

12-1-2021

A Human-Embodied Drone for Dexterous Aerial Manipulation

Dongbin Kim

Follow this and additional works at: <https://digitalscholarship.unlv.edu/thesesdissertations>



Part of the [Artificial Intelligence and Robotics Commons](#), and the [Robotics Commons](#)

Repository Citation

Kim, Dongbin, "A Human-Embodied Drone for Dexterous Aerial Manipulation" (2021). *UNLV Theses, Dissertations, Professional Papers, and Capstones*. 4298.

<http://dx.doi.org/10.34917/28340348>

This Dissertation is protected by copyright and/or related rights. It has been brought to you by Digital Scholarship@UNLV with permission from the rights-holder(s). You are free to use this Dissertation in any way that is permitted by the copyright and related rights legislation that applies to your use. For other uses you need to obtain permission from the rights-holder(s) directly, unless additional rights are indicated by a Creative Commons license in the record and/or on the work itself.

This Dissertation has been accepted for inclusion in UNLV Theses, Dissertations, Professional Papers, and Capstones by an authorized administrator of Digital Scholarship@UNLV. For more information, please contact digitalscholarship@unlv.edu.

A HUMAN-EMBODIED DRONE FOR DEXTEROUS AERIAL MANIPULATION

By

Dongbin Kim

Bachelor of Science - Aircraft Systems Engineering
Korea Aerospace University, Republic of Korea
2017

A dissertation submitted in partial fulfillment
of the requirements for the

Doctor of Philosophy - Mechanical Engineering

Department of Mechanical Engineering
Howard R. Hughes College of Engineering
The Graduate College

University of Nevada, Las Vegas
December 2021



Dissertation Approval

The Graduate College
The University of Nevada, Las Vegas

November 30, 2021

This dissertation prepared by

Dongbin Kim

entitled

A Human-Embodied Drone for Dexterous Aerial Manipulation

is approved in partial fulfillment of the requirements for the degree of

Doctor of Philosophy - Mechanical Engineering
Department of Mechanical Engineering

Paul Oh, Ph.D.
Examination Committee Chair

Kathryn Hausbeck Korgan, Ph.D.
*Vice Provost for Graduate Education &
Dean of the Graduate College*

Woosoon Yim, Ph.D.
Examination Committee Member

Mohamed Trabia, Ph.D.
Examination Committee Member

Georg Mauer, Ph.D.
Examination Committee Member

Jin Ouk Choi, Ph.D.
Graduate College Faculty Representative

ABSTRACT

Current drones perform a wide variety of tasks in surveillance, photography, agriculture, package delivery, etc. However, these tasks are performed passively without the use of human interaction. Aerial manipulation shifts this paradigm and implements drones with robotic arms that allow interaction with the environment rather than simply sensing it. For example, in construction, aerial manipulation in conjunction with human interaction could allow operators to perform several tasks, such as hosing decks, drill into surfaces, and sealing cracks via a drone. This integration with drones will henceforth be known as dexterous aerial manipulation.

Our recent work integrated the worker's experience into aerial manipulation using haptic technology. The net effect was such a system could enable the worker to leverage drones and complete tasks while utilizing haptics on the task site remotely. However, the tasks were completed within the operator's line-of-sight. Until now, immersive AR/VR frameworks has rarely been integrated in aerial manipulation. Yet, such a framework allows the drones to embody and transport the operator's senses, actions, and presence to a remote location in real-time. As a result, the operator can both physically interact with the environment and socially interact with actual workers on the worksite.

This dissertation presents a human-embodied drone interface for dexterous aerial

manipulation. Using VR/AR technology, the interface allows the operator to leverage their intelligence to collaboratively perform desired tasks anytime, anywhere with a drone that possesses great dexterity.

ACKNOWLEDGEMENTS

I would like to thank the people who supported my research from all aspects of my life. First, I would like to thank my dissertation committees for their time and advice. Next, I thank my colleagues from Drones and Autonomous Systems Lab (DASL) at the University of Nevada, Las Vegas (UNLV) for their warm support and assistance. Additionally, I would like to thank my father, Taehoon Tony Kim, my mother, Nayoung Kim, and my sister, Jinah Kim for their love, encouragement, and support in this long journey. Finally, I'm sincerely appreciative of my advisor, Dr. Paul Y. Oh, for his guidance, leadership, support, motivation, love, and encouragement during my time at UNLV.

Financial support for this study is provided by the U.S. Department of Transportation, Office of the Assistant Secretary for Research and Technology (USDOT/OST-R) under Grant No. 69A3551747126 through the INSPIRE University Transportation Center (<http://inspire-utc.mst.edu>) at Missouri University of Science and Technology. The views, opinions, findings and conclusions reflected in this publication are solely those of the author and do not represent the official policy or position of the USDOT/OST-R, or any State or other entity.

TABLE OF CONTENTS

ABSTRACT	iii
ACKNOWLEDGEMENTS	v
LIST OF TABLES	viii
LIST OF FIGURES	xi
CHAPTER 1 Introduction	1
CHAPTER 2 Literature Review	5
2.1 Mobile Manipulation	5
2.2 Aerial Manipulation	7
2.2.1 Aerial Grasping	7
2.2.2 Aerial Manipulator	8
2.2.3 Cooperative Aerial Manipulation	16
2.3 Test-and-Evaluation Platform	18
2.4 Haptic Manipulation	20
2.5 Telepresence Manipulation	23
CHAPTER 3 Preliminary Works	26
3.1 Aerial Manipulator Control	26
3.2 Lab Automation Drone	28
3.2.1 Parallel Manipulator	29
3.2.2 Parallel Manipulator Inverse Kinematics	31
3.2.3 Sensorized Parallel Jaw Gripper	35
3.2.4 Lab Automation Drone Prototype	37
3.2.5 Test-and-Evaluation	37
3.3 Testing-and-Evaluation Platform for Haptic-based Aerial Manipulation ..	40
3.3.1 Mobile Manipulating Unmanned Aerial Vehicle	41
3.3.2 Testing-and-Evaluation Platform	41
3.3.3 Haptic Device Force Rendering	43
3.3.4 Haptic Manipulation in Testing-and-Evaluation Platform	46
3.3.5 Flight Trials for Validation-and-Verification	47
3.4 Human-Drone Interface for Aerially Manipulated Drilling with Haptic Feedback	52
3.4.1 Customized Haptic Drill Press Design	53

3.4.2	Aerial Manipulator Concept Design	54
3.4.3	Force Rendering Limit for Target Material Selection	56
3.4.4	Sensitivity Gain	58
3.4.5	Proof-of-Concept Trials in Mini-SISTR	59
3.4.6	Proof-of-Concept Flight Trials	64
CHAPTER 4	General Objectives	69
4.1	Human-embodied Drone with Simple Task	71
4.1.1	Aerial Manipulator Design	71
4.1.2	Human body-motions	72
4.1.3	Haptics, Vision and Audio Feedback	76
4.1.4	Virtual World Configuration	80
4.1.5	Flight Test	83
4.2	Human-embodied Drone with Complex Tasks	90
4.2.1	Aerial Manipulator Design	91
4.2.2	Human body-motions	92
4.2.3	Haptics and Synthetic Vision	94
4.2.4	Mobility	98
4.2.5	Immersion	99
4.2.6	Flight Trials	100
CHAPTER 5	Conclusion	107
5.1	Summary of Contributions	107
5.2	Future Work	108
BIBLIOGRAPHY	110
CURRICULUM VITAE	119

LIST OF TABLES

3.1	Physical Properties of the manipulator concept design	31
3.2	Angular coordinates of leg attachment points to the base and moving platform.....	32
3.3	Leg attachment positions to the top and base in manipulator base coordinates	33
3.4	Physical Properties of the parallel gripper concept design	36
3.5	Rotation angle of revolute joint	39
3.6	The joystick position to MM-UAV arm position	46
3.7	Physical Properties of Aerial Manipulator	57
3.8	Gantry Haptic Drill Press Results Summary	61
3.9	Aerial Drill Press Test Flight Results Summary.....	67
4.1	Manipulator's Denavit-Hartenberg Parameters.....	73
4.2	Aerial Manipulator and the Operator Physical Properties	74
4.3	Aerial Manipulator Denavit-Hartenberg Parameters	93
4.4	Aerial Manipulator and the Operator Physical Properties	93

LIST OF FIGURES

2.1	Mobile Manipulation Implementations.....	6
2.2	Aerial grasping implementations	7
2.3	Aerial manipulator cascade PID controller scheme [18]	9
2.4	Aerial manipulator impedance controller scheme [27].....	11
2.5	Aerial manipulation implementations [37]	12
2.6	Aerial manipulation implementations	14
2.7	Aerial manipulation implementations.....	16
2.8	Cooperative aerial manipulation implementations.....	16
2.9	SISTR implementation: valve turning aerial manipulator [54]	19
2.10	Haptic manipulation implementations	20
2.11	Haptic-based aerial manipulation implementations.....	22
2.12	Telepresence manipulation implementations	23
2.13	Telepresence aerial manipulation implementations [65]	25
3.1	Aerial manipulator controller scheme	27
3.2	High Throughput Screening Laboratoy (Tecan journal, 3-2007)	29
3.3	Re-sized parallel manipulator concept design (inverted for clarity).....	30
3.4	LEGO-Based sensorized parallel jaw gripper concept.....	36
3.5	Lab automation drone prototype	37
3.6	Gantry-based test-and-evaluation platform	38
3.7	Micro-plate pick-and-place	39
3.8	Aerial manipulation with a haptics device. Operator feels reaction forces on the manipulator (inset); Inset shows manipulator grabbing a spring	40
3.9	MM-UAV design.....	42
3.10	The Touch (lower right corner) is adjusted to command the gantry and MM-UAV arm (background) to grab a spring (inset).....	43
3.11	The weight is applied (bottom), a substrate is constructed with strain gauge, a pin to grab a spring (inset).....	45
3.12	Haptic manipulation in testing-and-evaluation platform (origin 60 <i>mm</i>)	47
3.13	Haptic manipulation in testing-and-evaluation platform results.....	48
3.14	MM-UAV and spring test bench in the motion capture arena being controlled by the Touch haptic device	49
3.15	The cascade control system scheme.....	49
3.16	Flight trial closeup view	50
3.17	Flight trial results during force rendering	50

3.18	MM-UAV flight trials description.....	51
3.19	Aerial manipulation with a customized haptic drill press. Operator feels reaction forces on the manipulator (inset); Inset shows a rotary drill manipulator drill pressing on a plywood board.....	52
3.20	Customized haptic drill press design; drill chuck position (inset).....	53
3.21	Selected tool performance test: acrylic sheet, PVC pipe, plywood board, metal sheet, concrete, brick, and drywall (clockwise, inset).....	55
3.22	Aerial manipulator with 1-DoF drill manipulator design.....	56
3.23	Dynamixel calibration results: drill manipulator (top) & drill press (bottom).....	58
3.24	The haptic drill press (top-right), drill manipulator (background), and operator pressing the drill onto a test material (inset).....	59
3.25	Haptic drill press on plywood board (left), PVC pipe(Top inset), Acrylic sheet (Bottom inset).....	60
3.26	Unsuitable materials for haptic drill press.....	61
3.27	Haptic drill press in mini-SISTR results summary (raw force value sign changed for better understanding).....	62
3.28	Haptic drill press in gantry-based system results; Each figure displays force (top) & the manipulator's height (bottom).....	63
3.29	Flight environment and workspace;.....	64
3.30	Overall system scheme.....	65
3.31	Flight trial results.....	66
3.32	Aerial drill press test flight results summary (Raw force value sign changed for better understanding).....	67
3.33	Flight test closeup view from left to right; Plywood board, PVC pipe, Acrylic sheet.....	68
4.1	Human-embodied Drone Notional Concept.....	69
4.2	Human-embodied drone performing tasks in real world (left), operator in VR station (top right), View to the operator thorough VR headset (bottom right)......	71
4.3	Close view of aerial manipulator's dual-arm and camera.....	72
4.4	Kinematics relationship between the aerial manipulator and the operator with VR device (links expanded for clarity).....	73
4.5	Elbow up and down configuration: yellow lines describes the steel elbow frame.....	75
4.6	Sensorized end-effector for haptic feedback.....	76
4.7	2D vision feedback system: what the aerial manipulator see through the red triangle area is rendered to the operator. Red triangle area shows the camera's field-of-view (FOV).....	78
4.8	LiDAR cart overview: (a) LiDAR cart; (b) LiDAR tilts along with y-axis by a DC motor. Yellow area depicts LiDAR's scan range ($\pm 135^\circ$).....	78
4.9	Pre-made 3D model of the work space.....	79

4.10	Final 3D virtual world in Unity engine. The inset shows the graphical user interface and aerial mainpulator models	81
4.11	2D camera feedback configuration in the virtual world: field-of-views of the camera and the VR headset are shown in red and yellow, respectively	82
4.12	Flight trials: Unity scene (top), the motion capture area (bottom left), and VR station with the operator (bottom right)	84
4.13	Aerial Manipulator Controller Scheme	84
4.14	Flight trial results: Scenario 1	85
4.15	Flight trial results: Scenario 2	87
4.16	Noise filtering results	88
4.17	Flight trial summary: Scenario 1	89
4.18	Flight trial summary: Scenario 2	90
4.19	Close-up of Aerial Manipulator: a single arm and gripper is attached under drone's belly; a camera is attached close to the landing gear	91
4.20	Kinematics relationship between the aerial manipulator and the operator with the VR device(links expanded for clarity)	92
4.21	Synthetic vision by fisheye camera, and the operator with VR Headset. Yellow area shows the camera's field-of-view (FOV)	95
4.22	Fisheye camera image stitching into 3D sphere	96
4.23	Human-embodied drone controller scheme	97
4.24	Overall virtual world scene in Unity engine	99
4.25	Flight Environment: Unity view (top), the motion capture arena (bottom left), and VR station with the operator (bottom right)	100
4.26	Trajectories of the reference and measured position, from <i>All Tasks</i> : X (Top) to Z (Bottom)	103
4.27	Flight trial summary of <i>Task 1</i>	104
4.28	Flight trial summary of <i>Task 2</i>	105
4.29	Flight trial summary of <i>Task 3</i>	106

CHAPTER 1 INTRODUCTION

Mobile manipulation employs one or several robot manipulators that are designed for tasks such as object positioning, sensor insertion, and tool handling. These manipulators can be attached to ground vehicles, aircraft, underwater robots, and space robots to enable the following operations: structure assembly, valve-turning, underwater salvaging, and satellite repair respectively. Mobile manipulation using aerial, underwater, and space vehicles is particularly challenging because such vehicles are free-floating; they must counteract the reaction forces and torques generated by the manipulator-object interaction.

Aerial manipulation is an active research topic in robotics. Drones with serial, parallel, and bio-inspired manipulators have been deployed for various operations such as valve-turning, structure assembly, package manipulation, and industrial applications. The rationale is that Mobile-Manipulating Unmanned Aerial Vehicles (MM-UAVs) could replace workers in high-risk situations such as bridge, wind turbine, or power line inspections. In the past decade, researchers have focused on designing autonomous aerial manipulation systems. The notion is that an MM-UAV could autonomously execute object identification, grasp configuration, and motion planning to accomplish desired goals. Research groups have accomplished this by simplifying object geometries that can be easily identified with computer vision, utilizing object rigidity for pinch or power grasps and basic translation-rotation path

plans. Relaxing such properties has given value to aerial manipulation but prevents full implementation and, hence, adoption.

Recently, haptic sensing has been adopted to present a more collaborative approach to aerial manipulation. The main key is to include the worker and leverage their expertise to collaboratively perform aerial manipulation. In bridge maintenance, for example, the worker often touches rivets, pokes surfaces, and pries patches. Such haptic assessments provide important information in the routine inspection of bridges. Haptic sensing literature, especially in medical robotics, has a long history. The growth of minimally invasive surgery and tele-medicine has yielded commercial haptic devices. Furthermore, haptic-based interfaces are employed in mobile phones, Virtual Reality (VR), and other various wearable devices. Such interfaces are used for touch screens, interactive controllers, and clinical rehabilitation respectively. The use of such haptic devices enables the worker to perform various tasks to leverage the haptic feedback assessment of object properties to collaboratively perform aerial manipulation using drones. This could yield collaborative drones that augment a worker's ability to perform assessments and maintenance remotely. Towards this vision, haptic-based MM-UAVs have been built for tasks such as peg-in-hole, drilling, and pipe inspection.

Drones are fragile, easy to crash, and challenging to repair. Due to additional risks that come with mounting manipulators and interactions with the environment, testing-and-evaluation (*T&E*) platforms are required prior to the flight trials. *T&E* platforms have been built in simulation and hardware. Simulation-based platforms

such as Gazebo save time in hardware fabrication, crashes, and repairs. However, in complex scenarios where the drone has a hyper-redundant manipulator for tasks in a convoluted environment, this could be time-consuming. Also, the performance of these platforms cannot be trusted until it is validated and verified by relevant scenarios. Hardware-based platforms like a gantry system are designed to use their end-effector to emulate the drone's motions and realize the environment from the scenario. This can provide a safe and repeatable indoor flight trial environment while avoiding challenges and restrictions from the simulation platform. Thus, one can analytically perform test-and-evaluation for aerially manipulated operations before validation-and-verification flights outdoors or indoors (without the gantry).

Previous works have added value to the state-of-art aerial manipulation. However, most of the tasks were accomplished when the drone was within the operator's line-of-sight. Thus, one of the challenges remaining is to give the operator a sense of presence beyond their line-of-sight; the operator does not feel the senses and actions transported to and from the drone. What lacks in the previous work is the sensory information about the physical layout and social interaction with on-site workers.

To address this challenge, this dissertation adopts an immersive framework into the haptic-based human-in-the-loop aerial manipulation platform. The net effect of immersive technologies like VR and Augmented Reality (AR) is the *embodiment* of the user. Such a human-embodied interface enables operators to leverage their skills and experience to dexterously handle such objects; the operator can identify suitable grasp points and center-of-mass (CoM) to quickly perform material-handling tasks

like lifting-and-carrying, stacking-and-unstacking, and pushing-or-pulling of objects.

Toward this vision, this dissertation applies these notions in the context of aerial manipulation for tasks in bridge inspection and maintenance. The human-embodied drone has the goal of giving the worker a sense of presence while performing tasks on the bridge deck. This differs from teleoperated aerial manipulation; the worker actually sees, hears, and feels what is happening on the work site. The human-embodied drone can physically interact with objects and socially interact with workers who are on the work site.

CHAPTER 2 LITERATURE REVIEW

This chapter presents an overview of the past works in mobile manipulation (section 2.1), aerial manipulation (Section 2.2), test-and-evaluation platform (Section 2.3), haptic manipulation (Section 2.4), and telepresence manipulation (Section 2.5).

2.1 Mobile Manipulation

Manipulators on mobile vehicles have been demonstrated for applications in ground, underwater, air, and space (see Figure 2.1). Work in [1] demonstrates dexterous robot arms attached to Robonaut for manipulation tasks in space. Mobile camera-space manipulation (MCSM) in [2] was developed for planetary exploration rover missions, such as the prototype for NASA's 2003 Mars Exploration Rover. Work in [3] illustrates the control architecture and design of an anthropomorphic underwater robot, Ocean One (O_2). This underwater robot was built for deployment to an archaeological mission to the "Lune," a French naval vessel that sank in 1664 in the Mediterranean sea.

Humanoids like Honda Asimo, DRC-Hubo, and Boston Dynamics Atlas are designed to use highly dexterous arms to perform ground operations for task assistance, disaster response, and search-and-rescue, respectively [4]-[8]. The customized ground robot, RUR53, in [9][10] presents the control and planning strategies for au-

onomous navigation and manipulation missions at the Mohamed Bin Zayed International Robotics Challenge (MBZIRC). The challenge includes wrench detection, recognition, grasping, and valve-turning. The robots above are important to study for aerial manipulation because the goal is mainly to counter-balance the reaction force during the manipulation task.



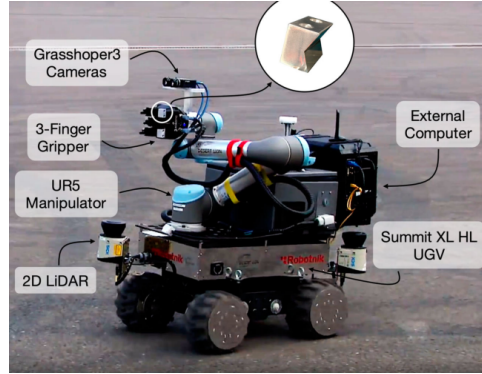
(a) NASA Rover Prototype [1]



(b) DRC-Hubo [7]



(c) Ocean One [3]



(d) RUR53 [9]

Figure 2.1: Mobile Manipulation Implementations

2.2 Aerial Manipulation

Aerial manipulation has been a paradigm shift to unmanned aerial vehicle (UAV) applications. The notion is that manipulators on an unmanned aerial vehicle could dexterously perform manipulation tasks in dangerous or inaccessible locations for workers. Several aerial manipulator designs have been presented: only grippers, or one or more robot limbs attached to an aerial vehicle, and cooperative aerial manipulators. They have accomplished tasks like grasping, pick-and-place, part-assembly, and object positioning.

2.2.1 Aerial Grasping

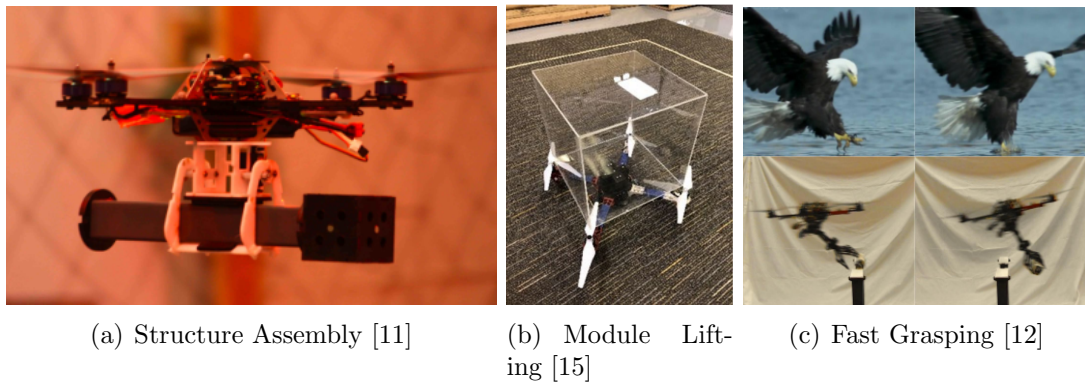


Figure 2.2: Aerial grasping implementations

Aerial grasping is intended to have a gripper directly attached to the aerial vehicles (see Figure 2.2). Quadrotor teams in [11] assembled 2.5-D structures from simple structural nodes and members equipped with magnets, called Special Cubic

Structures (SCS). Each quadrotor has a gripper attached to the belly side. Thus, they could pick up, transport, then assemble the structural elements. The proof-of-concept flight trials showcased the construction of a pyramid, wall, tower, and castle. The quadrotor’s design, modeling, estimation, and control architectures are summarized in [14].

Micro-UAVs (M-UAVs) in [12] performed high-speed grasping and payload transportation. The design was inspired by eagles hunting with their legs and claws. During the flight test, the M-UAV performed dynamic grasping using minimum snap trajectories in two different velocities. The modular construction group in [15] has addressed advantages and challenges for new UAV applications in module lifting and transporting. The authors designed a low-level gripper on top of a quadcopter to lift and transport a box-shaped construction module prototype. Though the approach is small-scaled, this paper expects to save the module lift and transport time and the costs of the overall construction process.

2.2.2 Aerial Manipulator

Though valuable in certain tasks, aerial grasping cannot perform more than a pick-and-place. An aerial vehicle with one or more robot limbs can create more opportunities to perform increasingly complex manipulations in air. This free-floating vehicle, called an aerial manipulator, has the following challenges: a controller that helps the vehicle balance its pose while interacting with the nearby environment and designing a manipulator and gripper for applications within the vehicle’s limited work

space.

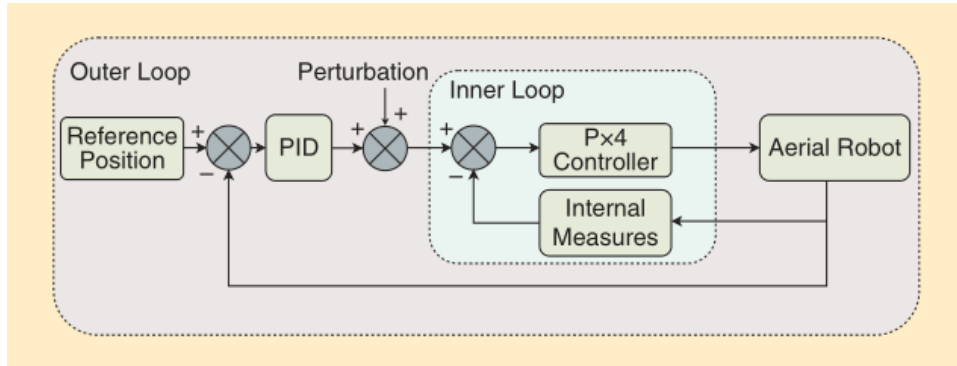


Figure 2.3: Aerial manipulator cascade PID controller scheme [18]

Controllers for aerial manipulators have been developed in the last few years. A cascade Proportional-Integral-Derivative (PID) controller is employed to compensate for the control error of aerial manipulator dynamics and quickly respond to the disturbances caused by internal errors such as sensor drifts. The authors in [16] utilized a motion capture system to capture the Mobile-Manipulating Unmanned Aerial Vehicle (MM-UAV)'s behavior for PID controllers. In addition, the authors in [18] placed a cascade PID controller outside of a commercial PX4 controller loop to compensate for the control error and perturbation from internal estimator errors in the PX4 controller. This approach successfully completed the aerial docking tasks (see Figure 2.3).

A visual servoing approach is demonstrated with an MM-UAV in [17]. The manipulator was visually servoed using an eye-in-hand camera with a specified pose

relative to a target while treating the motions of the host platform as perturbations. Simultaneously, the UAV pose was controlled using kinematic information from the manipulator. Hence, the manipulator could assume a joint-space configuration that maximize reachability, and the MM-UAV could compensate for unexpected motion during manipulation.

While the research above considers a UAV and robotic manipulators separately, others treat them as a coupled system. The non-linearity of the system has been stabilized by several controllers. An aerial manipulator developed at the University of SEville (AMUSE) in [21] presented a stable backstepping-based controller. This controller used the fully-coupled dynamic model for the multicopter and an admittance controller for the manipulator. This controller was then validated through a flight test with a rotorcraft containing eight rotors and a 7-DOF arm with a gripper to carry the sensors and processing hardware needed for outdoor positioning. Later, this performance was improved with the Closed-Loop Inverse Kinematics (CLIK) of aerial manipulators in [19]. CLIK provide smoother behavior to reduce perturbations and instability.

An adaptive sliding mode controller was developed in [24]. The authors developed the kinematic and dynamic models of a quadrotor using two-DOF robotic arms. This system successfully performed a pick-and-place task. Non-linear Model-Predictive Controller (NMPC) in [20] was integrated for aerial pick-and-place tasks. The controller was based on a sequential newton method for unconstrained optimal control and a high-frequency low-level controller that tracked the generated optimal reference

trajectories. The experimental results verify its effectiveness during the pick-and-place operation. A hybrid adaptive controller was embedded in an MM-UAV with multi-arms (4-DOF per arm) [26]. The controller used a combination of gain scheduling and a Lyapunov based Model Reference Adaptive Control (MRAC). Simulated flight experiments proved that the MRAC was capable of stabilizing the oscillations generated by unstable PID controllers from the author’s previous work [16].

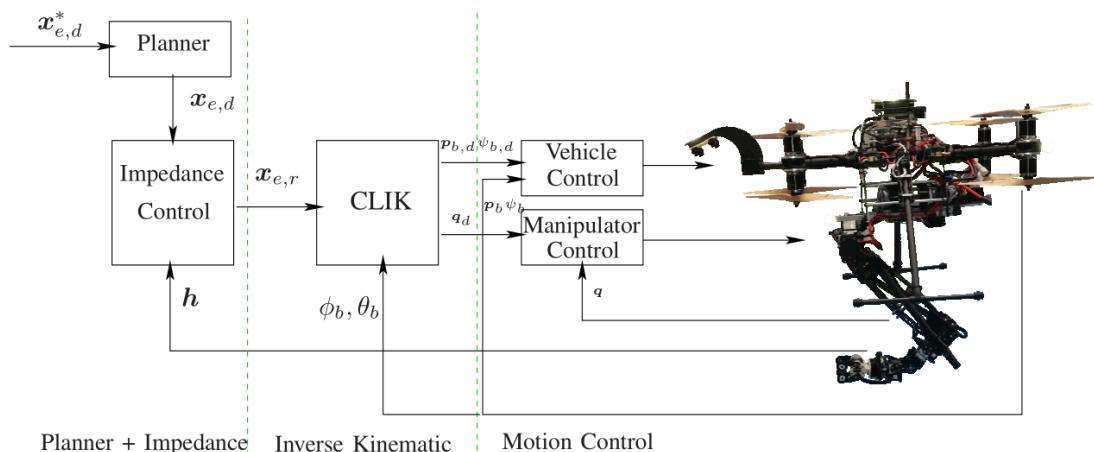


Figure 2.4: Aerial manipulator impedance controller scheme [27]

In addition, an impedance controller considers forces generated from physical interactions between aerial manipulators and the environment. [25] developed a cartesian impedance controller using the dynamic relationship between generalized external forces acting on both structure and system motion in terms of cartesian space coordinates. The results from the simulation validate the aerial vehicle’s ability to maintain stability during physical interactions. [27] proposed an impedance control scheme

for aerial manipulators (see Figure 2.4). The proposed controller has a multi-level architecture: the outer loop is composed of a trajectory generator and an impedance filter that modifies the trajectory to achieve a compliant behavior in the end-effector space; a middle loop is used to generate the joint space variables through a closed-loop inverse kinematic algorithm; lastly, the inner loop is aimed at ensuring the motion tracking. The proposed control architecture has been experimentally tested.

[28] showed a physical-virtual impedance controller for a lightweight, dual-arm aerial manipulator. This controller used force, torque, and virtual variables based on the deflection signals generated by a stereo vision system and a compliant spring-lever transmission mechanism. The vision system improved the pose accuracy and enabled appropriate estimations and a control of the contact forces.

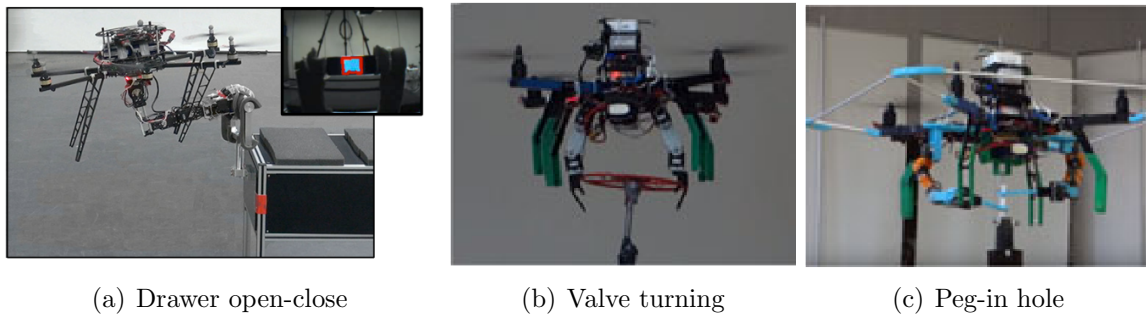


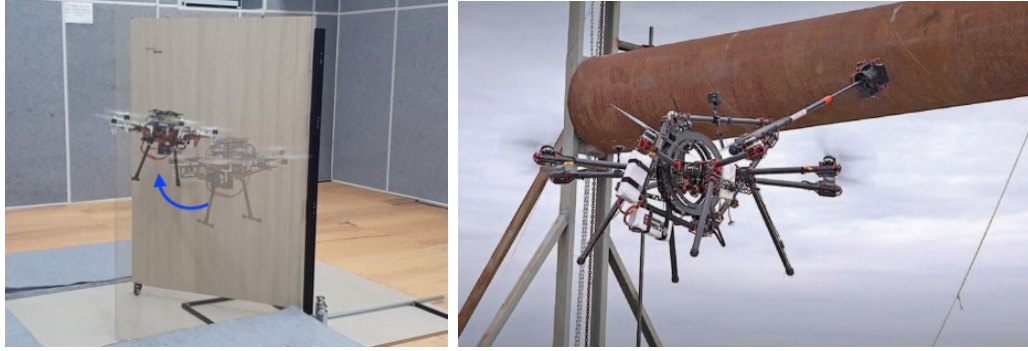
Figure 2.5: Aerial manipulation implementations [37]

With the promising controller performances described above, aerial manipulators have been deployed for practical applications. One of ARCAS European projects in [13] presented autonomous planning architectures for a team of aerial manipulators

to perform structure assembly. Three automatic planners were applied in sequence to compute assembly operations. The simulation results validated the feasibility of the approach. This work was then extended to the mechanical design of a light-weight 6-DOF aerial manipulator [33] and an aerial manipulator with multi-link arms [39].

Moreover, [29] employed an aerial manipulator for perching and door-opening missions. The authors introduced the door-approach control, attitude-change method, and mechanical designs for perching. Also, they developed a light-weight manipulator to twist the doorknob. The experimental results validated the performance of the proposed aerial manipulator. In the AEROWORKS project [30], a compliant aerial manipulator with 2-DOF arms was deployed for highly dynamic physical interaction tasks. They proposed one active rotational DOF and one passive linear DOF for the arm design to pitch movement compensation and impact energy absorption. [32] presented an aerial manipulator prototype with a robotic manipulator for physical interaction with the surrounding environment while remaining airborne. This prototype had a 3-DOF delta structured manipulator with a 3-DOF end-effector. Experimental results showed the successful physical interaction with the near environment by the prototype aerial manipulator.

[34] used an aerial manipulator for opening and closing an unknown drawer. To perform open-and-close drawer, the authors configured the aerial manipulator to exert a desired force on the drawer. They then controlled the velocity of the end-effector to deal with the uncertainties coupled with the mechanism of the drawer. The experiments demonstrated satisfactory results on performing the given tasks. In addition



(a) Hinged door open-close [38]

(b) Industrial Inspection [43]

Figure 2.6: Aerial manipulation implementations

to this work, another aerial manipulator from [38] opened a hinged door. Model Predictive Controllers (MPC) generated position setpoints to the Disturbance Observer (DOB)-based robust controller in real-time with a constrained version of Differential Dynamic Programming (DDP). The flight test showed the successful hinged door opening task.

An aerial manipulator in [36] performed valve turning tasks using a dual-arm. Prior to the flight test, yaw angle dynamics were analyzed and implemented into the controller. A human operator provided input to actuate the manipulators. The turning task was performed after the aerial manipulator was coupled to the valve. This dual-arm aerial manipulator was later deployed to perform peg-in-hole and pick-and-place tasks [37].

The AEROARMS project in [31] contributed to the development of a compliant 3-DOF arm with compliant fingers for an aerial manipulator. The arm employed shoulder pitch and elbow pitch joints for inspections, including contact forces with

the environment. This contribution was finally applied to a new aerial manipulator with dual arms and multi-directional thrusters for industrial inspection and maintenance [43]. The results successfully demonstrated the following operations: contact inspection of industrial pipes in air and ultrasonic measurements to determine pipe wall thickness.

The AERIALCORE project in [35] presented a lightweight active robotic arm with positioning compliant joints (POSITRON) for power-line inspection. POSITRON consists of a customized power-line attachment tool and a rotorcraft. Furthermore, in [40], their project proposed the application of a compliant bimanual aerial manipulator in two pipe inspection tasks involving the grasping and installation of inspection tools or sensor devices. Two configurations were considered for the manipulator design: a standard configuration with arms attached at the multicopter base and a long reach configuration with arms affixed to a passive pendulum. This work analyzed and compared the benefits and drawbacks of both configurations from the experimental results.

MM-UAVs with a parallel manipulator in [41] addressed the following shortcomings of serial manipulators for aerial manipulation: high disturbances in stability and difficulty in precision control. Thus, a 6-DOF parallel manipulator was attached to the underside of a UAV to perform manipulation. The experimental results showed the analytical benefits of the parallel manipulator in precise positioning and its lower impact on the UAV's center-of-gravity compared to a serial manipulator. This parallel mechanism was further used by lab automation drones for microplate delivery in

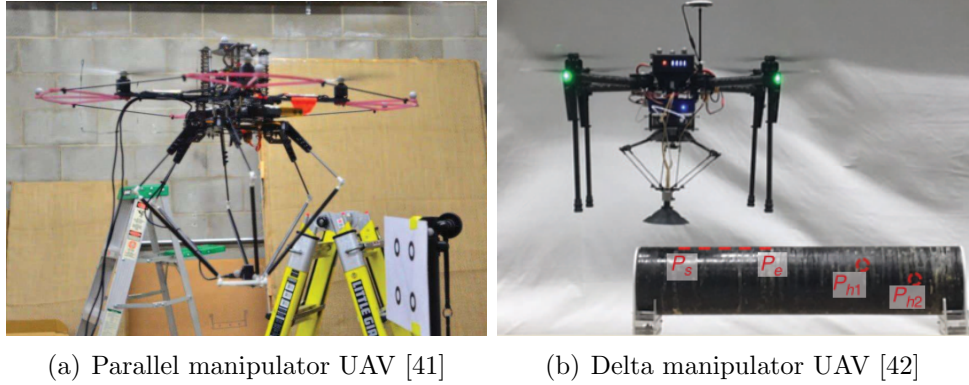


Figure 2.7: Aerial manipulation implementations

high throughput systems [71]-[73].

A reduced DOF parallel manipulator in [42] was employed for aerial repairs. In this research, a 3-DOF delta manipulator was employed on the aerial manipulator for precise aerial repairs using two-component LD40 Polyurethane (PU) foam. The flight test verified the precise pipe spot repairs using the given aerial manipulator.

2.2.3 Cooperative Aerial Manipulation

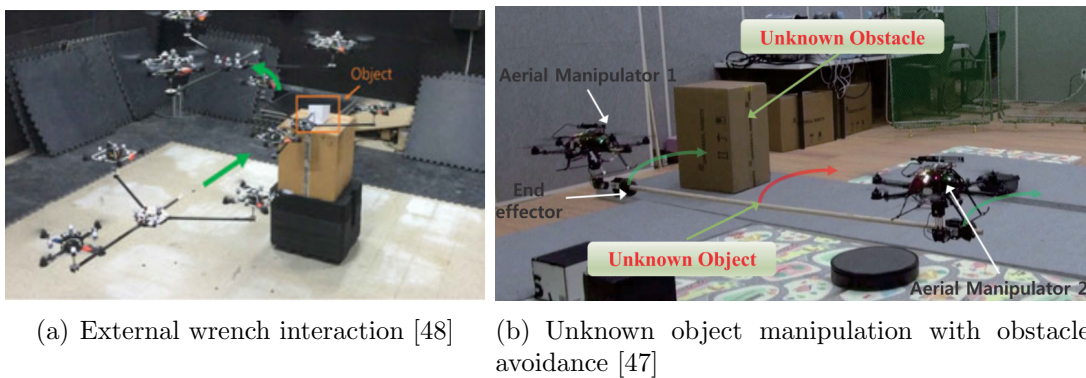


Figure 2.8: Cooperative aerial manipulation implementations

Aerial manipulation using a single aerial vehicle had the following active issues: limited workspace and payload of the vehicle; under-actuation, causing body-tilting with sideway force during manipulation; and complicated aerial manipulator assembly. This calls into question aerial manipulation of large, heavy, and long objects for industrial applications such as transporting construction material, industrial decommissioning, and urban search and rescue (USAR). Thus, cooperative aerial manipulation has been developed and explored (see Figure 2.8).

[44] and [48] proposed an aerial tool operation system using multiple quadcopters, where each quadcopter was used as a rotating thrust generator. They were connected to a tool by spherical joints, forming a Spherically Connected 2-Quadrotor Tool (S2QT) system. The Lyapunov approach was applied to control the system while performing tool operation tasks. Simulation and implementation results support the efficacy of this approach. In addition, a Spherically connected MultiQuadrotor (SMQ) system was built using three quadrotors. The system was deployed to interact with the external wrench and tele-manipulate an object.

The ARCAS-project in [45] presented a coordinated aerial manipulator control system for a bar transportation task. Two aerial vehicles with a 6-DOF manipulator were constructed. A coordinated controller for these vehicles had the following three layers: the centralized top layer, which planned the end-effector desired trajectories of each vehicle; the middle layer, local to each vehicle, which computed the corresponding motion references; and the bottom layer, which was a low-level dynamic motion controller that tracked the motion references. At the middle layer, the overall

mission was hierarchically decomposed in a set of elementary behaviors, which were combined together via the null space-based behavioral approach into more complex compound behaviors. Finally, the flight test was conducted to prove the performance of the presented approach.

[46] employed two generic aerial manipulators to perform cooperative manipulation of a cable-suspended load. The tasks were completed without the need of explicit communication between the agents. The proposed master-slave architecture exploited an admittance controller in order to coordinate the robots with implicit communication only, using cable forces. [47] presented a framework for cooperative aerial manipulation of unknown payload. The framework consisted of a controller, estimation of target payload, safety management, and obstacle avoidance with two aerial manipulators with a 2-DOF arm. An online estimator of the mass and inertial properties of an unknown payload was developed without force-torque sensors. This estimation was then fed to an adaptive controller to perform obstacle avoidance and unknown payload transportation.

2.3 Test-and-Evaluation Platform

For the past few years, research has been conducted on hardware-in-the-loop test rigs for testing-and-evaluation (T&E) of drones, sensor suites, controller design, path planning, and aerial manipulation. The notion is that this test rig can provide a safe and repeatable indoor or outdoor flight test environment for aerial manipulation (see Figure 2.9).

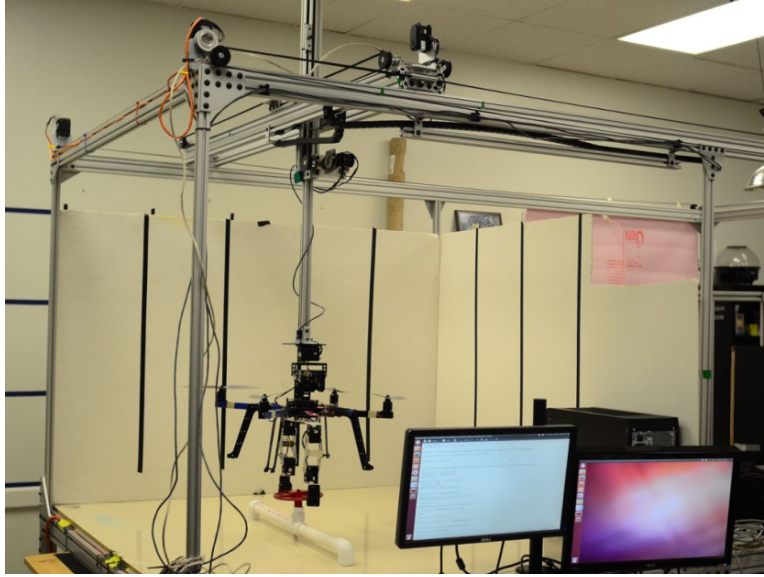


Figure 2.9: SISTR implementation: valve turning aerial manipulator [54]

A gantry-based T&E platform called SISTR (Systems Integrated Sensor Test Rig) was initially proposed in [49]. This $25 \times 25 \times 25$ cubic foot platform included model reference adaptive control to emulate aircraft motions. SISTR included fans, lamps, and fog machines for the T&E in the presence of gusts, glare, and obscurants. Therefore, one could perform indoor flight tests safely and analytically before validation-and-verification flights (V&V).

The authors in [50] and [53] attached a 7-DOF manipulator to SISTR. An impedance controller was integrated in a manipulator to control the dynamic interaction between the manipulator and the nearby environment. Finally, SISTR performed hose-insertion tasks. The experiment results validated the performance of the designed kinematic, dynamic model and controller. With the promising results, an aerial manipulator for hose-insertion was constructed in [54], then verified and validated by

flight test in [37]. The same strategy was applied to aerial manipulators to complete tasks like visual servoing, (T&E [51], V&V [41]) valve-turning (T&E [52], V&V [36]), and microplate pick-and-place (T&E [72], V&V [73]).

2.4 Haptic Manipulation

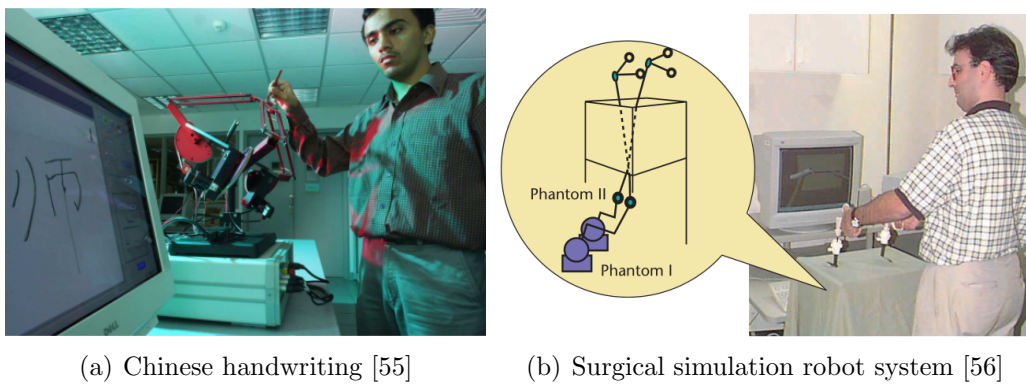


Figure 2.10: Haptic manipulation implementations

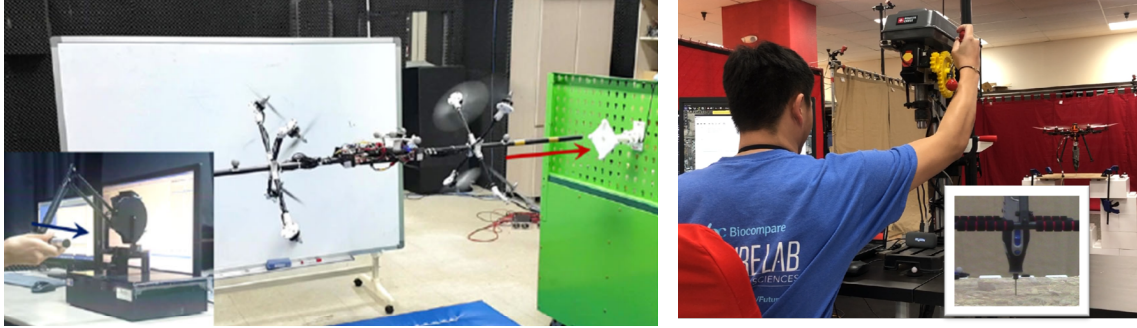
Haptics in literature has a long history. The purpose of haptics is to provide information to the user based on physical interactions via touch. Haptics has been integrated for manipulation in the fields of education, medical, and food as well as immersive technologies like Virtual (VR) or Augmented Reality (AR) (see Figure 2.10).

[55] presented a 6-DOF haptic interface as a robotic teacher for Chinese handwriting. The interface reflected the image ensuring transparent virtual manipulation with undistorted hand-eye coordination. The authors stated the benefits of such a device for people with visual impairments or even people who are unfamiliar with

Chinese writing. [56] presented a haptic interface for Minimally Invasive Surgical Simulation and Training (MISST). The interface included touching, feeling, and organ manipulation through instruments for medical personnel training. The growth of haptic manipulation in the medical field yielded commercial haptic devices like 3DS Haptics [90]. [57] collected haptic and motion signals to learn human feeding behaviors for robotic feeding. Haptic datasets were collected using a force torque sensor embedded fork. In addition, motion was recorded by a motion capture system. The experiment results showed that a robot arm using a large dataset could successfully feed a mannequin.

Finger Glove for Augmented Reality (FinGAR), a wearable tactile device in [58], was developed for fingertip interaction with the virtual world. FinGAR was designed to be lightweight, simple, and easy to wear and also move to satisfy standards for a general virtual reality system. FinGAR devices were attached to the thumb, index, and middle fingers of the user. This device combines electrical and mechanical stimulation to provide tactile feedback of virtual objects: skin deformation, high/low frequency vibration, and pressure.

In aerial manipulation, haptic sensing can provide meaningful system information to the operator. This can improve task dexterity and hence overcome the following current issues in autonomous aerial manipulation: the inability to unexpected changes in the environment, and complex object geometries. [59] presented a bilateral tele-operation scheme for cooperative aerial manipulation using a commercial haptic device. The haptic device controlled multi-UAVs to perform object pick-and-



(a) Wrench generation with ODAR [60]

(b) Aerially manipulated drill tasks [74]

Figure 2.11: Haptic-based aerial manipulation implementations

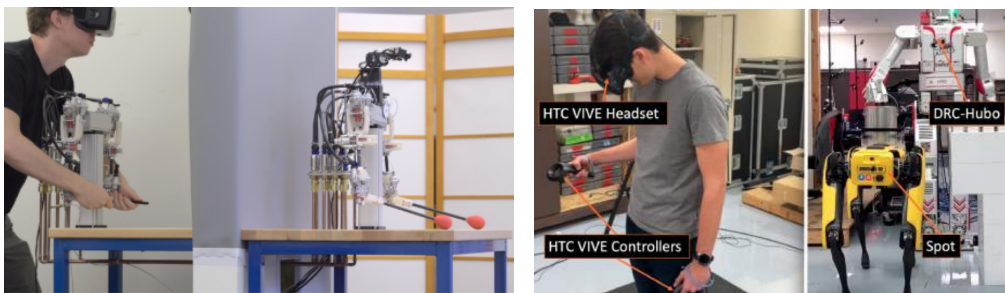
place tasks. Haptic feedback was important in reducing task completion time and enhancing the tracking performance of the flight trajectory. OmniDirectional Aerial Robot (ODAR) in [60] performed wrench generation and peg-in-hole tasks using a haptic device. The haptic device generated desired trajectories of ODAR and rendered contact force feedback to the user during the tasks (see Figure 2.11(a)).

[74] proposed a testing-and-evaluation platform for haptic-based aerial manipulation. The platform consisted of a gantry system, a commercial haptic device for emulating drone motions, and force rendering to the operator, respectively. The notion was that this platform could provide a safe and repeatable flight test environment for haptic-based aerial manipulation. [75] showcased aerially manipulated drill tasks using haptic feedback. An aerial manipulator with a 1-DOF drill arm and a customized haptic drill press were constructed. During the tasks, force is sensed when the drill bit contacted the surfaces of the materials. This force was then rendered to the operator. The tasks were successfully completed with test materials (see Figure 2.11(b)).

2.5 Telepresence Manipulation

Telepresence provides users the ability to directly interact with a physically real, remote environment experienced from a first-person Point-Of-View (POV). Regardless of the location, one is still able to perceive and act as if being present in a different location. This can be beneficial for manipulation when the task has to be done beyond a worker's line-of-sight. In past years, the growth of immersive technologies (e.g., VR/AR) has created new interfaces for telepresence manipulation.

[61] presented a tele-operated robot with a VR system for telepresence manipulation. The user at the remote station controlled force-reflection joysticks to command an electro-hydraulic servo drive-based manipulator and perform pick-and-place at the work site. The task was captured in real-time by a video camera in the remote computer. In addition, a graphic computer showed real-time motions of the manipulator and target object in VR. Thus, this combination solved time delay issues in tele-operation systems.



(a) Human robot interaction [62]

(b) Heterogeneous robot control for construction tasks [63]

Figure 2.12: Telepresence manipulation implementations

[62] presented a haptic telepresence humanoid robot for human-robot interaction (see Figure 2.12(a)). The robot had a hybrid hydrostatic transmission mechanism for two 4-DOF arms and a pair of stereo cameras mounted on the neck side. These cameras provided live video feedback to the VR headset worn by the operator. A master-slave approach was implemented for the manipulation. The operator gave neck/arm motions to the slave robot using the master robot. The slave robot interacted with the recipient for the tasks.

[64] employed a mobile humanoid nursing robot to perform food serving tasks with telepresence cameras. The camera was selected autonomously for visual feedback to the operator. The human motor system was then coupled with the cameras to create the natural perception-action. Hence, this allowed for active perception control using visual feedback from the wearable and standalone cameras for manipulation in food serving scenarios. [63] deployed heterogeneous robots for tasks in construction environment (see Figure 2.12(b)). Multimodal teleoperation was performed using a VR-based framework. The framework enabled the operator to control a humanoid synchronously and a quadruped robot asynchronously with VR controllers. Multiple cameras were integrated to provide live 3D images from different angles to the operator with a VR headset. The experimental results successfully demonstrated the feasibility of the framework in a construction environment.

In aerial manipulation, [65] presented a state-of-the-art telepresence system for enhancing aerial manipulation capabilities (see Figure 2.13). The system consisted of a haptic device, VR, and a cable-Suspended Aerial Manipulator (SAM). The VR

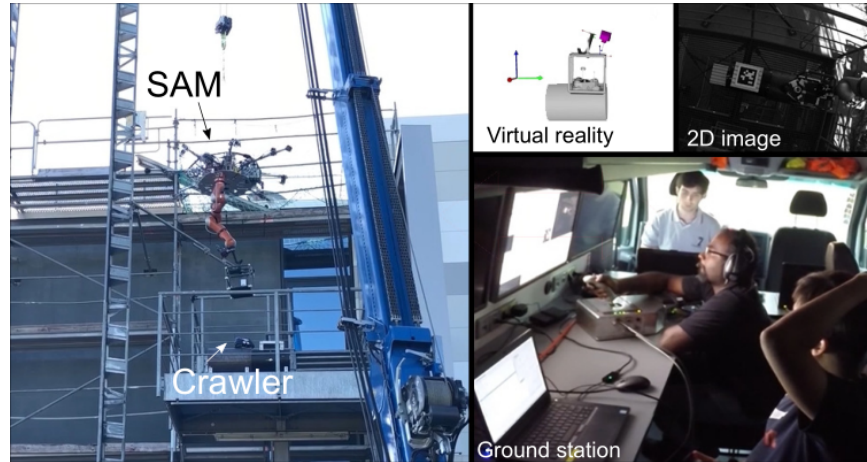


Figure 2.13: Telepresence aerial manipulation implementations [65]

device provided real-time 3D visual feedback to the operator at a remote station. This vision feedback was achieved by utilizing onboard visual and inertial sensors, an object tracking algorithm, and a pre-generated object database. The experiment results showed the benefits of the proposed system in accomplishing advanced aerial manipulation tasks like grasping, placing, force exertion, and peg-in-hole insertion.

CHAPTER 3 PRELIMINARY WORKS

This chapter addresses preliminary works toward this dissertation. They are organized by the following sections: aerial manipulator control (Section 3.1); lab automation drone (Section 3.2); testing-and-evaluation platform for haptic-based aerial manipulation (Section 3.3); and aerially manipulated drilling using haptic feedback (Section 3.4).

3.1 Aerial Manipulator Control

The fundamental theories underlying UAV dynamics are generally understood [66]-[68]. The rapid growth of open-source projects on UAV systems has yielded commercial autopilot controllers like Pixhawk, Ardupilot, and MultiWii [93]-[95]. They provide stable performance for a single UAV operation which includes indoor/outdoor aerial imaging, UAV racing, and semi-autonomous waypoint flight for outdoor skywriting [70].

However, when a UAV is coupled with moving payloads like a robotic manipulator, control design for such aerial manipulators becomes challenging due to the following: the vehicle is free-floating, a robotic manipulator on the vehicle creates coupling effects in the system dynamics, and the manipulator's dynamics depend on the different configurations for the desired tasks. Thus, several designs have been ad-

dressed to control the aerial manipulator while the vehicle is counter-balancing forces from physical interaction with objects.

[69] separates the aerial manipulator controllers into two approaches. The first approach includes a centralized approach. This considers the UAV and the robotic manipulator as unique entities. Thus, complete kinematic and dynamic models are required prior to designing the controller and the trajectory planning. The second approach involves using decentralization. This considers the UAV and the robotic manipulator as two separate independent systems. Coupling effects from the manipulator on the vehicle are considered external disturbances. The net effect of this approach is a utility for several cases: dynamics of the manipulator, complexity of dexterous tasks, and the constant shift of center-of-mass (CoM) during flight.

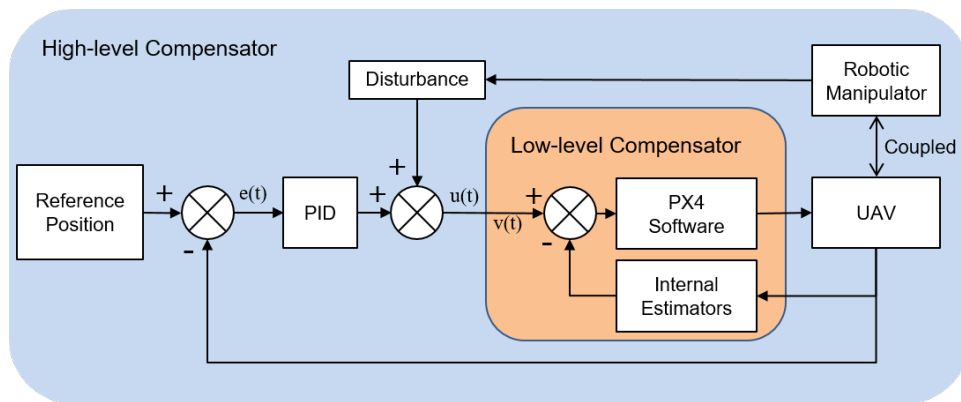


Figure 3.1: Aerial manipulator controller scheme

Considering the above, the decentralized approach was selected to control the aerial manipulator in this dissertation. The control architecture was motivated by a

cascade control system in [18]. The controller was constructed with low/high-level compensators (see Figure 3.1).

A low-level compensator was provided by PX4 software in *Pixhawk*. In the PX4 software, the internal estimator estimates attitudes of the vehicle's dynamics via Extended Kalman Filter (EKF)'s using an Inertia Measurement Unit (IMU), magnetometer, and a barometric pressure sensor. Then, the control inputs are computed by a cascade PID controller, taking the difference between the estimated and the reference velocity of the vehicle. The inputs are translated to the corresponding actuation on the motors.

A high-level compensator has a cascade PID controller in the parent loop of the low-level compensator. This provides quick responses to the external disturbances caused by the manipulator and internal estimator errors such as sensor drift. The UAV and reference positions are compared to form the error $e(t)$. After compensation, the signal $u(t)$ is formed and converted into a reference velocity $v(t)$ in the low-level compensator as an input for the internal controller.

3.2 Lab Automation Drone

With promising progress in aerial manipulation, the National Institute of Health (NIH) had looked for potential uses of UAV in high throughput systems (HTS) [97]. The goal was to add more flexibility to existing HTS by using the empty space above the test station (Figure 3.2). The critical gap is that there is no manipulator and gripper design for the lab automation drone. In [71]-[73], a concept lab automation drone

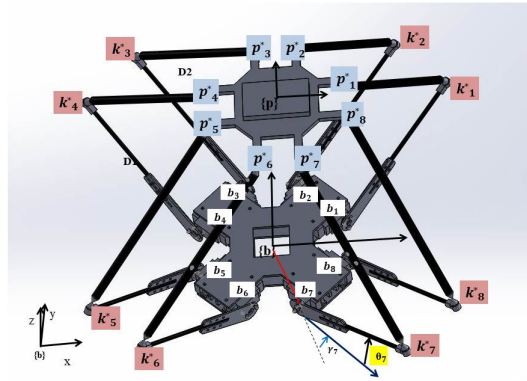


Figure 3.2: High Throughput Screening Laboratory (Tecan journal, 3-2007)

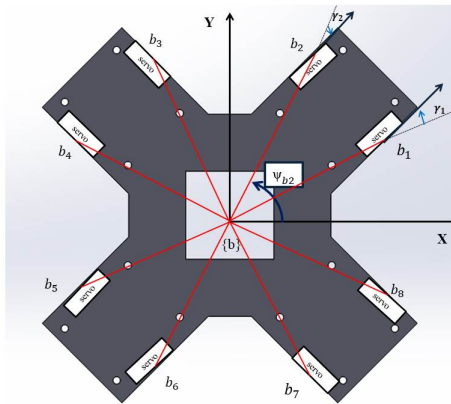
was demonstrated to deliver a micro-plate from a test station to another in a high throughput system (HTS). The concept drone was built with a parallel manipulator (Section 3.2.1-3.1.2), a sensorized parallel jaw gripper (Section 3.2.3), and a drone (Section 3.2.4). Micro-plate pick-and-place tasks were performed in a gantry-based test-and-evaluation platform (Section 3.2.5).

3.2.1 Parallel Manipulator

From [41], in comparison to a serial manipulator, a parallel manipulator provides higher precision and lowers the impact on a drone's center-of-gravity. Thus, the 6 degree-of-freedom (6-DOF) parallel manipulator is built with 8 servo motors,



(a) CAD Design of the manipulator



(b) Geometrical arrangement of leg attachment points (c) Actual Design of the manipulator

Figure 3.3: Re-sized parallel manipulator concept design (inverted for clarity)

3D printed plates, and carbon-fiber links. Table 3.1 shows the manipulator dimensions. The dimensions allows the manipulator to fit within the workspace under the drone frame. All motors on the manipulator are controlled by the C++ open-source software, Pololu Mastro Servo Controller.

In Figure 3.3, the 8 legs attaching the base b to the moving platform p can be seen. All 8 motors work together to drive the mass of the legs and the moving platform.

Table 3.1: Physical Properties of the manipulator concept design

Symbol	Value	Description
D_1	0.110 <i>m</i>	Fixed length link (base joint and knee)
D_2	0.135 <i>m</i>	Fixed length link (knee and top platform joint)
L	0.773 <i>m</i>	Length (origin to the base attachment point)
M_{tm}	0.471 <i>kg</i>	Total mass of manipulator concept design
M_{mm}	0.093 <i>kg</i>	Total mass of moving components

Each leg, i , is attached to a servo on the base by a revolute joint. The servo drives a fixed length link, D_1 , to an angle θ_i from the plane of the base. The D_1 link is connected to a second fixed length link, D_2 , via a spherical *knee* joint, and the other end of the D_2 link attaches to the platform via a second spherical joint. The relative mounting positions of each leg is described in terms of angles ψ_{bi} and ψ_{pi} in the xy plane. γ_i is an angle between ψ_{bi} and the position of the link on the xy base plane, D_1 . Table 3.2 and 3.3 shows the coordinates of each leg attachment point.

3.2.2 Parallel Manipulator Inverse Kinematics

The purpose of inverse kinematics for this parallel manipulator is to find desired angles for each of the 8 driven revolute joints around the base platform. So, the

Table 3.2: Angular coordinates of leg attachment points to the base and moving platform

Leg(i)	$\psi_{b_i}(\text{radians})$	$\gamma_i(\text{radians})$	$\psi_{p_i}(\text{radians})$
1	0.3658	0.4196	0.2782
2	1.2050	0.4196	1.2926
3	1.9336	0.4196	1.8490
4	2.7758	0.4196	2.8634
5	3.5074	0.4196	3.4198
6	4.3466	0.4196	4.4342
7	5.0781	0.4196	4.9906
8	5.9194	0.4196	6.0050

top platform is driven to a desired pose in the manipulator's base coordinates. The transformation between the base and top platforms is described by Euler rotations in XYZ convention, thus the rotation matrix is defined as

$$R = R_z(\gamma)R_y(\beta)R_x(\alpha) \quad (3.1)$$

The homogeneous transform bT_p is used to map each leg's attachment point to the top platform, p_i , to its goal pose p_i^* in the base coordinates of the manipulator as shown in Equation 3.2

$$p_i^* = p_i {}^bT_p \quad (3.2)$$

Next, the Euclidean distance L_i^* is calculated as the direct distance between b_i and p_i^* for each leg. L_i^* is a virtual leg and it is the hypotenuse of the triangle formed

Table 3.3: Leg attachment positions to the top and base in manipulator base coordinates

Leg(i)	Base Connections			Top Connections		
	$b_{xi}(m)$	$b_{yi}(m)$	$b_{zi}(m)$	$p_{xi}(m)$	$p_{yi}(m)$	$p_{zi}(m)$
1	0.0722	0.0277	0	0.0717	0.0205	0
2	0.0277	0.0722	0	0.0205	0.0717	0
3	-0.0277	0.0722	0	-0.0205	0.0717	0
4	-0.0722	0.0277	0	-0.0717	0.0205	0
5	-0.0722	-0.0277	0	-0.0717	-0.0205	0
6	-0.0277	-0.0722	0	-0.0205	-0.0717	0
7	0.0277	-0.0722	0	0.0205	-0.0717	0
8	0.0722	-0.0277	0	0.0717	-0.0205	0

by the points b_i , p_i^* and the knee, m_i^* .

$$L_i^* = \|p_i^* - b_i\| \quad (3.3)$$

The spherical joint point, k_i^* between D_1 and D_2 is calculated through the transformation

$$k_i^* = (k_{xi}^*, k_{yi}^*, k_{zi}^*)^T = b_i + {}^{Servo}R_b(D_1, 0, 0)^T \quad (3.4)$$

where:

$$b_i = (b_{xi}, b_{yi}, b_{zi})^T \quad (3.5)$$

$${}^{Servo}R_b = R_z(\psi_{bi} \pm \gamma_i)R_y(\theta_i) \quad (3.6)$$

In the rotation matrix, ${}^{Servo}R_b$, the sum of the angles is used for odd-numbered legs, and the difference of the angles is used for even-numbered legs. As results,

$$k_i^* = \begin{bmatrix} k_{xi}^* \\ k_{yi}^* \\ k_{zi}^* \end{bmatrix} = \begin{bmatrix} D_1 \cos(\psi_{bi} \pm \gamma_i) \cos(\theta_i) + b_{xi} \\ D_1 \sin(\psi_{bi} \pm \gamma_i) \cos(\theta_i) + b_{yi} \\ D_1 \sin(\theta_i) + b_{zi} \end{bmatrix} \quad (3.7)$$

Thus fixed length links, D_1 , D_2 , can be described with Equation 3.7

$$D_1 = \|k_i^* - b_i\|, \quad (3.8)$$

$$D_2 = \|p_i^* - k_i^*\|, \quad (3.9)$$

For desired position and orientation, new sets of p_i^* and virtual legs L_i are calculated. The inverse kinematic solution, θ_i satisfies for all 8 joints

$$|L_i^*|^2 = (p_i^* - b_i)^T (p_i^* - b_i) \quad (3.10)$$

$$D_1^2 = (k_i^* - b_i)^T (k_i^* - b_i) \quad (3.11)$$

$$D_2^2 = (p_i^* - k_i^*)^T (p_i^* - k_i^*) \quad (3.12)$$

Combination of the above equations leads to

$$|L_i^*|^2 + D_1^2 - D_2^2 = 2(b_i - k_i^*)^T (b_i - p_i^*) \quad (3.13)$$

After substituting from Equation 3.4, Equation 3.13 becomes

$$\begin{aligned}
& |L_i^*|^2 + D_1^2 - D_2^2 = \\
& 2D_1(p_{zi}^* - b_{zi}) \sin(\theta_i) + \\
& 2D_1[(p_{xi}^* - b_{xi}) \cos(\psi_{bi} \pm \gamma_i) + (p_{yi}^* - b_{yi}) \sin(\psi_{bi} \pm \gamma_i)] \cos(\theta_i)
\end{aligned} \tag{3.14}$$

Finally, the desired angle of servo rotation, θ_i , is derived by Equation 3.14 using the trigonometric identity

$$\theta_i = \arcsin\left(\frac{c}{\sqrt{a^2 + b^2}}\right) - \arctan\left(\frac{b}{a}\right), \tag{3.15}$$

where:

$$\begin{aligned}
a &= 2D_1(p_{zi}^* - b_{zi}) \\
b &= 2D_1[(p_{xi}^* - b_{xi}) \cos(\psi_{bi} \pm \gamma_i) + (p_{yi}^* - b_{yi}) \sin(\psi_{bi} \pm \gamma_i)] \\
c &= L_i^{*2} - D_2^2 + D_1^2.
\end{aligned}$$

In b , the sum of the angles is used in the sinusoids for odd-numbered legs, while the difference of the angles is used for even-numbered legs

3.2.3 Sensorized Parallel Jaw Gripper

For rapid prototyping, LEGO's were utilized to construct the sensorized parallel jaw gripper for grasping tasks (see Figure 3.4). The gripper is operated by servomotors that react to tactile feedback from an inter-integrated-circuit(I^2C) compatible Time

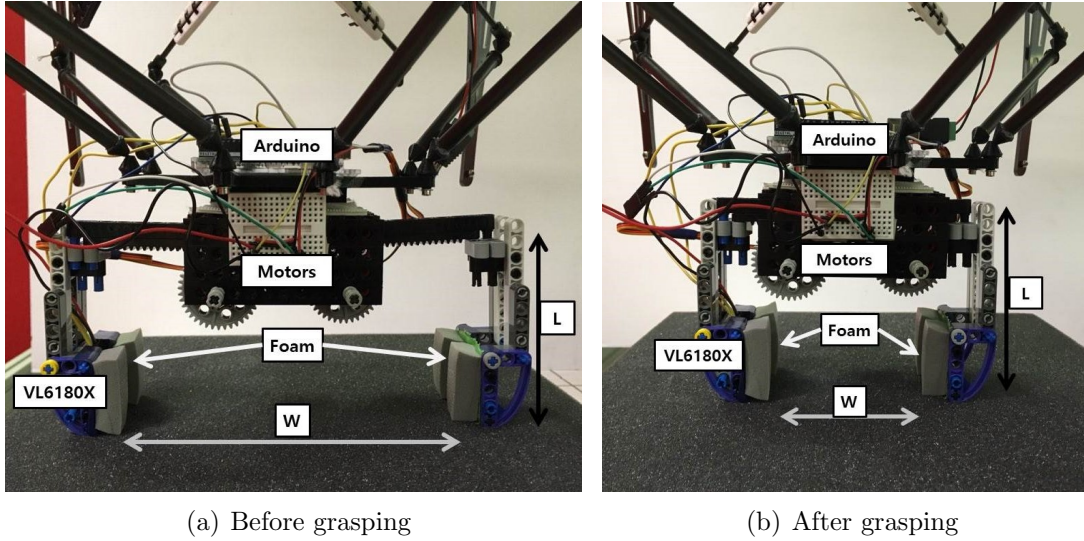


Figure 3.4: LEGO-Based sensorized parallel jaw gripper concept

Table 3.4: Physical Properties of the parallel gripper concept design

Symbol	Value	Description
W	$0.095-0.185m$	Width between grip and non-grip
H	$0.11 m$	Height of the gripper
M_{tg}	$0.234 kg$	Total mass of the gripper concept design

of flight(ToF) sensor, VL6180X (STMicroelectronics). The sensor is mounted at the right bottom side of the gripper in-hand. An I^2C compatible Arduino-Uno is used to operate the gripper and receive proximity range data from the sensor. Two pieces of foams are attached on each side to enhance grasping characteristics. The task begins when the object contacts the gripper. The physical properties of the gripper are listed in Table 3.4. The gripper is then attached to the manipulator's end-effector.



Figure 3.5: Lab automation drone prototype

3.2.4 Lab Automation Drone Prototype

Finally, a lab automation drone prototype is built with the Q450 quadcopter frame (see Figure 3.5). Four LD-Power 960kV motors with 24cm propellers are mounted on the frame. Additional landing gears are attached to create a 25cm square workspace under the quadcopter. A 11.1kV, 2200mAh Li-Po battery is connected for power source. An open-source autopilot, *Pixhawk*, is mounted for flight control. The flight data is stored and downloaded on an open-source software, Mission Planner. The payload is estimated to be 3.0kg, so the total weight of manipulator and gripper design is designed with a total mass of 0.798kg and a moving mass of 0.327kg. The parallel manipulator and the sensorized gripper are attached to the quadcopter's belly.

3.2.5 Test-and-Evaluation

The 4-DOF gantry-based platform in Fig. 3.6 is built for test-and-evaluation. The design is motivated by Systems Integrated Sensor Test Rig (SISTR) from [49]. The

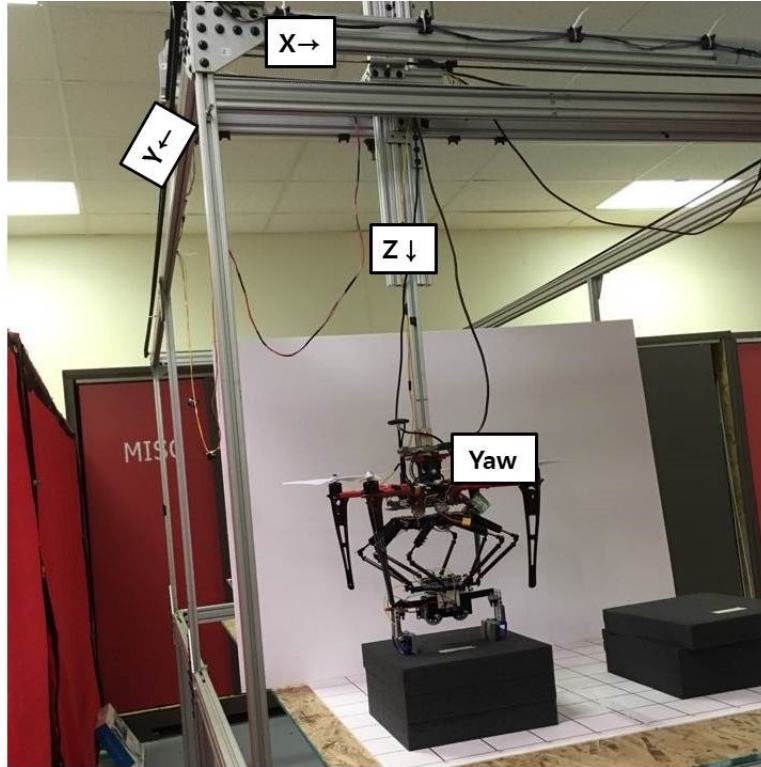


Figure 3.6: Gantry-based test-and-evaluation platform

gantry's

$$1.2m \times 0.5m \times 0.5m$$

workspace has the footprint to emulate a small HTS or a larger Section of HTS. The gantry runs Dynamixel motors to provide end-effector cartesianal (x, y, z) position and yaw ψ orientation.

The prototype lab automation drone is affixed to the gantry's end-effector for micro-plate grasping. A $90cm \times 60cm$ rectangular coordinate system was positioned below the drone to measure the accuracy of translation. The micro-plate is placed on the top of black-cube. The drone descends $10cm$ and grasps the micro-plate, then

Table 3.5: Rotation angle of revolute joint

Positions			
Store and Delivery		Pick-up	
Joint(i)	$\theta_i(\text{radians})$	Joint(i)	$\theta_i(\text{radians})$
1-8	0.0015	1-8	0.6881

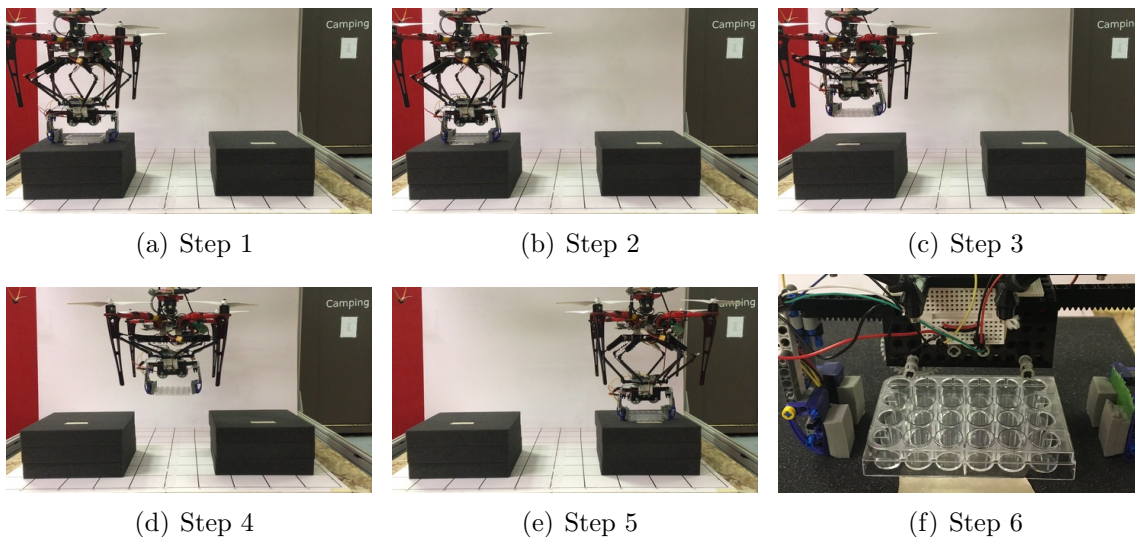


Figure 3.7: Micro-plate pick-and-place

delivers it to the target location. During the test, an empty micro-plate, a micro-plate with vitamin pills, and a micro-plate with juice sample are delivered from $(80,20,15)$ to $(20,20,15)$.

Table 3.5 describes the calculated revolute joint angles on each leg during the experiments. All 8 revolute joints are rotated with the same angles because the pick-and-place task only requires the end-effector motions in z-axis; hence, the same virtual length L_i are applied to calculations for the inverse kinematics.

Figure. 3.7 shows the sequence of recorded images during the test. The micro-plate is delivered gently. The result demonstrated precise micro-plate pick-and-place.

3.3 Testing-and-Evaluation Platform for Haptic-based Aerial Manipulation



Figure 3.8: Aerial manipulation with a haptics device. Operator feels reaction forces on the manipulator (inset); Inset shows manipulator grabbing a spring

Autonomous aerial manipulation has been studied for over a decade. The desired tasks have been achieved when the cases are simple: target object geometries are easily identified with computer vision; object rigidity is suitable to grasp; flight trajectories are mainly linear. Current challenges in autonomous aerial manipulation are the following: manipulating object that have complex geometries and a drone's ability to adjust to unexpected environmental changes.

Therefore, a more collaborative approach is proposed in [74]. The notion is that the worker performing the task can leverage the haptic assessment of object properties to collaboratively perform aerial manipulation. In such human-in-the loop approaches, haptic sensing can provide meaningful system information to the opera-

tor. This could yield collaborative drones that augment a worker’s ability to perform assessment and maintenance remotely.

Toward this vision, testing-and-evaluation (T&E) platform for haptic-based human-in-the-loop aerial manipulation is demonstrated (see Figure 3.8). The platform was designed in a gantry-based system with a haptic-based mobile-manipulating unmanned aerial vehicle (MM-UAV), and a commercial haptic device (Section 3.3.1-3.3.4). The flight trials validated and verified the efficacy of this platform (Section 3.3.5). The main outcome is that the platform could provide a safe and repeatable flight test environment for haptic-based aerial manipulation.

3.3.1 Mobile Manipulating Unmanned Aerial Vehicle

Mobile-Manipulation Unmanned Aerial Vehicles (MM-UAV) are a series of rotorcraft drones that have been designed, developed, and deployed for different tasks like valve turning, hose insertion, and visual servoing [37]. In Section 3.2, the latest version MM-UAV has been developed for high throughput systems. This MM-UAV has a tuck-and-stow arm (Figure 3.9). The parallel mechanism gives the end-effector six degrees-of-freedom, but can also be folded flat. This parallel-based arm is better at counter-balancing the payload as the arm maneuvers in the workspace.

3.3.2 Testing-and-Evaluation Platform

A gantry-based platform has been used for the testing-and-evaluation (T&E) of drones, sensor suites, controller design, path planning and aerial manipulation [49]-

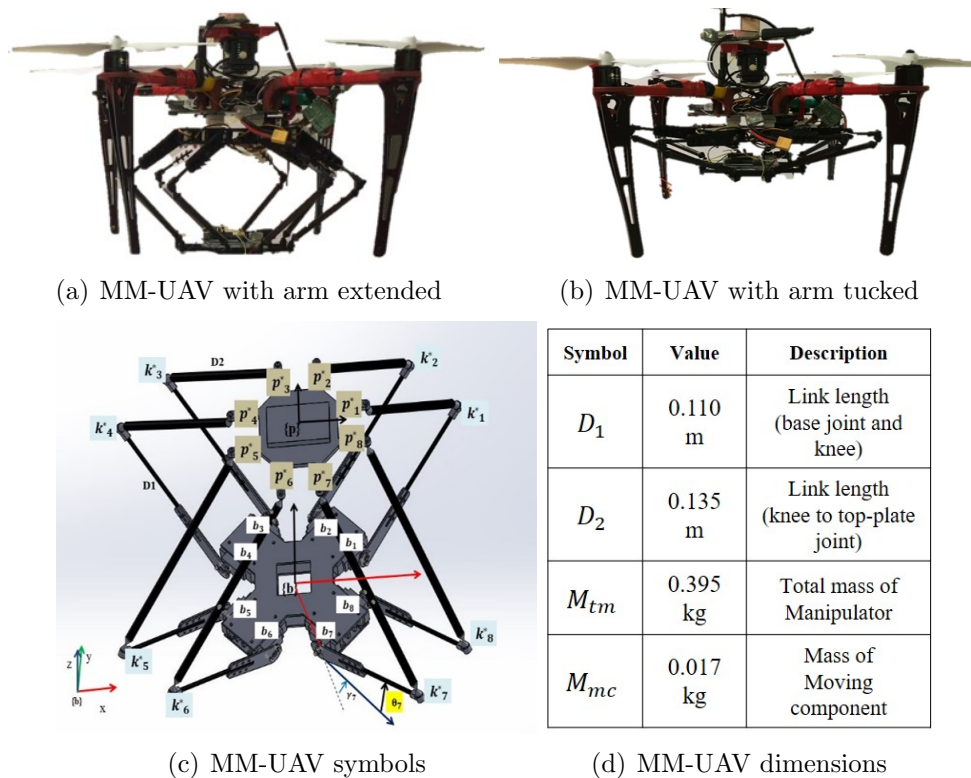


Figure 3.9: MM-UAV design

[54], called SISTR (Systems Integrated Sensor Test Rig). This $25 \times 25 \times 25$ cubic foot platform has included a model reference adaptive control to emulate aircraft motions. SISTR has included fans, lamps, and fog machines for the T&E in the presence of gusts, glare, and obscurants. SISTR enables one to perform indoor flight tests safely and analytically before validation-and-verification flights (without the gantry).

Mini-SISTR is a smaller scale version, $5 \times 4 \times 2$ cubic foot, of the room-sized one, was used (Figure. 3.10). The MM-UAV is mounted to the end of the gantry's vertical axis. The operator uses the commercially available 3D Systems haptics device (called Touch [90]) like a joystick; the device's encoder states transform into both gantry

motions (and thus the rotorcraft) and arm positions. Moreover, the forces felt by MM-UAV's end-effector are transmitted back to the 3D Systems haptic device. This empowers the operator to feel what the arm feels.

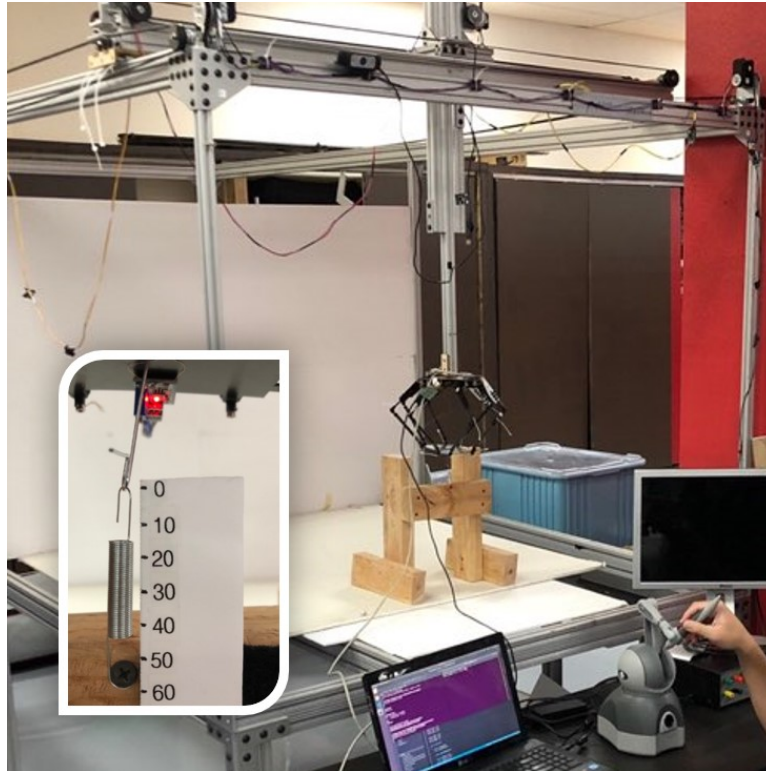


Figure 3.10: The Touch (lower right corner) is adjusted to command the gantry and MM-UAV arm (background) to grab a spring (inset)

3.3.3 Haptic Device Force Rendering

Providing haptic sensing could realize a more collaborative drone – one that augments the operator's abilities to assess and potentially repair infrastructure. Hooke's law has been selected as a logical first step for haptic feedback. The notion was to

have one end of spring fixed to a base. The operator would steer the MM-UAV over the spring and maneuver the arm to grab the spring's free end. The operator would then command the MM-UAV to displace the spring. The resulting forces would then be felt through the Touch. From this, the operator would then be able to ascertain spring displacement values. Figure 3.10 shows the notion's realization. Strain gauges were affixed to the MM-UAV's end-effector. An Arduino-based microcontroller acquired force measurements. This data was then transmitted to the Touch via the OpenHaptics software development kit [91].

Broadly speaking there are two categories of haptic devices. Admittance-based ones like the Hapticmaster [92] returns the corresponding displacement values with force measurements. On the contrary, impedance-based ones like the Touch does the opposite; the corresponding force from displacement measurements is returned. As such, designing a suitable strain-gauge sensor revolves around the substrate's thickness. Equation 3.16 depicts the relationship between the elastic force F_{total}^{spring} , the spring constant K , and the displacement x . Initial tension force F_0^{spring} captures the spring's initial state. The range of the calibrated forces is given by Equation 3.17.

$$F_{total}^{spring} = F_0^{spring} + Kx \quad (3.16)$$

$$F_{min}^{sensor} \leq F^{sensor} \leq F_{max}^{sensor} \quad (3.17)$$

$$F_{min}^{sensor} \leq F_0^{spring} \quad (3.18)$$

To determine a suitable substrate thickness, Equation 3.18 should be satisfied.

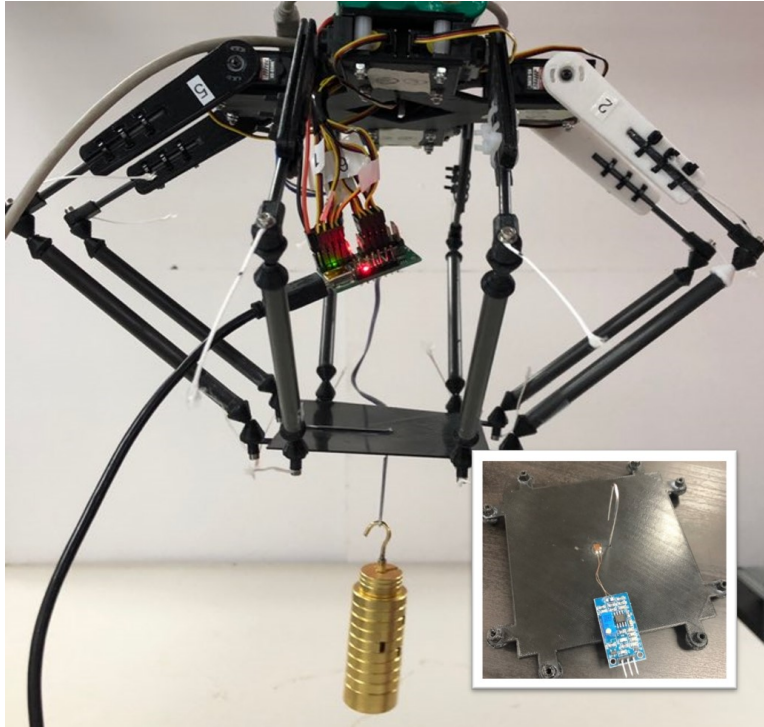


Figure 3.11: The weight is applied (bottom), a substrate is constructed with strain gauge, a pin to grab a spring (inset)

Several substrates were constructed, strain gauges mounted, test weights applied, measurements were acquired, and signal conditioned in Figure 3.11. The net effect resulted in a 1 *mm* substrate which yielded a sensing range of $0.12 \text{ N} \leq F^{sensor} \leq 6.29 \text{ N}$.

The Touch has a 6-DOF stylus. The stylus serves as a joystick to maneuver the drone positioning. It also allows the operator to feel the rendered forces through three linear positions. Because the sensed force is scalar, it is broken down into three-dimensional components like in Equation 3.19.

$$\vec{F}^{rendered} = F^{sensor} \left(\frac{\vec{r}_{joystick}}{\|\vec{r}_{joystick}\|} \right) \quad (3.19)$$

where:

$$\vec{r}_{joystick} = x_{joystick} \cdot \hat{i} + y_{joystick} \cdot \hat{j} + z_{joystick} \cdot \hat{k}$$

$$\|\vec{r}_{joystick}\| = \sqrt{x_{joystick}^2 + y_{joystick}^2 + z_{joystick}^2}$$

$\vec{r}_{joystick}$ is the position of the joystick provided from the haptic device. Hence, this renders the exact scalar force to the operator regardless of the joystick position. The Touch's limit switches restrict force measurements to $\pm 3 N$ in all three dimensions. This was kept in mind by scaling the values returned by the spring.

3.3.4 Haptic Manipulation in Testing-and-Evaluation Platform

Table 3.6: The joystick position to MM-UAV arm position

Position	Haptic Device	MM-UAV arm
X	-0.217 ~ 0.213 m	-0.15 ~ 0.15 m
Y	-0.071 ~ 0.093 m	-0.15 ~ 0.15 m
Z	-108 ~ 204 m	-0.00 ~ 0.23 m

Haptic manipulation was implemented in the testing-and-evaluation platform. One end of the spring was fixed to the ground in the gantry's workspace (see Figure 3.12). The operator used the haptic device joystick to command the arm to grab

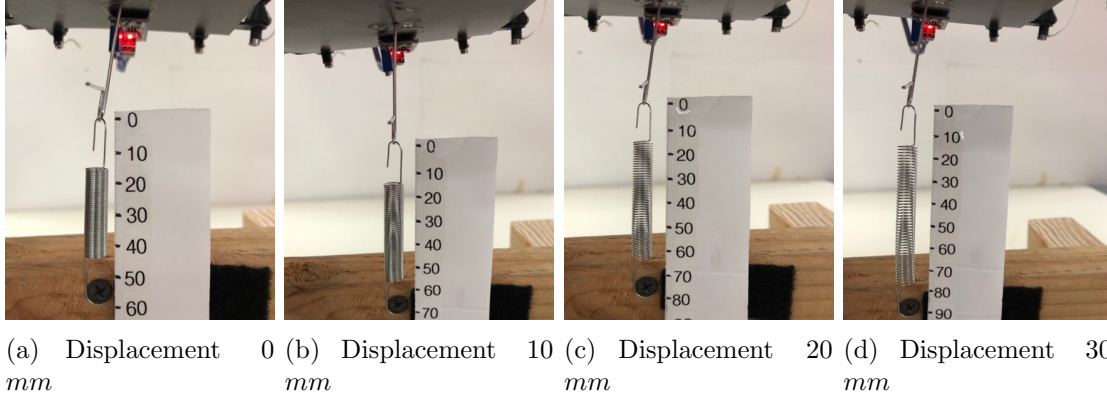


Figure 3.12: Haptic manipulation in testing-and-evaluation platform (origin 60 *mm*)

the spring’s free end. Table 3.6 shows that joystick positions are translated into the arm positions. The operator then ascended the arm in the vertical axis. Figure 3.13 shows that the end-effector’s position inputs are proportional to the measured forces. These forces were scaled by 50% to avoid triggering the Touch’s limit switches (3.3*N* in all axes). One can also observe that there was about 0.4 second lag between the force sensor and the Touch. Furthermore, the end-effector position inputs were larger than the spring displacement. This was attributed to the arm’s motor torques which were deemed to be slightly underpowered when extending the spring.

3.3.5 Flight Trials for Validation-and-Verification

The haptic-based MM-UAV was test flown in a motion-capture arena (see Figure 3.14). The spring test stand used in the gantry was positioned in the arena’s workspace and flight trials were performed to evaluate the efficacy of the design.

The manipulator is attached to the belly of a DJI Q450 quadcopter. For stable

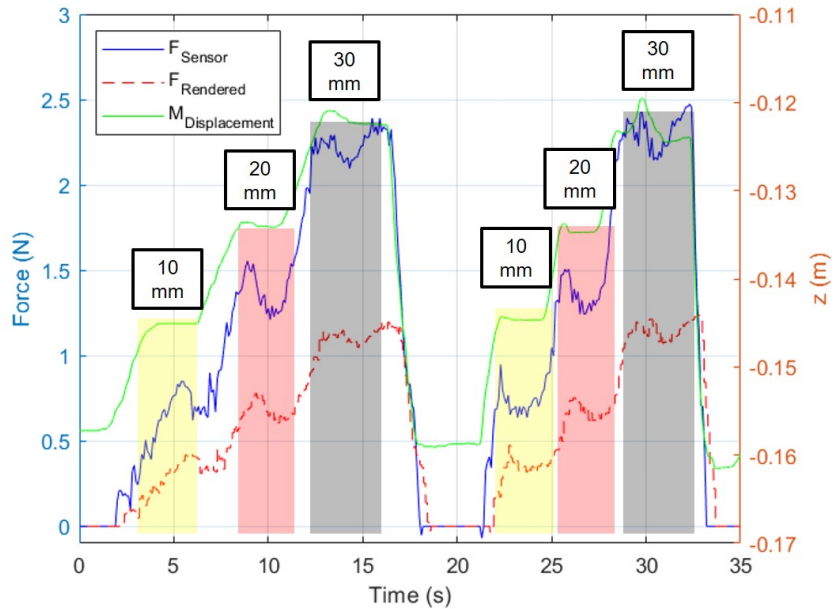


Figure 3.13: Haptic manipulation in testing-and-evaluation platform results

hovering, a cascade controller was employed (see Figure 3.15). The controller scheme is detailed in Section 3.1. Motion capture acquires the MM-UAV’s position as represented by the outer loop. This outer loop consists of a proportional-derivative (PD) controller running at 100 Hz to overcome disturbances.

Flight trials were conducted. A motion capture marker was placed on the spring to monitor the amount of deflection. The operator first commands the drone to take-off and fly above a target location $(0, 0, 0.82)$ in meters. This places the vehicle above the spring. The operator then uses the haptic device to servo the arm and grab onto the spring’s free end. The spring is stretched when the arm ascends. The operator feels these reaction forces through the Touch. Figure 3.16 is an image sequence from a recorded video of a flight trial. Figure 3.18 describes trajectories of MM-UAV and



Figure 3.14: MM-UAV and spring test bench in the motion capture arena being controlled by the Touch haptic device

its arm near the target location in the trials. One observes the similarity of this figure with the one conducted in testing-and-evaluation platform (see Figure 3.13).

Motion capture data was used for further evaluation. Flight trials ran for 80 seconds. The spring force was captured and rendered between 63 and 66 seconds (see Figure 3.17). The top graph plots the position error with respect to the desired posi-

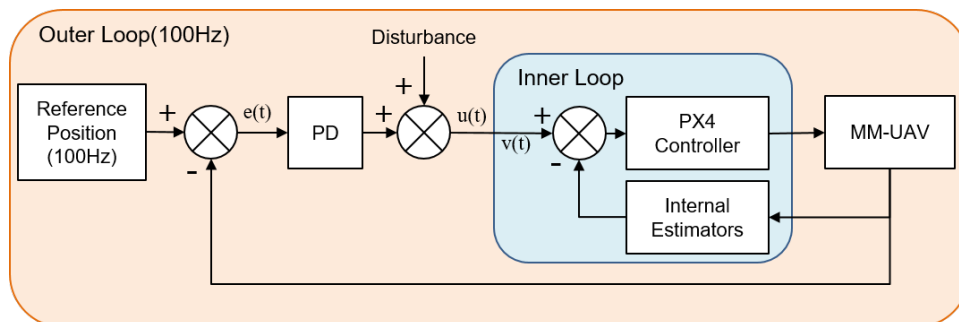


Figure 3.15: The cascade control system scheme

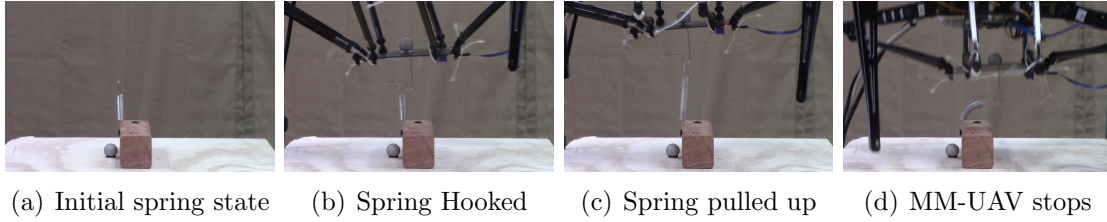


Figure 3.16: Flight trial closeup view

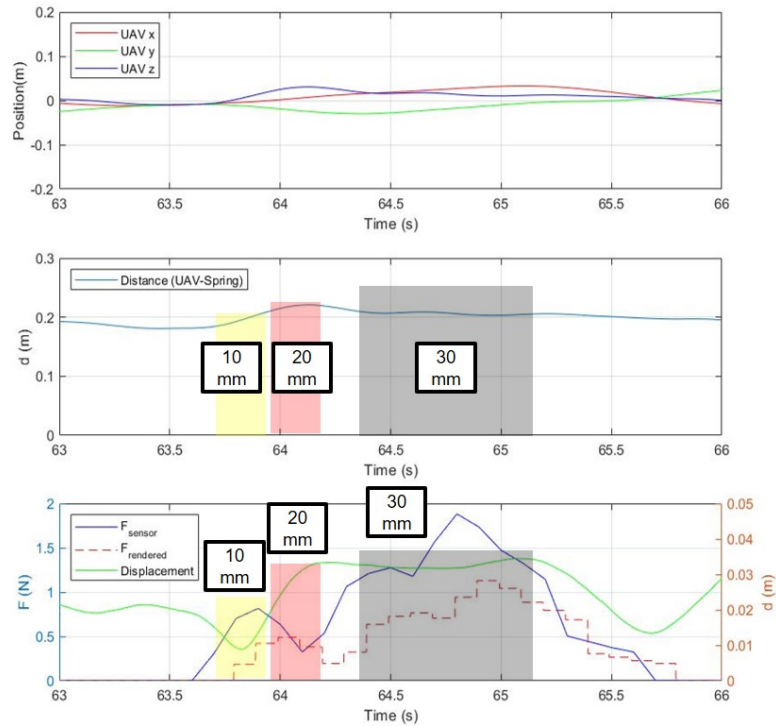
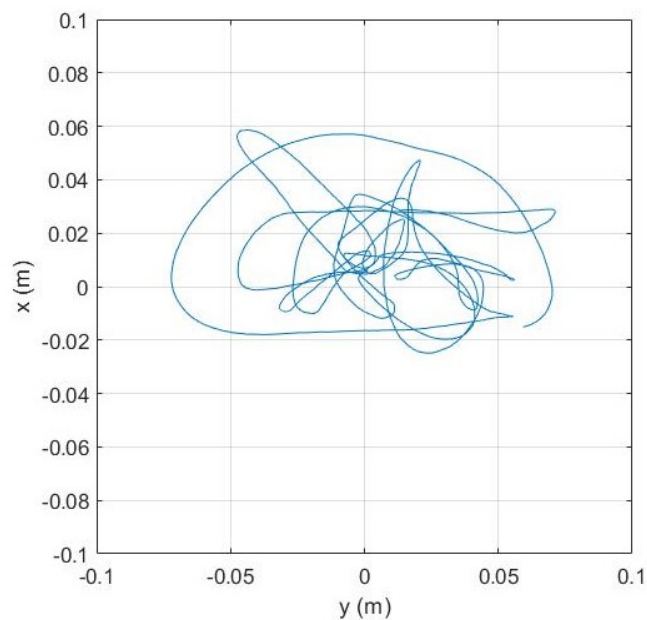
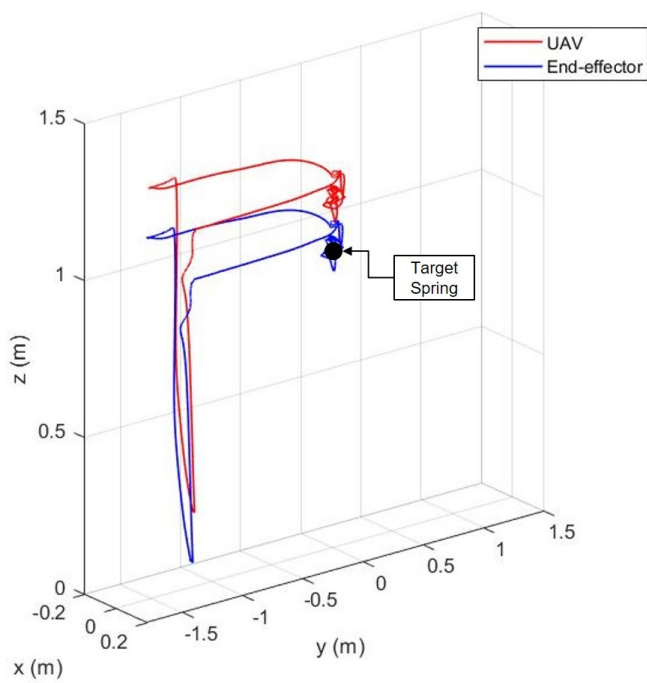


Figure 3.17: Flight trial results during force rendering

tion. The center graph plots the distance between the drone and spring. The bottom graph plots both the measured and rendered forces and spring displacement measured by motion capture. One also observes that between 63.5 and 64.5 seconds, flight fluctuations cause incorrect for measurements. But once the flight became stable, the measured forces (marked in black) match values from the testing-and-evaluation platform (see Figure 3.13). The net effect is the gantry’s efficacy; testing-and-evaluation



(a) MM-UAV's arm X-Y position history near the target location



(b) MM-UAV flight trajectories

Figure 3.18: MM-UAV flight trials description

platform is suitable for *pre-flight* testing in a safe and repeatable manner before flight trials are conducted on the real vehicle.

3.4 Human-Drone Interface for Aerially Manipulated Drilling with Haptic Feedback



Figure 3.19: Aerial manipulation with a customized haptic drill press. Operator feels reaction forces on the manipulator (inset); Inset shows a rotary drill manipulator drill pressing on a plywood board

With promising results from the work in Section 3.3, a concept for haptic-based human-in-the-loop aerial manipulation to remotely work on surfaces is presented [75] (see Figure 3.19). This concept stems from the collaborative project with the US Department of Transportation (DOT) for bridge maintenance, inspection, and repair. Surfaces like the decks and bottoms of bridges often need prep work like drilling

pilot holes. The concept addresses drill press tasks as a case study. The drill press is generally utilized for several tasks: material assembly, bridge repair, and sensor insertion. In such tasks, haptic assessment could enable the operator-in-the loop to inspect the material condition and increase task dexterity. Therefore, a human-drone interface is designed to remotely drill with a mobile-manipulating drone and a customized haptic drill press (Section 3.4.1-3.4.4). Five rigid materials were selected for the proof-of-concept trials (Section 3.4.5-3.4.6). The results from the trials proved that the operator's handling expertise helped the drone successfully perform drill tasks on the materials.

3.4.1 Customized Haptic Drill Press Design

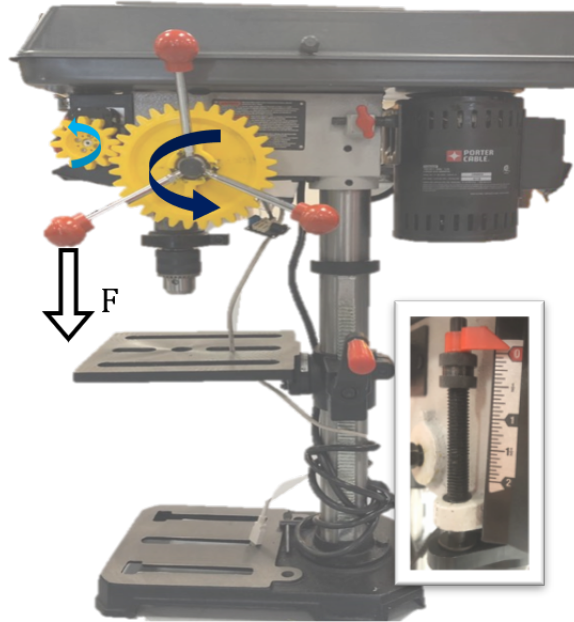


Figure 3.20: Customized haptic drill press design; drill chuck position (inset)

To provide the operator with haptic feedback, the goal is to render the forces that are transmitted from the drill mounted on the drone. The rationale is that such a design empowers the operator to feel the forces encountered by the drill. Thus, a conventional Porter-Cable drill press with a Dynamixel MX-28 motor is augmented (see Figure 3.20). The augmentation has a single degree-of-freedom rotary handle that drives a drill chuck up and down linearly (0 to 0.05 m). The motor reads the chuck position, senses applied torques, and also generates sufficient stall torque (2.5 Nm at 12 V). It is mounted on the left of the drill press and is linked to the rotary handle by two 3D-printed gears. Both gears are designed to have 0.02 m and 0.06 m radius respectively. The motor senses the torque inputs as the operator rotates the handle while simultaneously provides torque feedback to the operator.

3.4.2 Aerial Manipulator Concept Design

To design a robotic drill manipulator, hand-drills are considered. The drill press is operated by a binary (on-or-off) power system and the drill chuck motion is linear. The weight of a drone's payload should be considered. Most hand-drills are over 1.5 kg and would require a more complex gripper for the power grasp. Hence, Dremel's cordless rotary tool is selected for the manipulator design. This tool is chosen because it provides performances at speeds ranging from 5,000 to 30,000 RPM and has a collet for 7/64" to 1/8" drill bits. Drill performance is demonstrated in Figure 3.21. Seven materials are selected for experimentation: CAT PS2-10 oriented standard board sheathing plywood (12" x 24" x 7/16); Charlotte 4" diameter PVC pipe (4" x 10" x

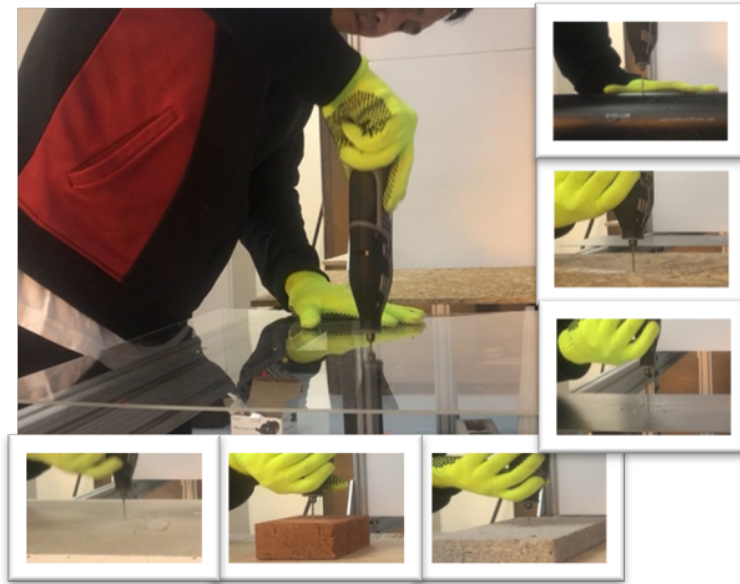


Figure 3.21: Selected tool performance test: acrylic sheet, PVC pipe, plywood board, metal sheet, concrete, brick, and drywall (clockwise, inset)

1/4"); Simbalux Acrylic sheet (12" x 12" x 1/8"); Hilman weld steel sheet 16GA (12" x 24" x 1/16"); Liftlight Drywall Panel (12" x 12" x 1/2"); Lowe's Concrete Block (5" x 16" x 2"); and Lowe's Red Clay Brick (3" x 8" x 2.25"). Material thickness is considered with the size of drill-bit. DeWalt 7/64" diameter industrial cobalt drill bit (1.5" length) and Bosch 1/8" diameter concrete drill bit (1.5" length) are mounted onto the rotary tool. During experimentation it was observed that the tool could not penetrate concrete and brick. Hence, the rest of materials are used for the proof-of-concept. A Dynamixel MX-28 is selected as the manipulator for the tool. This tool is attached to the Dynamixel's aluminum joint (see Figure 3.22). To mount the drill manipulator, a Powerday S550 hexacopter is selected. The maximum payload is calculated to be 3.6 kg with six 920 kv brushless motors, 9" self-tightening propellers,

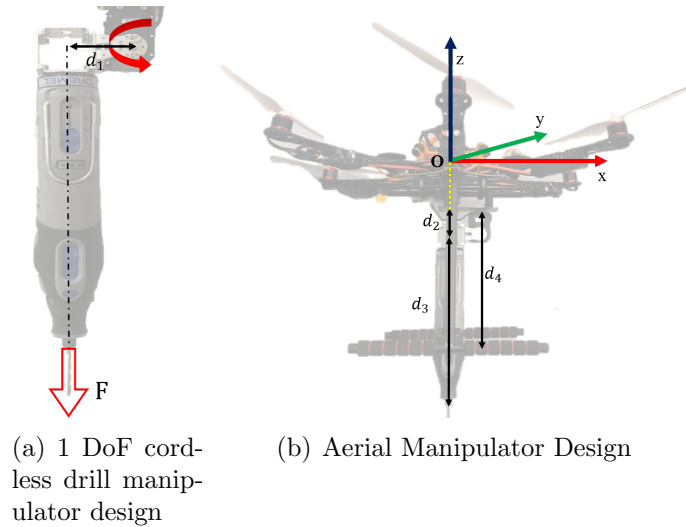


Figure 3.22: Aerial manipulator with 1-DoF drill manipulator design

and a 11.1 V 2200 mAh 3S Li-Po battery. The Pixhawk4 is mounted to control the rotorcraft. Finally, the drill manipulator is attached to the underside of rotorcraft. The manipulator is placed under the drone’s center-of-gravity to help counter-balance the drone during flight. Table 3.7 shows the physical properties of the concept aerial manipulator.

3.4.3 Force Rendering Limit for Target Material Selection

The haptic drill press begins rendering forces when the drill manipulator contacts materials. All materials have properties such as density, shear modulus, and tensile strength. Such properties could impact the amount of generated forces on the drill manipulator. Forces that are over-rendered could damage the system. Hence, the force rendering limit is derived from selected test materials. First, both Dynamixels on the drill press and the drill manipulator are calibrated, and then a linear regression

Table 3.7: Physical Properties of Aerial Manipulator

Symbol	Value	Description
d_1	0.05 <i>m</i>	Length between Dynamixel joint and rotary drill
d_2	0.045 <i>m</i>	Length between drone belly to rotary drill)
d_3	0.29 <i>m</i>	Rotary drill length with a drill bit
d_4	0.21 <i>m</i>	Height of drone's workspace
M_{arm}	0.79 <i>kg</i>	Total mass of 1-DoF drill manipulator
M_{total}	2.79 <i>kg</i>	Total mass of aerial manipulator

is performed (see Figure 3.23). Dynamixel provides a torque sensing value from 0 to 1023, but it is recommended to sense less than the stall torque (2.4 *Nm* at 12 *V*) [96]. Therefore, the torque sensing value is limited to a maximum of 600. As a result, the drill manipulator and the drill press are set to have a maximum force sensing limit of 48 *N*, and 127 *N* respectively. Additionally, the weight of the aerial manipulator is considered. The drill press task is being executed while the rotorcraft hovers, and the drill bit is the only contact point to the test material. Thus, the rotorcraft weight was calculated to 27 *N*. The force rendering limit is summarized as follows:

$$F_{\text{rendered}} < W^{\text{am}} \leq F_{\text{max}}^{\text{dm}} \leq F_{\text{max}}^{\text{dp}} \quad (3.20)$$

where F_{rendered} is the force rendered from the drill manipulator to the drill press and W^{am} , $F_{\text{max}}^{\text{dm}}$, and $F_{\text{max}}^{\text{dp}}$ are aerial manipulator weight and the maximum force sensing limits of the drill manipulator and the drill press respectively. This force rendering

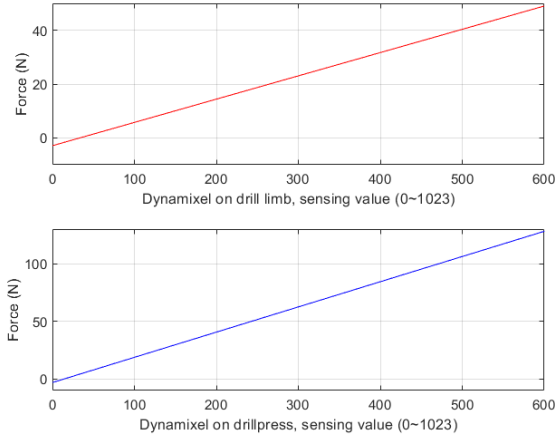


Figure 3.23: Dynamixel calibration results: drill manipulator (top) & drill press (bottom)

limit enables the operator to select suitable test materials for the proof-of-concept flight trials.

3.4.4 Sensitivity Gain

To simulate proper haptic feedback, the varied response of operators due to different body sizes and strength is considered. To capture this response, α is called as sensitivity gain and is proposed to amplify or reduce the sensed raw force for rendering.

$$F_{\text{rendered}} = F_{\text{raw}} \cdot \alpha \quad (3.21)$$

where F_{raw} is the initially sensed raw force from the drill manipulator and F_{rendered} is the rendered force to the haptic drill press. This force amplification or reduction assists the operator to distinguish drill press tasks such as initial contact; drill-in;

drill-out. This allows the operator to assess material properties to perform drill press tasks. Because the rendered force gives an impact on the drill press system, Equation 3.20 changes to:

$$F_{\text{raw}} < W^{\text{am}} \leq F_{\text{max}}^{\text{dl}} \quad (3.22)$$

$$F_{\text{rendered}} \leq F_{\text{max}}^{\text{dp}} \quad (3.23)$$

In gantry-based and flight trials, the operator tunes α while drilling different materials. This stops when the operator sensitively feels the rendered forces.

3.4.5 Proof-of-Concept Trials in Mini-SISTR

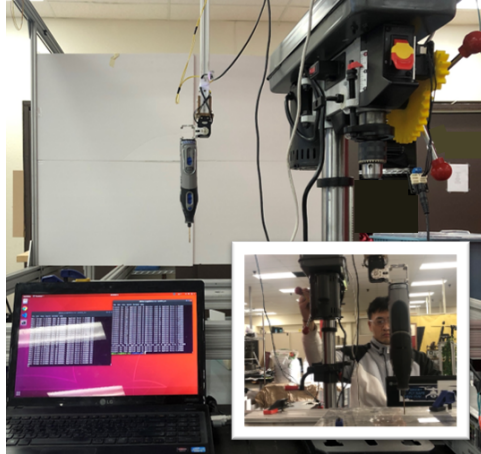


Figure 3.24: The haptic drill press (top-right), drill manipulator (background), and operator pressing the drill onto a test material (inset)

Mini-SISTR (Systems Integrated Sensor Test Rig), a gantry-based platform for emulating drone motion, is built for test-and-evaluation in Section 3.2.2. This plat-

form provides safe indoor test flight environments (see Figure. 3.24). For proof-of-concept, the drill manipulator is mounted to the end of the gantry's vertical axis. The operator uses the customized haptic drill press to control the altitude of the gantry manipulator. The Dynamixel mounted on the drill press reads the drill chuck position and transforms this position into the manipulator's altitude (and thus the rotorcraft's altitude). Forces are sensed when the manipulator contacts selected test materials. The contact pushes the manipulator joint to generate torques. These torques are sensed and converted into forces by dividing with d_1 . The forces are transmitted back to the drill press by computer. This haptic integration allows the operator to feel what the drill manipulator is feeling as it contacts the material.

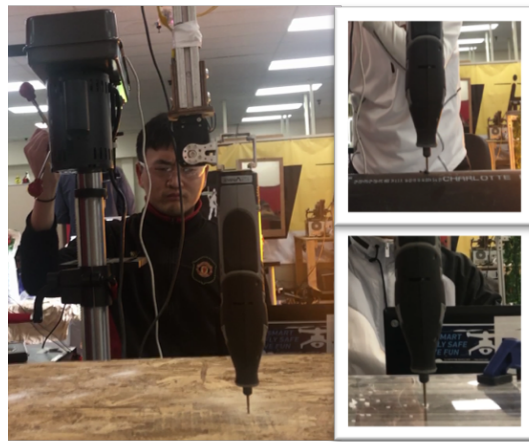


Figure 3.25: Haptic drill press on plywood board (left), PVC pipe (Top inset), Acrylic sheet (Bottom inset)

Finally, five materials, plywood board, PVC pipe, acrylic sheet, drywall, and rolled steel, are clamped to a test-rig on the gantry for drill press trials (see Figure 3.25).



(a) Drywall (Force captured)
 (b) Steel sheet (Contact not captured)
 (c) Steel sheet (Skating)

Figure 3.26: Unsuitable materials for haptic drill press

The operator manipulates the haptic drill press rotary handle in order to control the altitude of the gantry manipulator. The gantry then descends the manipulator. When the manipulator contacts a test material, torques are sensed and converted into raw forces using the right-hand rule.

Table 3.8: Gantry Haptic Drill Press Results Summary

Materials	F_{raw} Mean (N)	F_{raw} Standard Deviation (N)	Sensitivity (α)	Tensile Strength (N/mm^2)
Plywood	-1.4598	0.3907	15	27.57
PVC	-3.7786	0.8374	10	40.13
Acrylic	-5.3287	0.7075	5	68.94

The manipulator weight is offset. The offset helps the operator sense forces only by the contacts. F_{raw} is limited to 27 N , low-pass-filtered, multiplied with α , and

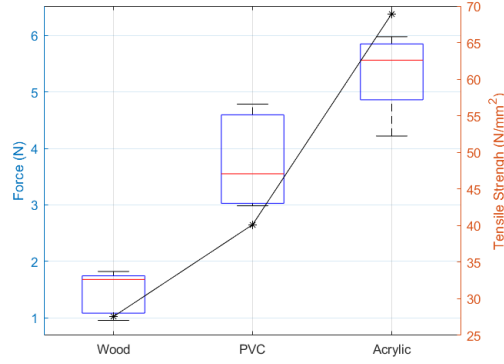


Figure 3.27: Haptic drill press in mini-SISTR results summary (raw force value sign changed for better understanding)

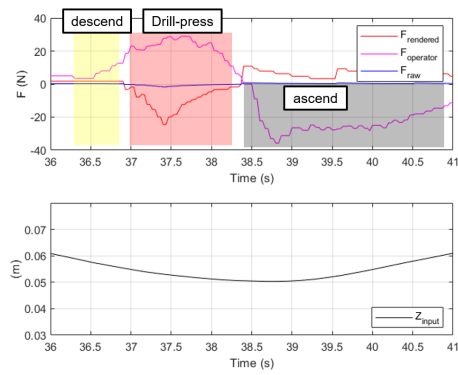
then rendered to the drill press (see Equation 3.24, 3.25).

$$F_{\text{filtered}}(t) = \frac{\tau}{\tau + t_s} F_{\text{filtered}}(t - 1) + \frac{t_s}{\tau + t_s} F_{\text{raw}}(t) \quad (3.24)$$

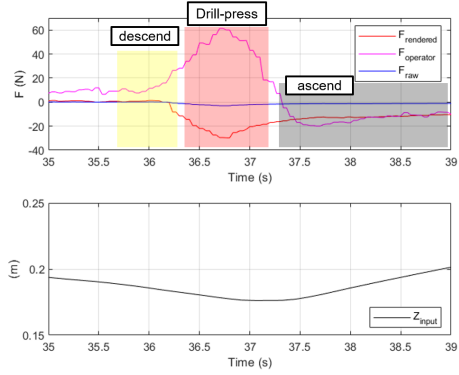
$$F_{\text{rendered}}(t) = F_{\text{filtered}}(t) \cdot \alpha \quad (3.25)$$

α is tuned in the trials, as mentioned in Section 3.3.4. Each of the test materials is drill pressed five times. Figure 3.26 identifies the unsuitable materials for the trials. The drywall was very easy to drill through, thus, F_{raw} was not captured due to low reaction forces. Furthermore, the manipulator was skating on the steel sheet. It was found that due to the material properties of the steel sheet, a drill press force higher than F_{raw} was required. This violates Equation 3.22. Thus, the results are addressed with the rest of materials, and these unsuitable materials are ignored in experimentation.

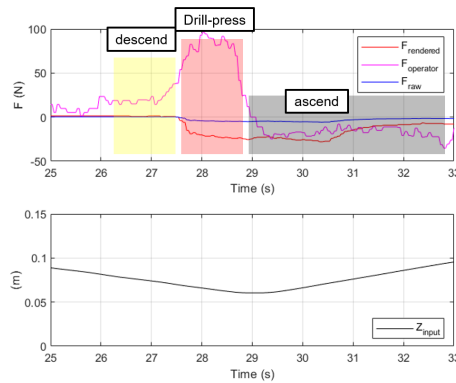
In Figure 3.28, the top graph plots raw forces, rendered forces amplified by α , and



(a) Plywood board



(b) PVC pipe



(c) Acrylic sheet

Figure 3.28: Haptic drill press in gantry-based system results; Each figure displays force (top) & the manipulator's height (bottom)

operator input forces. The bottom graph plots the drill manipulator altitude input from the drill press. The operator's force inputs are positive when the manipulator descends. The operator's input increases to counter-act the rendered force while the drill contacts the materials. One can also observe that there are existing rendered forces after the manipulator is retracted from materials. This occurred because pull-off task changed the offset. Furthermore, the material tensile strength is found to be proportional to the sensed raw force (see Table 3.8 and Figure 3.27).

3.4.6 Proof-of-Concept Flight Trials

The flight trials are implemented for proof-of-concept (see Figure 3.29). Flight tests serve to verify-and-validate the design performed in mini-SISTR. The operator remote station consists of the haptic drill press, a main computer, and a power supply for the dynamixel. The drone's flight environment and workspace are in a motion capture arena. The workspace is two meters away from the remote station and assembled using Everblock Modular Building Blocks that are broadly used in modular construction research [15]. The test materials, plywood board, PVC pipe, and acrylic sheet are clamped to the workspace for drill press tasks.

For flight stability, the aerial manipulator controller has a proportional-integral-derivative (PID) compensator with anti-windup. The gains are tuned to overcome disturbances from the drill manipulator and errors from the internal estimators (see

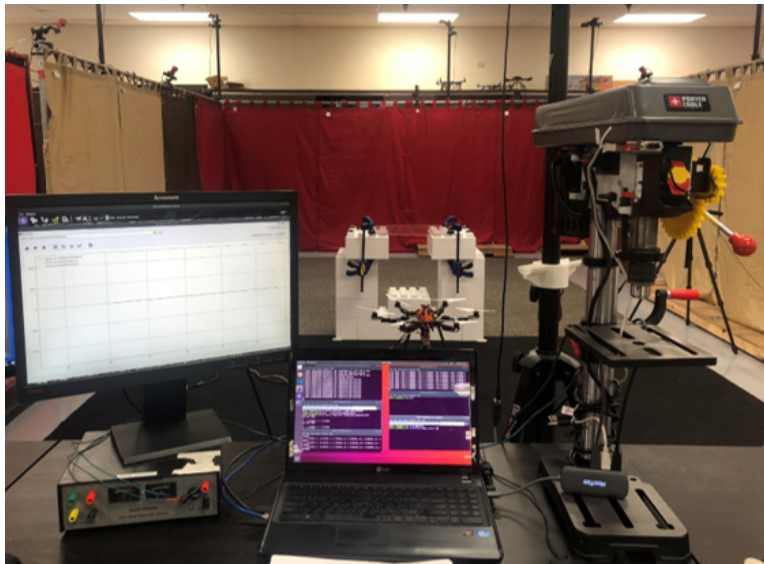


Figure 3.29: Flight environment and workspace;

Figure 3.30). Flight trials were conducted five times with each of the materials. Motion capture markers were placed on the workspace to display the target location. The operator first commands the drone to take-off and fly above a target location. This places the vehicle above the materials. The operator then manipulates the drill press rotary handle to descend the drone’s manipulator to the materials. The forces are sensed when the manipulator contacts on materials. α is tuned in the trials. The operator feels these rendered forces through the drill press. Figure 3.31 describes flight trial results. Figure 3.33 displays a series of recorded images from the flight trials. Figure 3.32 and Table 3.9 summarizes the results. One observes the similar plot-form of the results with the ones conducted in the gantry (see Figure 3.27). Flight trials ran for 85 seconds. The reaction forces were sensed and rendered between 55 and 65 seconds. The top graph plots raw forces, rendered forces amplified by α , and operator input forces. The center graph plots the rotorcraft altitude inputs from the drill press. The bottom graph plots the position error by the difference between the current and the desired position of the rotorcraft. One also observes that flight fluctuations in

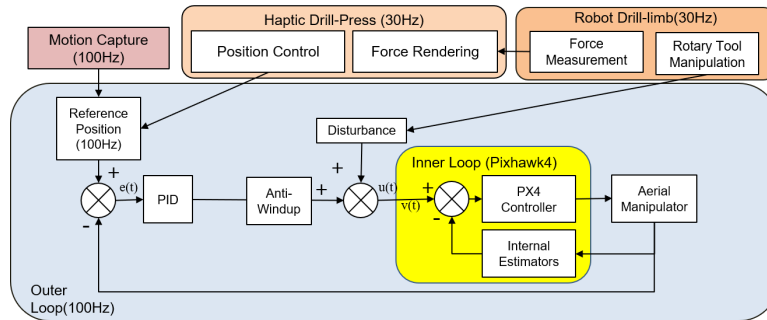
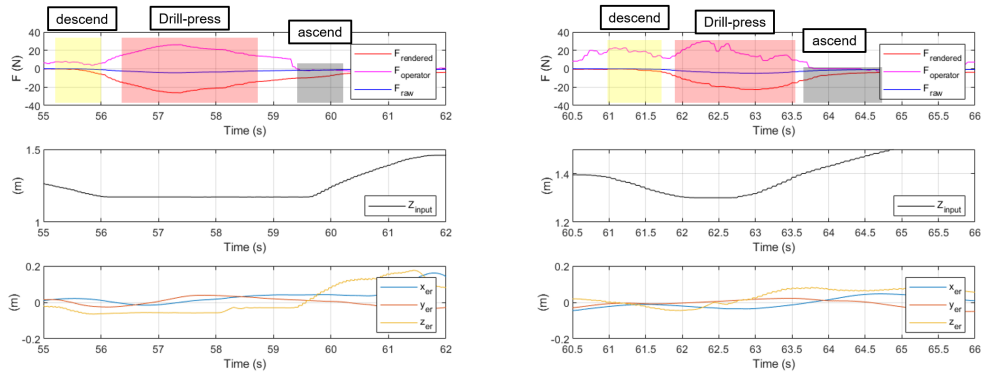
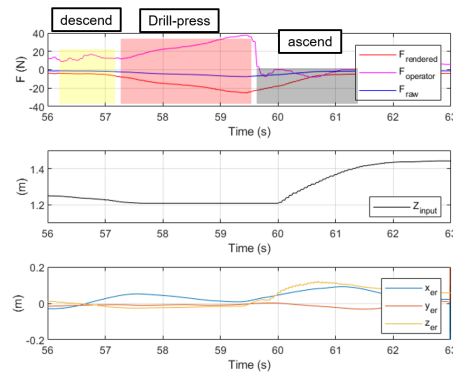


Figure 3.30: Overall system scheme



(a) Plywood board

(b) PVC pipe



(c) Acrylic sheet

Figure 3.31: Flight trial results

drill press increased the force measurements. Thus, the operator reduced α from the gantry to about a half to feel similar forces to the gantry ones through the drill press. (see Table 3.9).

Table 3.9: Aerial Drill Press Test Flight Results Summary

Materials	F_{raw} Mean (N)	F_{raw} Standard Deviation (N)	Sensitivity (α)	Tensile Strength (N/mm^2)
Plywood	-3.93	0.84	6	27.57
PVC	-5.70	0.78	4	40.13
Acrylic	-7.33	1.83	3	68.94

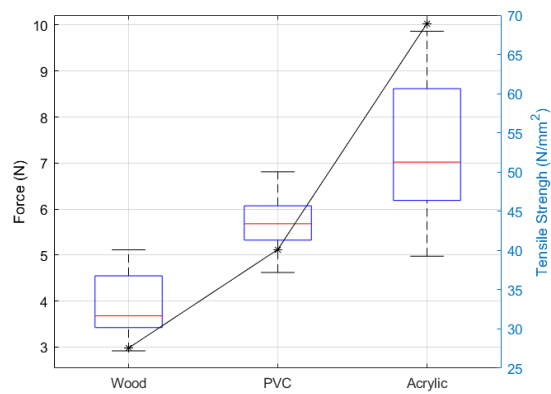
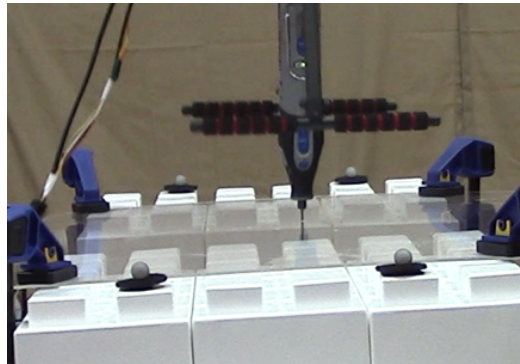


Figure 3.32: Aerial drill press test flight results summary (Raw force value sign changed for better understanding)



(a)

(b)



(c)

Figure 3.33: Flight test closeup view from left to right; Plywood board, PVC pipe, Acrylic sheet

CHAPTER 4 GENERAL OBJECTIVES

Lab automation drone presents potential use of aerial manipulation in high throughput systems (Section 3.2). Haptic-based human-in-the-loop aerial manipulation gives another solution to existing challenges in the state-of-art autonomous aerial manipulation (Section 3.3-3.4). Including these works, the state-of-art aerial manipulation has completed the desired tasks when the operator and the aerial manipulator are at the same location. Thus, new challenges for aerial manipulation arise when the task has to be done beyond the operator's line-of-sight; aerial manipulation has to provide the operator tele-presence; the operator must experience the senses and actions transported to and from the drone.

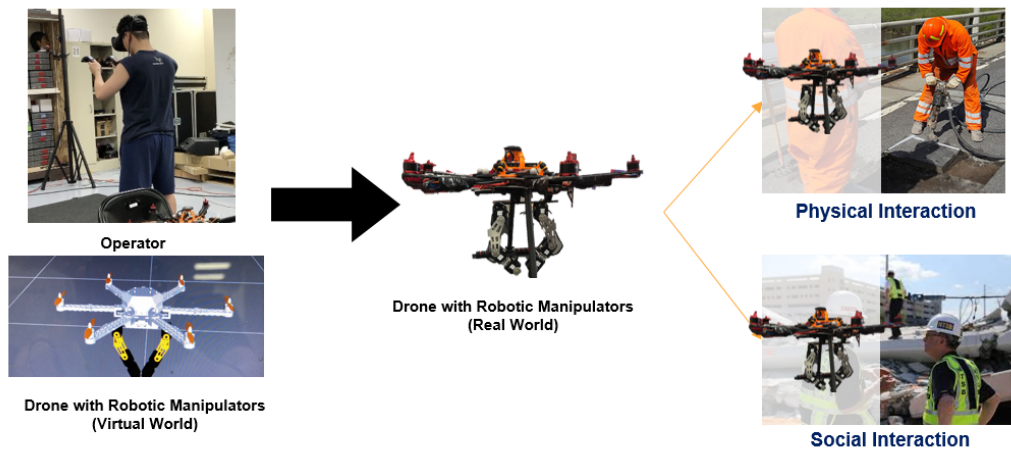


Figure 4.1: Human-embodied Drone Notional Concept

Reiterating the introduction, an immersive framework is integrated into the haptic-based human-in-the-loop aerial manipulation platform to address these challenges. Immersive technologies like augmented and virtual reality (AR/VR) have been exponentially growing recently. Through VR or AR devices, a user can identify themselves, and interact with surrounding environments in the virtual world, like an *Avatar* [76]-[78]. Next to the human-in-the-loop approach, this technology could lead to a human-embodied drone interface. The notion is that a mobile manipulating drone that embodies an operator in both the virtual/real world to dexterously perform the desired tasks (see Figure 4.1). The operator, using VR or AR devices, can leverage the drone to physically interact with objects and socially interact with on-site workers.

This differs from telepresence aerial manipulation in [65]: Real-time vision sensing provides physical layout of the remote area in 2D and 3D; the operator socially interacts with on-site workers; the operator's body gestures are converted and mapped into a mobile-manipulating drone. This is also different from simple communication (i.e. a Skype tablet [79] or a quadcopter with a smartphone [80]).

Toward this vision, this chapter presents two concepts of the human-embodied drone. The first concept demonstrates that the drone performs a simple pick-and-place task (Section 4.1) [81]. The second one demonstrates the drone with more complex tasks like horizontal drilling, peg-in-hole, and lock-unlock door (Section 4.2).



Figure 4.2: Human-embodied drone performing tasks in real world (left), operator in VR station (top right), View to the operator thorough VR headset (bottom right).

4.1 Human-embodied Drone with Simple Task

Figure 4.2 demonstrates overall view of the human-embodied drone for package pick-and-place. The drone is designed with a hexacopter, two 3-DOF manipulators, haptic sensing, vision sensing, and voice communication with drone noise filter.

4.1.1 Aerial Manipulator Design

The goal of the human-embodied drone is to embody a person's body motions and senses. A Powerday S550 hexacopter, 920Kv motors, 945 propellers were chosen to create 3.6 kg payload capacity. The drone do not have to exactly mimic the human form. With payload limits, 3 degree-of-freedom (DOF) dual-arms and parallel jaw grippers that mount to the drone were designed; they provide suitable motion range

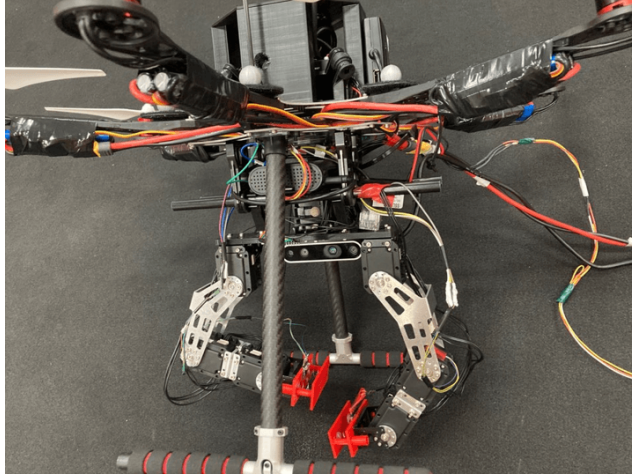


Figure 4.3: Close view of aerial manipulator's dual-arm and camera

for the operator to manipulate objects. An Intel RealSense D435i Camera is mounted on the bottom of the vehicle (see Figure 4.3). For immersion, the Microsoft HTC Vive was selected. The headset shows the operator a virtual representation of the vehicle's nearby environment. The hand controllers generates scalar scaled vibrations to provide haptic feedback (see Figure 4.4).

4.1.2 Human body-motions

To utilize human arm motions, a pair of robotic manipulators that were used in valve-turning [36] were advanced. An extra DOF was added and range sensors were embedded in the parallel jaw gripper. Each of the manipulators consists of three MX-28 Dynamixels, a steel elbow frame, and a joint to gesture human body-motions. Figure 4.4 shows the coordinate systems of the aerial manipulator and the operator with VR device. Table 4.1 describes the Denavit-Hartenberg parameters. Table 4.2

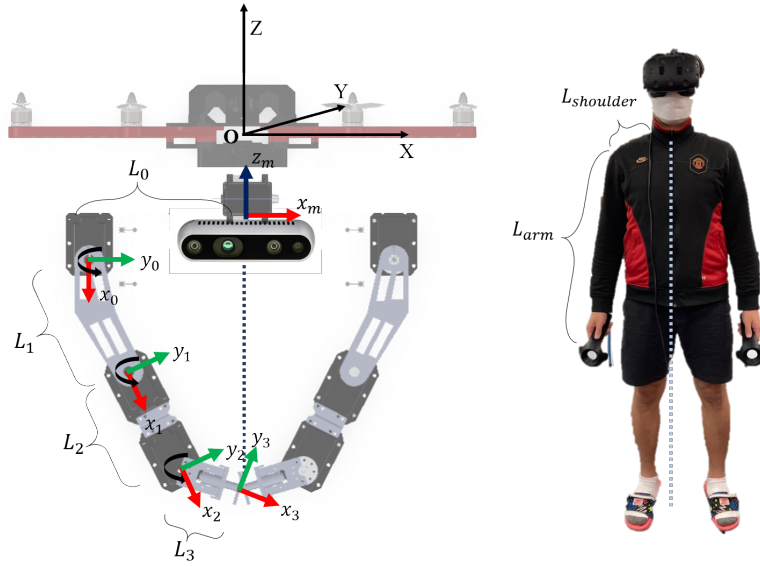


Figure 4.4: Kinematics relationship between the aerial manipulator and the operator with VR device (links expanded for clarity)

Table 4.1: Manipulator's Denavit-Hartenberg Parameters

Link(i)	θ_i (rad.)	α_i (rad.)	d_i (m)	a_i (m)
1	θ_1	0	0	L_1
2	θ_2	0	0	L_2
3	θ_3	0	0	L_3

shows manipulator and operator properties. First the homogeneous transforms are created following Equation 4.1.

$${}^{n-1}A_n = \begin{bmatrix} \cos\theta_n & -\sin\theta_n \cos\alpha_n & \sin\theta_n \cos\alpha_n & a_n \cos\theta_n \\ \sin\theta_n & \cos\theta_n \cos\alpha_n & -\cos\theta_n \sin\alpha_n & a_n \sin\theta_n \\ 0 & \sin\alpha_n & \cos\alpha_n & d_n \\ 0 & 0 & 0 & 1 \end{bmatrix} \quad (4.1)$$

Table 4.2: Aerial Manipulator and the Operator Physical Properties

Symbol	Value (m)
L_0	0.08 m
L_1	0.09 m
L_2	0.093 m
L_3	0.05 m
$L_{shoulder}$	0.28 m
L_{arm}	0.73 m

The sensors in the VR hand controller capture its position relative to the user's shoulder tip. These positions are then used to determine the manipulator's end-effector positions with the following:

$$\begin{bmatrix} x_e \\ y_e \end{bmatrix} = \begin{bmatrix} x_{controller} \frac{L_1+L_2}{L_{arm}} \\ y_{controller} \frac{L_0}{L_{shoulder}} \end{bmatrix} \quad (4.2)$$

The end-effector has a parallel jaw gripper. The gripper must be aligned with the global z -axis during manipulation to properly grasp objects. Thus, the desired position must be considered with the length of the gripper:

$$\begin{bmatrix} x_{desired} \\ y_{desired} \end{bmatrix} = \begin{bmatrix} x_e - L_3 \\ y_e \end{bmatrix} \quad (4.3)$$

The end-effector's forward kinematics are computed using

$$T = {}^0A_1{}^1A_2 \quad (4.4)$$

Finally, the inverse kinematics are computed using the Orocos Kinematics and Dynamics Library (KDL). The desired angles θ_1 and θ_2 are first calculated. θ_3 is then calculated using Equation 4.5:

$$\theta_3 = \frac{\pi}{2} - \theta_2 - \theta_1 - \frac{\pi}{6} \quad (4.5)$$

Human arm motions follow an elbow-down configuration. Negative θ_1 and θ_2 values are the opposite (i.e. elbow-up). Thus Equation 4.6 and Figure 4.5 is used to

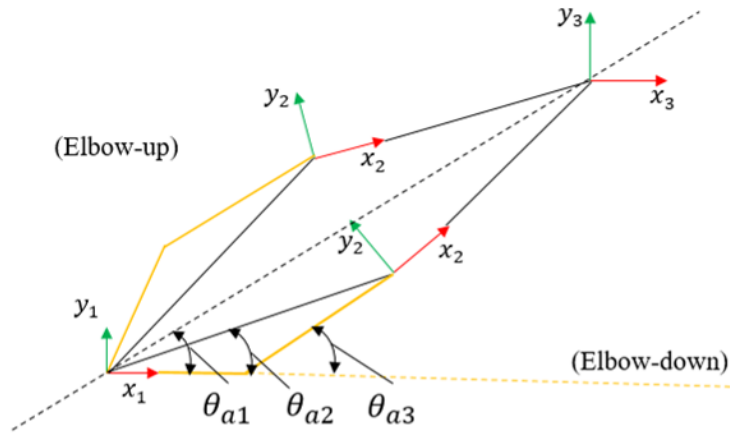


Figure 4.5: Elbow up and down configuration: yellow lines describes the steel elbow frame

configure the manipulator in the elbow-down configuration.

$$\begin{bmatrix} \theta_1^{new} \\ \theta_2^{new} \end{bmatrix} = \begin{bmatrix} 2(\theta_{a1} - \theta_1 - \theta_{a2}) + \theta_1 \\ -\theta_2 + 2\theta_{a3} - 2\theta_{a2} \end{bmatrix} \quad (4.6)$$

θ_{a1} is the angle between the manipulator's first joint origin and desired position. θ_{a2} is the angle between joint axis x_0 and link 1 which is 18.45° . θ_{a3} is the manipulator's steel elbow frame tilt angle which is 30° .

4.1.3 Haptics, Vision and Audio Feedback

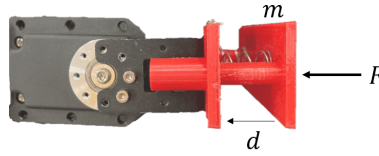


Figure 4.6: Sensorized end-effector for haptic feedback

Haptic Feedback: The sensorized parallel end-effectors are attached to each of the manipulator tips to provide haptic feedback to the operator (Figure 4.6). Each of the end-effector has a 3D printed frame, a time-of-flight VL6180x range sensor and two springs. The spring constant (0.5 N/mm), is found by the Dynamixel MX-28's stall torque which is 2.5 Nm [96]. When the end-effector pushes the object, the force is

generated and sensed. The amount of sensed force is calculated using:

$$F = m\ddot{d} + 2Kd \quad (4.7)$$

Where m , d and K are the end-effector's weight ($6g$), spring displacement, and spring constant, respectively. The VR controller vibrates accordingly to render the sensed force to the operator.

Vision Feedback: To provide 2D visual feedback, an Intel RealSense D435i camera was mounted on a MX-28 Dynamixel motor on the vehicle's belly (Figure 4.7). When the operator's head tilts as sensed by the VR headset, the camera angle changes. The camera is lifted backward to give the operator a wider field-of-view (FOV). The camera angle range was calibrated to range from 0 to 90 degrees (no to full tilting). These ranges map to the user's actual head angle range of -4 to 24 degrees (no to full tilting).

In addition, 3D vision feedback is also provided to present the real world in the virtual world (see Figure 4.9). This helps the operator to understand the nearby environment of the aerial manipulator. Recently, Simultaneous Localization and Mapping (SLAM) and PointCloud have been demonstrated as one of the solutions for 3D vision feedback. For drones to apply this solution, multiple cameras or sensors would have to be integrated to the aircraft, also this requires large computational loads. Furthermore, drones have payload limits. An approach used in the authors in the DARPA Robotics Challenge (DRC) [7] involved a LiDAR cart (see Figure 4.8). The

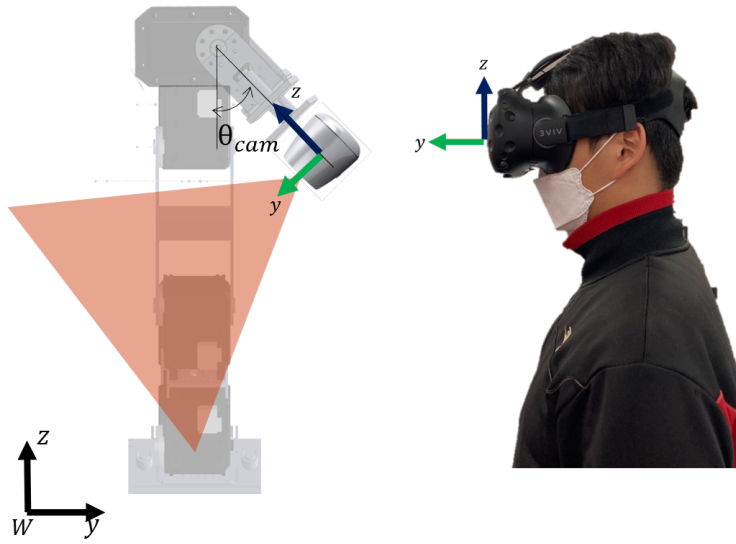


Figure 4.7: 2D vision feedback system: what the aerial manipulator see through the red triangle area is rendered to the operator. Red triangle area shows the camera's field-of-view (FOV)

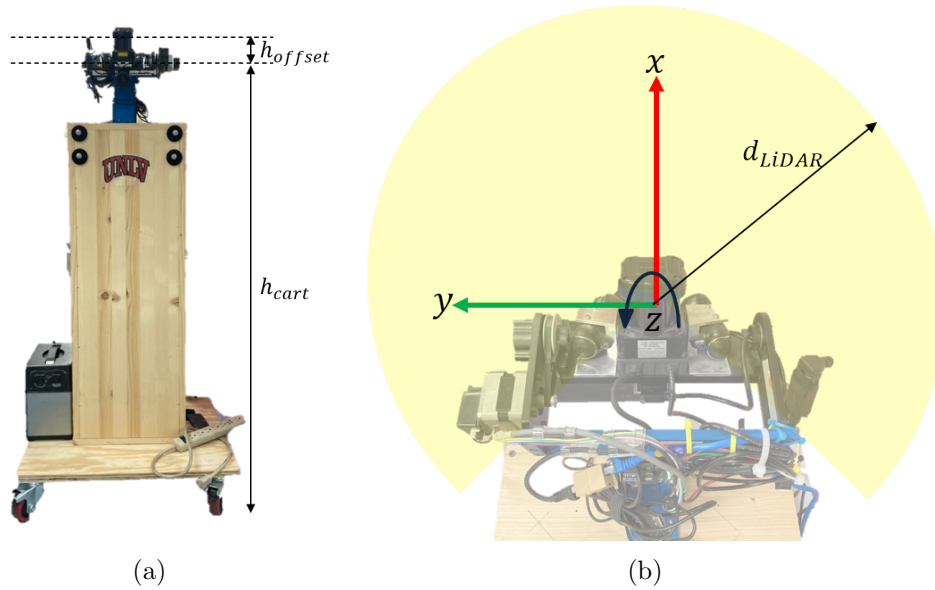
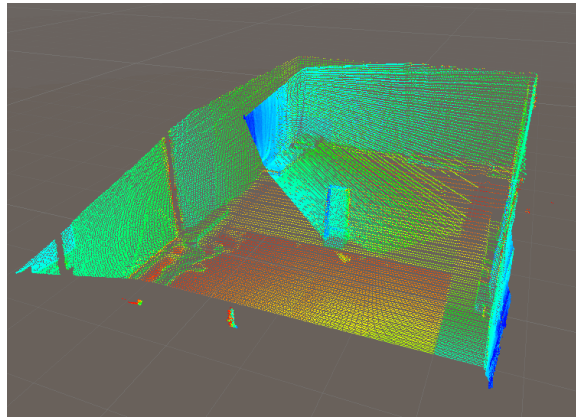


Figure 4.8: LiDAR cart overview: (a) LiDAR cart; (b) LiDAR tilts along with y-axis by a DC motor. Yellow area depicts LiDAR's scan range ($\pm 135^\circ$)



(a) The real world task space



(b) LiDAR map of the task space



(c) Colorized map of the task space

Figure 4.9: Pre-made 3D model of the work space

cart generates a PointCloud. This PointCloud is combined with a photo stitching software, Autodesk ReCap, to create a colored 3D map of the environment (see

Figure 4.9).

Audio Feedback: For the human-embodied drone to talk with people in the real-world, drone's propeller noise can easily drown out speech. Thus, a voice communication system using the open-source WebRTC (Web Real-Time Communication) package was selected. The designed system records prop noise and identifies its frequencies using a Short-Time Fourier Transforms (STFT) in MATLAB. A second order bandpass filter is then implemented in WebRTC to filter prop noise.

4.1.4 Virtual World Configuration

Unity is a software engine that is broadly used in VR/AR games. ROS and ROS-Sharp (ROS#) [83] enable robotic platforms to be integrated into Unity. The net effect is that one can create a virtual twin of the real-world aerial manipulator and nearby environment (see Figure 4.10).

First, the virtual aerial manipulator was modelled in SolidWorks. Then this model was exported in the Universal Robot Description Format (URDF). Finally the URDF was imported into Unity as a 3D model with ROS#.

Figure 4.10's inset shows the graphical user interface (GUI) in Unity. The GUI is designed with 5 menus. Each of the menus display a system status bar, command menu (arm, take-off, disarm, and landing), and launch buttons. The status bar provides condition status of the actual the drone in real-time. The command menu is displayed when the operator uses the VR controller to push the launch button. The operator uses the command menu to control the modes of the aerial manipulator in

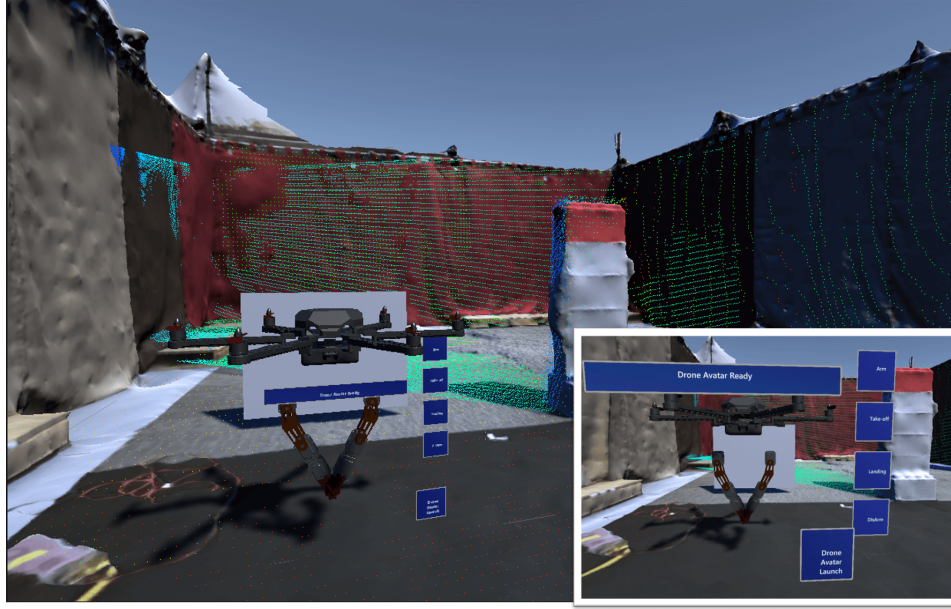
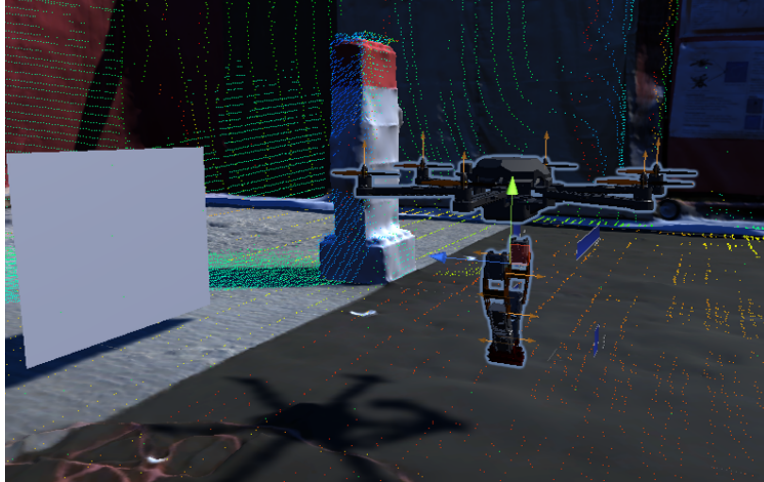


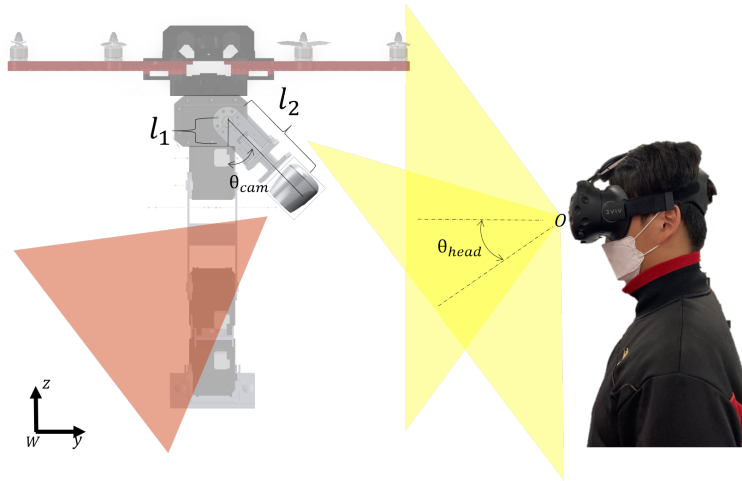
Figure 4.10: Final 3D virtual world in Unity engine. The inset shows the graphical user interface and aerial manipulator models

the real world.

A 3D model of the vehicle's work space is shown in Figure 4.10. Although this model is stationary, it still gives the operator useful situational awareness for the aerial manipulator. In addition to this model, real-time 2D camera feedback is combined together to help the user to effectively perform aerial manipulation. Figure 4.11 shows the configuration. A 2D plane object is created to render the 2D image. The size of the plane is 640 mm by 480 mm following the pixel size of the 2D image. The plane is placed 0.35 m front of the aerial manipulator to secure the aerial manipulator's work-space. (4.8) and (4.9) is used to keep the plane parallel to the VR headset face.



(a) 2D plane for 2D camera feedback and the aerial manipulator



(b) 2D camera feedback configuration description

Figure 4.11: 2D camera feedback configuration in the virtual world: field-of-views of the camera and the VR headset are shown in red and yellow, respectively

$$\begin{bmatrix} x_{plane} \\ y_{plane} \\ z_{plane} \end{bmatrix} = Rotz(\theta_{yaw}) Rotx(-\theta_{head}) \begin{bmatrix} x_{camera} \\ y_{camera} \\ z_{camera} \end{bmatrix} \quad (4.8)$$

$$\begin{bmatrix} x_{camera} \\ y_{camera} \\ z_{camera} \end{bmatrix} = \begin{bmatrix} x_m \\ y_m - l_2 + l_2 \cos(\theta_{cam}) + l_1 \sin(\theta_{cam}) - 0.35 \\ z_m + l_2 \sin(\theta_{cam}) + l_1 \cos(\theta_{cam}) \end{bmatrix} \quad (4.9)$$

Rot_x and Rot_z are the rotation matrix around x and z axes respectively. x_m , y_m , and z_m are the origin positions of manipulator (see Figure 4.4). l_1 is distance between the manipulator origin and motor's center of rotation, 1.4 cm. l_2 is distance between the motor's center of rotation and camera, 4.1 cm.

In addition, the aerial manipulation within the VR headset's field-of-view (FOV) and the aerial manipulator were found having 52 cm width. Thus, the vehicle is placed 40 cm in front of VR headset's point-of-view to display aerial manipulation clearly for the operator.

4.1.5 Flight Test

Flight trials were conducted in the motion capture area with the VR station (see Figure 4.12). The arena shows the aerial manipulator, a work stand and a 15 V 800 W power supply to provide longer flight times. The VR station has the HTC vive, desktop, and bluetooth earbuds, is located ten meters from the arena.

Figure 4.13 describes the control scheme for the aerial manipulator. The drone and manipulator are dynamically coupled but independently controlled with the VR controller and headset. In the manipulator controller, when a reference position is given by the VR controllers, the desired joint angles are calculated through inverse kinemat-

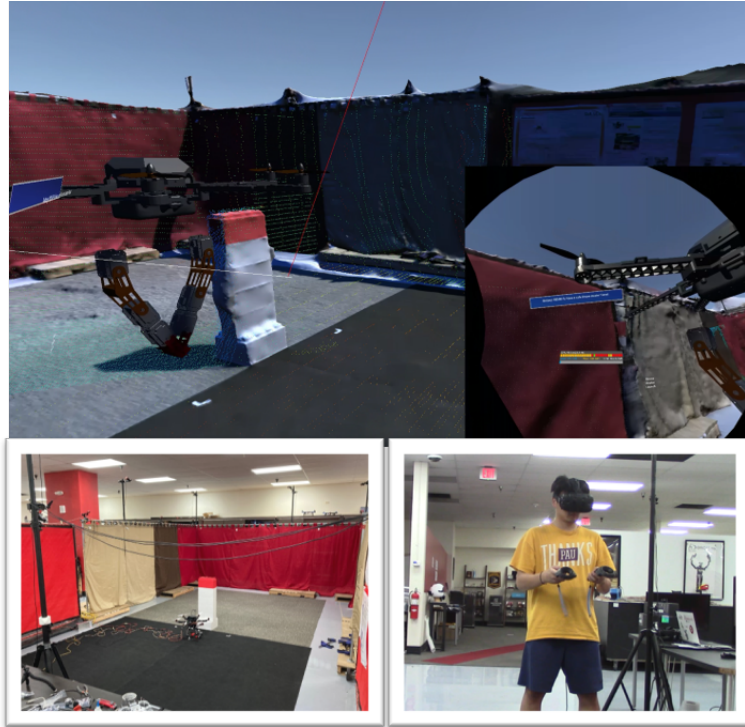


Figure 4.12: Flight trials: Unity scene (top), the motion capture area (bottom left), and VR station with the operator (bottom right)

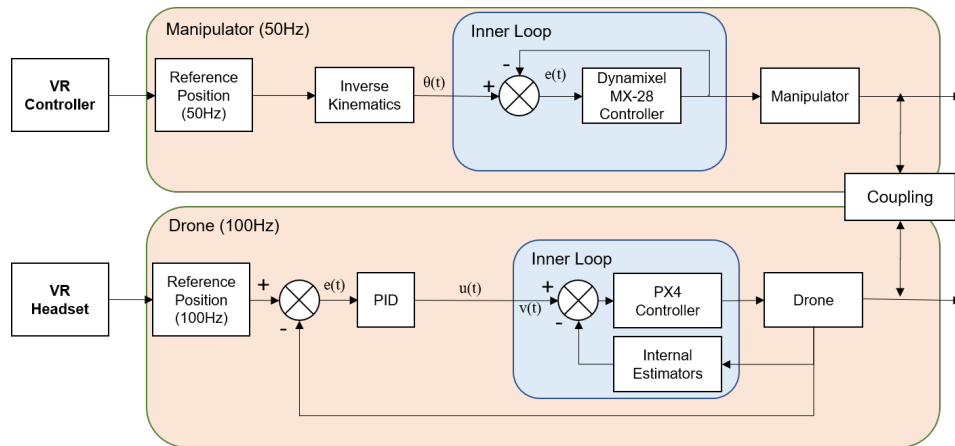
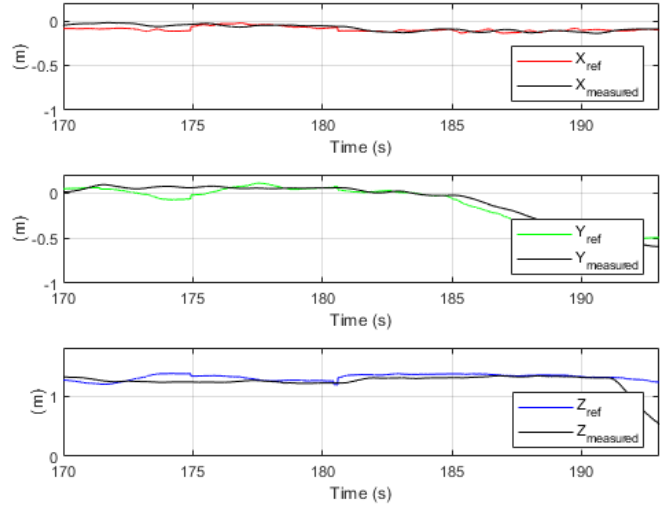
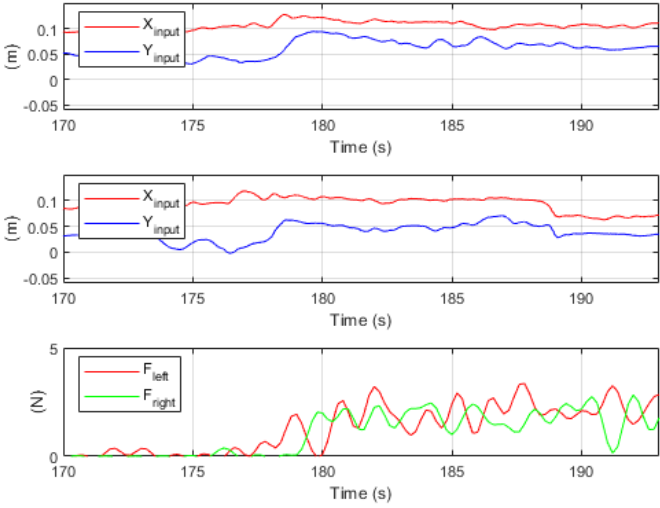


Figure 4.13: Aerial Manipulator Controller Scheme

ics. Then, the Dynamixel's low-level controller drives the joints to the desired angles. The drone controller has a proportional-integral-derivative (PID) compensator. This



(a) Flight trajectories: reference vs measured, X (Top) to Z (Bottom)



(b) End-effector trajectories of left arm (Top) and right arm (Center), and the reaction force(Bottom)

Figure 4.14: Flight trial results: Scenario 1

controller is detailed in Section 3.1. The computation for both controllers are done in Robot Operating Systems (ROS) on a Raspberry Pi 4 embedded computer.

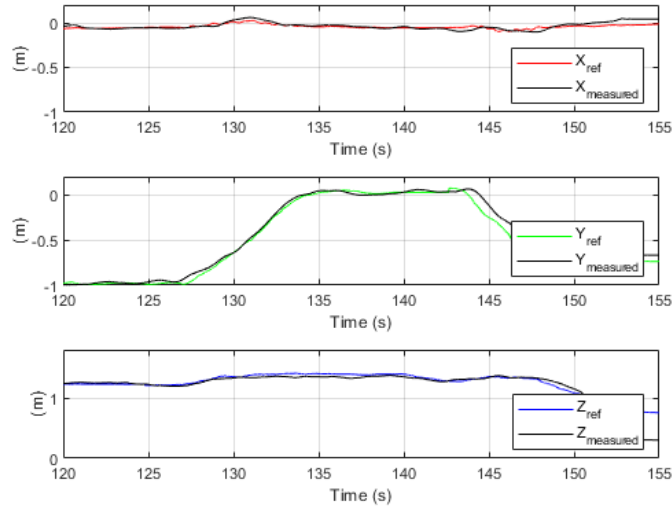
The main contribution of Section 4.1.1-4.1.4 is an integration of the immersive framework with the haptic-based human-in-the-loop aerial manipulation platform. This framework serves to make the operator feel as if they are where the drone is and experience a tele-presence through it. Flight scenarios were implemented to demonstrate them.

Scenario 1 – Package delivery: The operator uses visual perception, localization of objects, gestures, gaze, and haptics to move, grasp and manipulate a (8.5cm x 8.5cm x 4.5cm, 0.108kg) package. During the package pick-and-place, the reaction forces were sensed by the manipulator’s end-effector and rendered to the operator through the VR hand controllers. The scenario ran for 200 seconds. Figure 4.14 demonstrates the results. Figure 4.17 has an image sequence by the recorded video of this scenario.

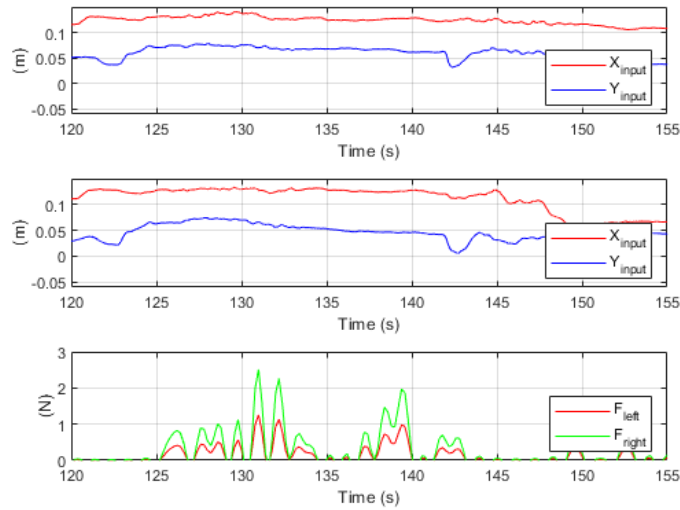
The increased reaction force and manipulator Y position shows the operator successfully grabs the package at time 175-180 seconds. One notices a increment at time 180 seconds. This is because the package was close to slip out of the end-effector due to prop downwash. Haptic feedback, however, sensed this and the operator performed power-grasp. One can see that the sensed reaction force fluctuates due to the range sensor’s small resolution and the vibration from drone flight.

Scenario 2 – Operator Interaction with Recipient: Human-embodied drone’s operator communicates with a recipient to accomplish package delivery. Such shared situational awareness demonstrates operator’s presence.

The WebRTC-based noise filter from Section 4.1.3 allows the operator to hear requests from a recipient standing around the drone. Here, the recipient communi-



(a) Flight trajectories: reference vs measured, X (Top) to Z (Bottom)



(b) End-effector trajectories of left arm (Top) and right arm (Center), and the reaction force(Bottom)

Figure 4.15: Flight trial results: Scenario 2

cates with the operator to place the package within the space. This scenario ran for 170 seconds. Figure 4.15 shows the results. Figure 4.16 has a spectrogram which

demonstrates successful performance of the noise filter. Figure 4.18 shows an image sequence by recorded video of this scenario.

The increased reaction forces and arm motions shows that the aerial manipulator received the package around 125 seconds. The changes on end-effector position and the reaction force measurements between 140 and 145 seconds show the package successfully delivered on the work stand. One can see that the amount of the reaction forces is smaller than the ones from the first scenario. This is because the recipient conversed with the operator; this shared situational awareness allowed the two people to cooperatively perform the task.

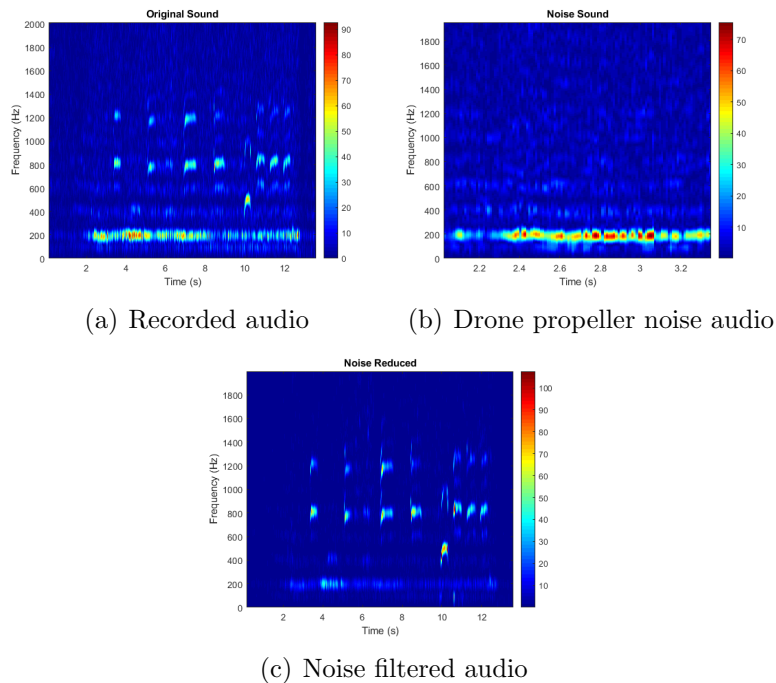
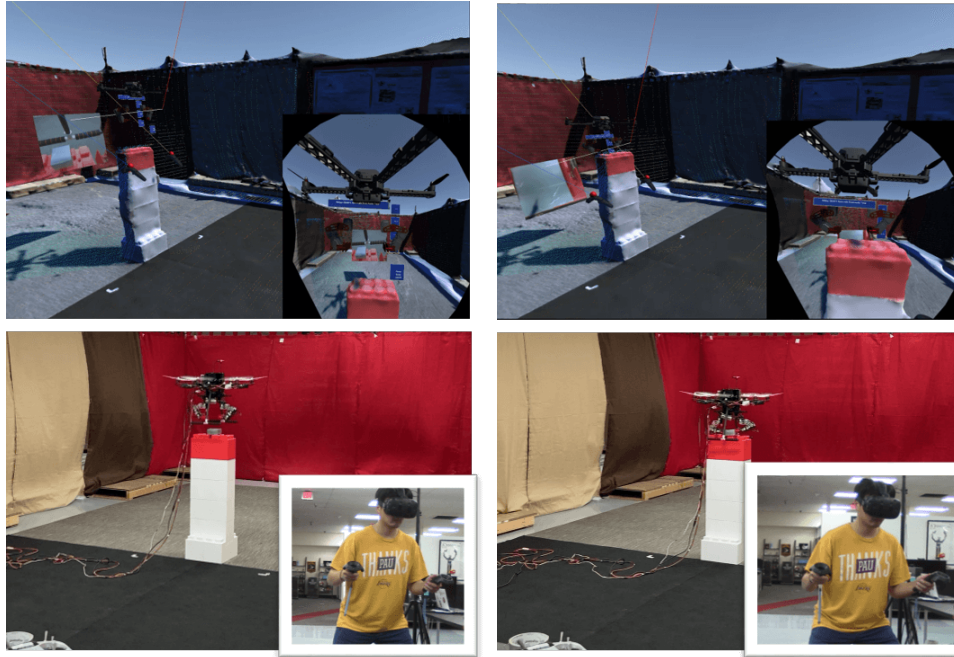
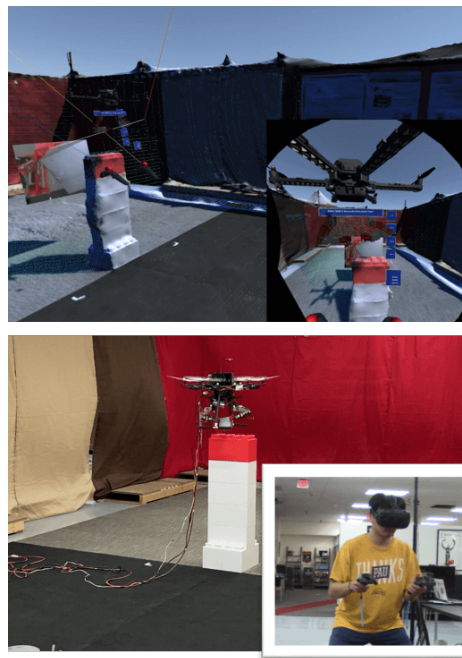


Figure 4.16: Noise filtering results



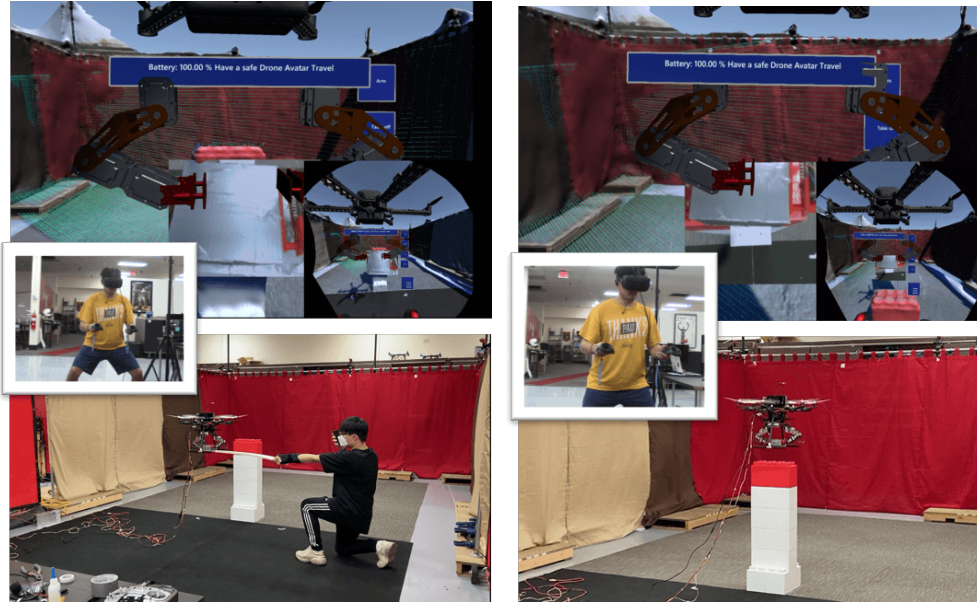
(a) Manipulation area arrival

(b) Attempt Grasping



(c) Hard grasping to secure the object from drone downwash effect

Figure 4.17: Flight trial summary: Scenario 1



(a) Received the package from the person; person also communicates about task performance

(b) Arrival at the work stand



(c) Place the package

Figure 4.18: Flight trial summary: Scenario 2

4.2 Human-embodied Drone with Complex Tasks

Through human-embodied drone interface, the operator could leverage their intelligence to handle the objects and socially interact with on-site workers to complete



Figure 4.19: Close-up of Aerial Manipulator: a single arm and gripper is attached under drone's belly; a camera is attached close to the landing gear

desired tasks. Thus, it is important to design a human-embodied interface for synthetic human intelligence. In the work in Section 4.1, the interface consists of seven factors: aerial manipulator design; human gesture mapping; haptics; synthetic vision; auditory feedback; mobility; and immersion. In this section, the factors applied to the previous interface are evolved except for the auditory feedback.

4.2.1 Aerial Manipulator Design

To design a suitable aerial manipulator for the interface, a Powerday S550 hexacopter was chosen to have 6.2 *kg* payload capacity with six 880 *kv* brushless motors and 11" carbon-fiber propellers. Given the payload limit and target horizontal tasks, a three degree-of-freedom (DOF) arms and a parallel jaw gripper are mounted to the drone; this allows the operator to manipulate objects with a suitable motion range. A 200-degrees Field-of-View (FOV), 8 Megapixels Fisheye Camera is mounted on the left side of the vehicle to provide visual feedback (see Figure 4.19).

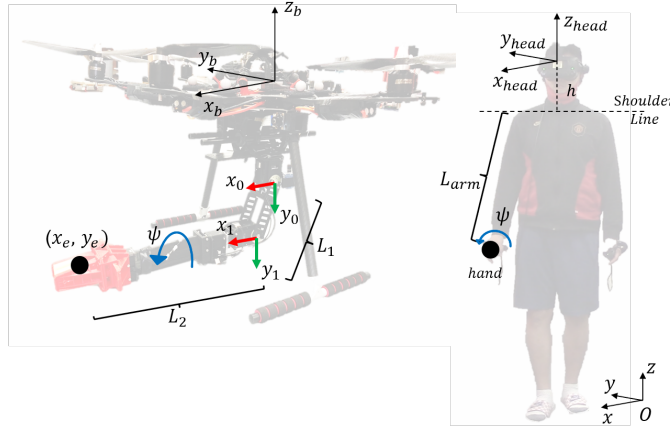


Figure 4.20: Kinematics relationship between the aerial manipulator and the operator with the VR device(links expanded for clarity)

4.2.2 Human body-motions

The human-embodied drone interface in the previous section, had a pair of aerial manipulators (dual-arm and gripper) for pick-and-place tasks. Dual-arm well gestured the operator's arm motions. In this paper, however, a 4-DOF single-arm and gripper are attached to the drone due to payload limits and the desired motion range. The manipulator has two MX-64 Dynamixels, two XM430 Dynamixels, a steel frame, a 3D printed gripper to mimic the operator's right arm and hand motions (pinch and rotate). Figure 4.20 shows the coordinate systems of the aerial manipulator and the operator with the VR device. The headset and controller independently control the positions of the drone and manipulator.

Table 4.3 describes the Denavit-Hartenberg parameters. Table 4.4 shows the properties of aerial manipulator and the operator. Then, the homogeneous transforms are derived using Equation 4.1.

Table 4.3: Aerial Manipulator Denavit-Hartenberg Parameters

Link(i)	θ_i (rad.)	α_i (rad.)	d_i (m)	a_i (m)
1	θ_1	0	0	L_1
2	θ_2	0	0	L_2

Table 4.4: Aerial Manipulator and the Operator Physical Properties

Symbol	Value (m)
L_1	0.11 m
L_2	0.33 m
L_{arm}	0.73 m
h	0.22 m

The sensors in the VR system calculate VR controller's relative position to the user's VR headset position. Then, these positions are utilized to find the desired positions of manipulator's end-effector with the following:

$$\begin{bmatrix} x_e \\ y_e \end{bmatrix} = \begin{bmatrix} (x_{hand} - x_{head}) \frac{L_1 + L_2}{L_{arm}} \\ (z_{hand} - z_{head} + h) \frac{L_1 + L_2}{L_{arm}} \end{bmatrix} \quad (4.10)$$

where x_e and y_e are the end-effector's position relative to the manipulator's XY-plane origin. x_{hand} , y_{hand} , x_{head} and y_{head} are global positions of the right VR controller and headset. h is the distance between VR headset and the operator's horizontal shoulder line. The right VR controller's roll angle ψ rotates the gripper.

To find the desired angles θ_1 and θ_2 , the forward kinematics are derived by the following:

$${}^0T_2 = {}^0A_1 {}^1A_2 \quad (4.11)$$

Then, the inverse kinematics are calculated to find suitable joint angles for the manipulator to reach to the desired position. The Jacobian matrix is derived using Equation 4.11.

$$\dot{x} = J(\theta)\dot{\theta} \quad (4.12)$$

where \dot{x} is the end-effector velocities, $J(\theta)$ is the Jacobian matrix, $\dot{\theta}$ is the joint's angular velocities. With the desired end-effector positions from 4.10, the suitable joint angles are determined using the Levenberg-Marquardt method [84].

The drone's gripper has a parallel mechanism. The gripper has to be parallel to the ground to properly manipulate objects horizontally during the flight.

4.2.3 Haptics and Synthetic Vision

Haptics: To provide haptic feedback to the operator, the torque sensors on the arm's dynamixels are calibrated to measure the applied force on each joint. Dynamixels usually capture the force while the attached mass is rotating or being pushed. Thus, it is hard to capture the reaction force from the sensors when the arm physically interacts with near environments. To correctly measure these forces during the manipulation, the dynamixels are configured to sense the force when the arm is

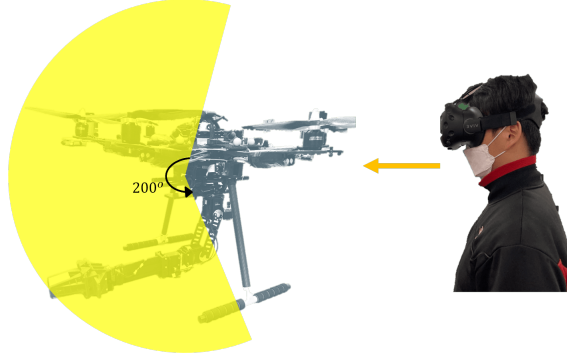


Figure 4.21: Synthetic vision by fisheye camera, and the operator with VR Headset. Yellow area shows the camera's field-of-view (FOV)

horizontally full-stretched by the following:

$$F_i^{reaction} = F_i^{measured} - F_i^{normal} \quad (4.13)$$

where $i = 1, 2, 3, 4$, is the number of the motor - joint1, joint2, joint3, and gripper, respectively. $F_i^{reaction}$, $F_i^{measured}$ are reaction force and sensed force. F_i^{normal} is the pre-captured force when the arm is horizontally full-stretched without physical interaction or payload on the gripper. The VR controllers emit scalar-scaled vibrations to provide haptic feedback. One can not perform haptic assessment if the multiple reaction forces are rendered together in a single source. Thus, the source is splited to render in two VR controllers. When reaction force is captured in joints 1 and 2, the left VR controller renders the amount of reaction force to the operator by vibrations. When reaction forces are captured in joint three and gripper, the right VR controller emits vibrations.(see Figure 4.20).

Synthetic Vision: To provide synthetic vision, a 200-degrees Field-of-View (FOV),

8 Megapixels Fisheye Camera is mounted on the left side of the vehicle. The wide range of camera sensor provides more situational awareness than the author's previous design with a pre-captured 3D model and real-time 2D feedback. In addition, the camera angle does not have to change by the VR headset angle. The fisheye camera renders raw circular image data. To properly provide the visual feedback, the image is calibrated and stitched in a sphere using Equation 4.14 and 4.15 (see Figure 4.22).

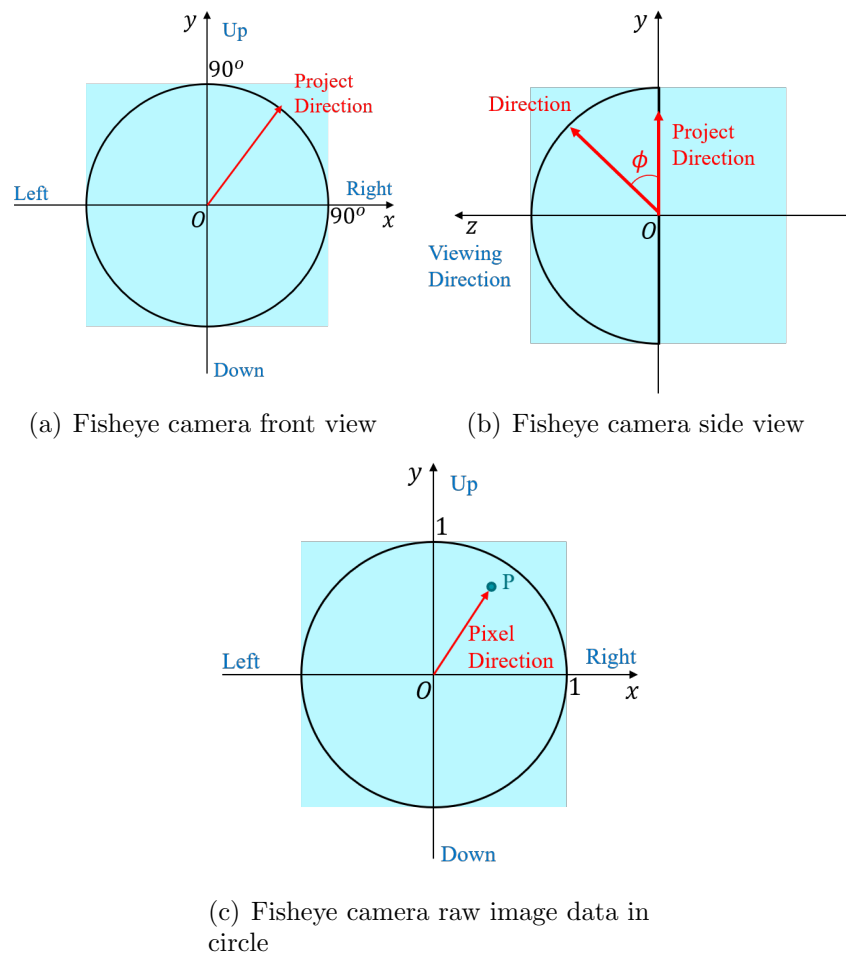


Figure 4.22: Fisheye camera image stitching into 3D sphere

$$\begin{bmatrix} \theta_{proj} \\ \phi_{proj} \\ r \end{bmatrix} = \begin{bmatrix} atan2(z_{sphere}, x_{sphere}) \\ atan2(\sqrt{x_{sphere}^2 + z_{sphere}^2}, y_{sphere}) \\ \phi_{proj}/FOV \end{bmatrix} \quad (4.14)$$

$$\begin{bmatrix} x_{pixel} \\ y_{pixel} \end{bmatrix} = \begin{bmatrix} 0.5 - r * \sin(\theta_{proj}) \\ 0.5 + r * \cos(\theta_{proj}) \end{bmatrix} \quad (4.15)$$

where $(x_{sphere}, y_{sphere}, z_{sphere})$ is the position to render raw image in the sphere. x_{pixel} and y_{pixel} shows the location of the pixel in unit circle of the raw fisheye image. the to be rendered as 3D sphere for the operator through VR headset

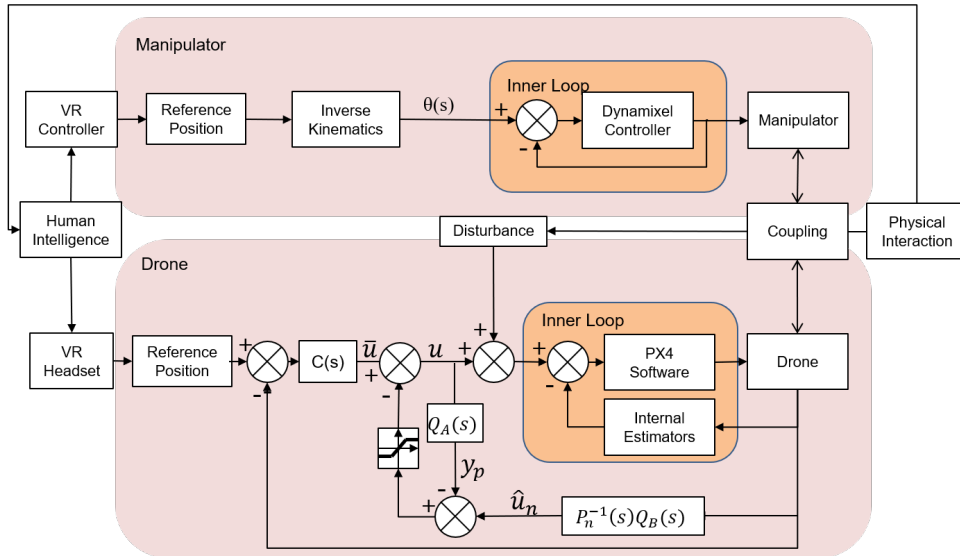


Figure 4.23: Human-embodied drone controller scheme

4.2.4 Mobility

Figure 4.23 depicts the control structure in the human-embodied drone interface. The drone and manipulator are dynamically coupled. While the aerial manipulator is physically interacting with objects, the operator leverages their intelligence to perform task assessment, then controls the aerial manipulator with the VR headset and controllers. The decentralized approach is implemented to stabilize the vehicle. This approach treats the vehicle and the manipulator as two separate independent systems. Moreover, the drone's coupling effects with the manipulator and uncertainty from the drone's physical interaction with the environment are considered as external disturbance [69].

Recently, Disturbance Observer(DOB) based position controller has been applied in aerial manipulation. The rationale is that the DOB assists the transient performance recovery of the aerial manipulator in tasks. The controller performance has been validated in [88] where an unmanned aerial manipulator(UAM) pushes a movable structure like a hinged-door. Thus, the aerial manipulator equips a DOB proportional-integral-derivative (PID) position, controller. The DOB tutorial in [89] provides a simple and effective design of DOB based controller.

In the manipulator, when a reference position is given by the VR controllers, the desired joint angles are first calculated through inverse kinematics. Then the Dynamixel's low-level controller drives the joints to the desired angles. The computation for both controllers is done in MAVROS on a NVIDIA Jetson Xavier NX computer.

4.2.5 Immersion

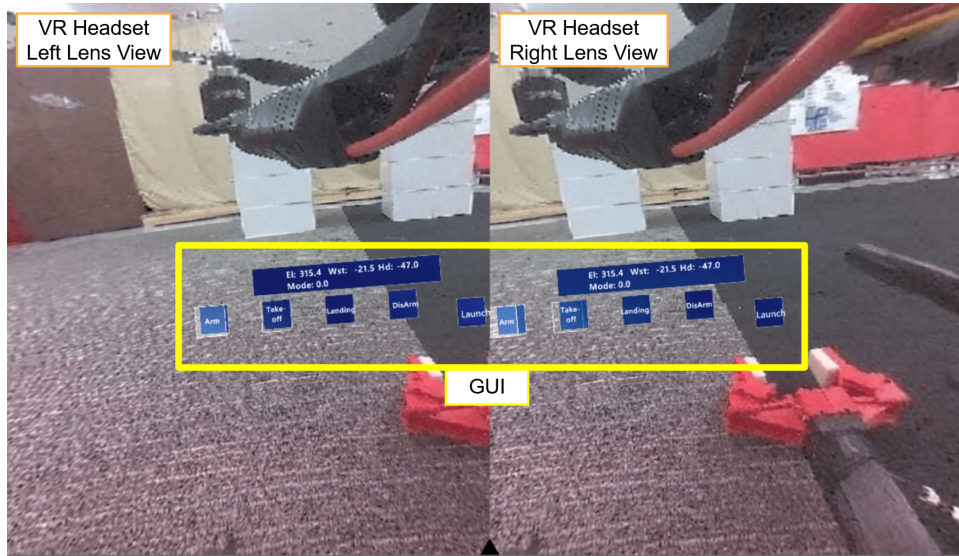


Figure 4.24: Overall virtual world scene in Unity engine

The Valve Index VR Full Kit was selected for immersion. Microsoft Mixed Reality Toolkit (MRTK) [99], and ROS# [83] are computed together to integrate robotic platforms into a VR/AR gaming software engine, Unity. The Unity allows one to create a virtual twin of the real-world aerial manipulator and nearby environment. The virtual scene in the paper has simpler models - a sphere model and the graphical user interface (GUI) - than the one from the author's previous work (see Figure 4.24).

3D sphere model has a shader to display visual data on its inner surface. The shader is coded with Equation 4.14 and 4.15 to stitch raw images from the fisheye camera. The GUI has five menus. Each of the menus displays a system status bar. The status bar provides real-time information of applied currents on the manipulator's

dynamixels. The operator controls the command menu to deploy the onsite aerial manipulator.

4.2.6 Flight Trials

Flight trials were conducted in the motion capture arena with the VR station (see Figure 4.25). The arena has the aerial manipulator, a task stand with drywall, a pipe hole, and a door lock. An 18V, 1080W power supply to provide sufficient flight times. 25 meters from the arena, there is the VR station which has the Valve Index VR full kit, a gaming desktop.

The net effect from the general objectives is the embodiment of the operator

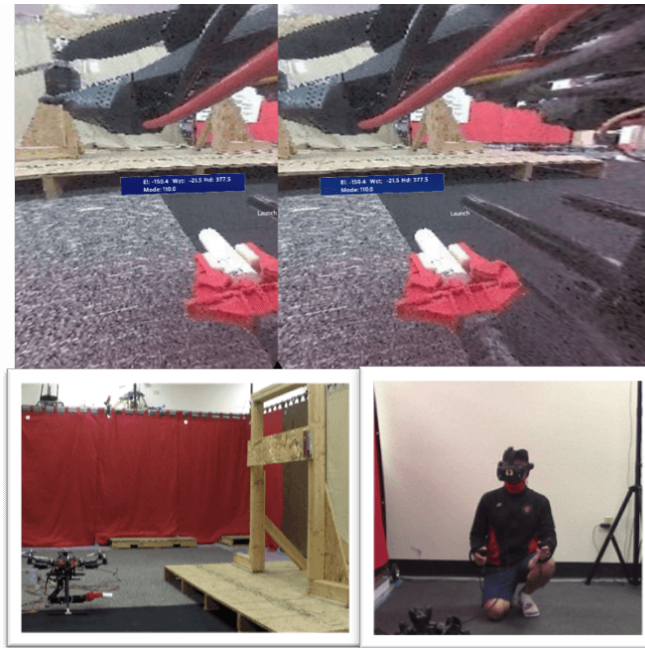


Figure 4.25: Flight Environment: Unity view (top), the motion capture arena (bottom left), and VR station with the operator (bottom right)

in an aerial manipulator platform. The embodiment enables the operator to have a visual perception, localization of objects, gestures, gaze, and haptics to handle objects dexterously. Thus, one could augment their intelligence to perform aerial manipulation beyond line-of-sight. Several aerial manipulation tasks were conducted to demonstrate such a platform's efficacy.

Task 1 – Drilling: The scenario ran for 120 seconds. The operator grabs a hand rotary tool through human-embodied drone to horizontally drill into drywall. During the drill tasks, the reaction forces were captured by the manipulator's torque sensors and provided to the operator through the VR hand controllers. Figure 4.26(a) demonstrates the results. Figure 4.27 is an image sequence by the recorded video of this task.

The changes in x position of the aerial manipulator show the operator successfully performed the drill tasks at time 60-70 seconds and 75-85 seconds.

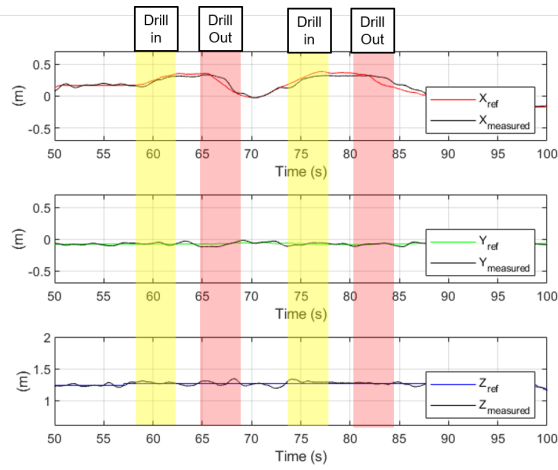
Task 2 – Peg-in-hole: This task ran for 160 seconds. The operator plugs a 1" radius PVC pipe into a 1-1/4" PVC pipe's hole through the human-embodied drone. The scenario ran for 160 seconds. Figure 4.26(b) demonstrates the results. Figure 4.28 is an image sequence by the recorded video of this task.

The operator successfully performed the peg-in-hole task Between time 105-140 seconds. The increased x position errors show that the aerial manipulator began plugging the pipe into the hole.

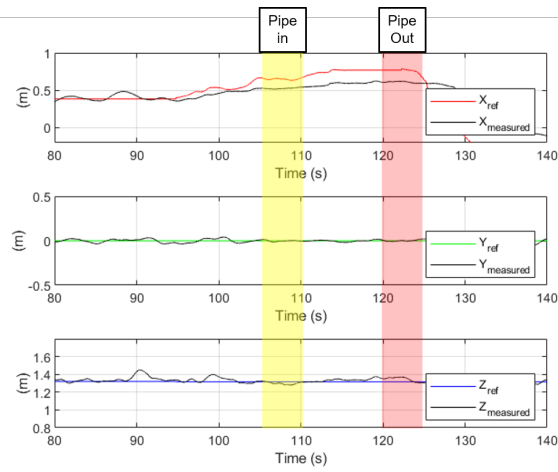
Task 3 – Key Manipulation: The task ran for 215 seconds, longer than the drill and peg-in-hole tasks. The operator manipulates a (2.2cm x 7.5cm) key to lock/unlock

the home door. Figure 4.26(c) describes the results. Figure 4.29 showcases an image sequence from recorded video of this scenario.

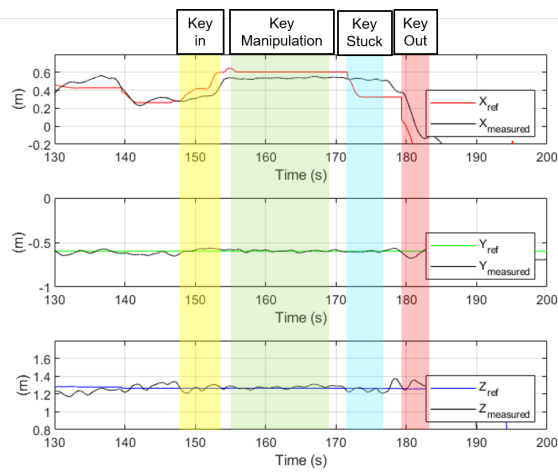
The operator successfully put the key in the home door at 150 seconds. Then, the door is locked/unlocked between 155-170 seconds. One can observe that the key is stuck for about 8 seconds. Finally, the key is pulled out at 180 seconds.



(a) *Task 1*



(b) *Task 2*



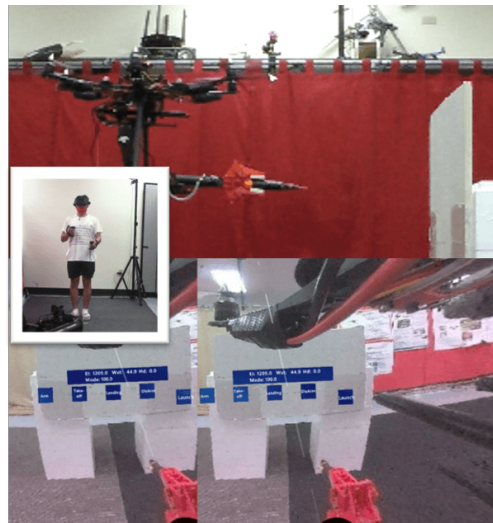
(c) *Task 3*

Figure 4.26: Trajectories of the reference and measured position, from *All Tasks*: X (Top) to Z (Bottom)



(a) Approach

(b) Drilling on the drywall



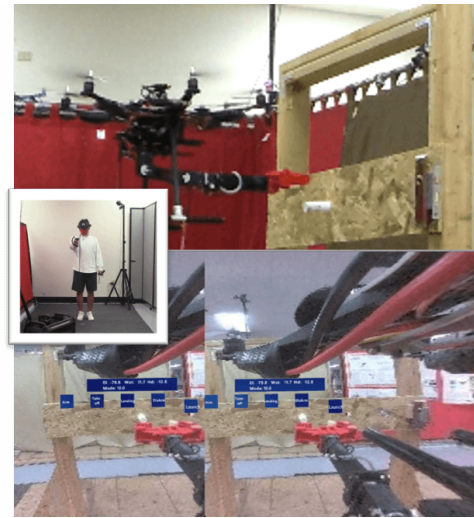
(c) Pull off the drill

Figure 4.27: Flight trial summary of *Task 1*



(a) Approach to the target hole

(b) Peg-in-hole



(c) Release the pipe

Figure 4.28: Flight trial summary of *Task 2*



(a) Approaching to the door-lock

(b) Lock the key; yellow circle shows the steel bar is pulled out



(c) Unlock the key

Figure 4.29: Flight trial summary of *Task 3*

CHAPTER 5 CONCLUSION

5.1 Summary of Contributions

This dissertation presents contributions to state-of-art aerial manipulation. Despite the number of contributions in the past decade, one can hardly see adoptions or implementations of aerial manipulation in practice. The challenge stems from autonomy. The autonomous aerial manipulation has been accomplished in simple cases where the target object information was a known *priori*, and (or) the object geometries were simplified to relax the constraints. Thus, this dissertation raises questions on the designs for human-in-the-loop aerial manipulation. The motivation for this dissertation is that such a design could augment the abilities of workers in dangerous tasks to complete the tasks using mobile manipulating drones.

Chapter 3 presents preliminary works that include the following: models, designs, and controls of aerial manipulation with parallel mechanisms; a gantry-based testing-and-evaluation platform for haptic-based human-in-the-loop aerial manipulation and haptic-based human-in-the-loop aerial drilling.

Finally, Chapter 4 integrates immersive devices with the existing haptic-based human-in-the-loop platform. The main contribution of this integration is to form a human-embodied drone interface for dexterous aerial manipulation. Section 4.1 presents the first human-embodied drone interface for package delivery with and

without a recipient. The operator successfully accomplished the given tasks in these scenarios with no a priori information about the package or its nearby environment. Haptic feedback allowed the operator to take care of the package which was about to slip from the manipulator’s end-effector. In the second scenario, the conversation between the operator and recipient yielded success through shared situational awareness. Section 4.2 evolves the first interface. A 200 FOV Fisheye camera improved situational awareness. A 4-DOF arm and a parallel jaw gripper allowed the operator to pinch and grasp the objects. This increased the dexterity of the interface. Disturbance Observer-based (DOB) controller improves the aerial manipulator’s stability in flight for horizontal tasks of drilling, peg-in-hole, and lock-unlock key. The flight trials successfully demonstrated the interface’s efficacy.

5.2 Future Work

To the best of our knowledge, the development of the human-embodied interface for aerial manipulation is novel. We believe this interface has potential for practical implementation. The embodied operator in aerial manipulator can leverage their *intelligence* through the immersive framework to physically interact with objects and socially interact with on-site workers during the dexterous tasks in drilling, peg-in-hole, and key manipulation.

During the flight trials of the human-embodied drone, reaction forces are sensed when the robotic manipulators interact with physical objects. The current controller does not consider mechanical impedance from the manipulator’s physical interaction

with the object. This can cause mechanical damage by large reaction forces. Also, this can prevent the operator from performing accurate haptic assessments during the task. Therefore, future work will include studies in a force tracking impedance controller. In addition, the newest AR/VR devices have headset cameras that recognize hand gestures. These devices would give freedom to design suitable haptic devices for the operator. To provide haptic feedback to the whole body of the operator, a cable-driven parallel robot (CDPR) in [100] will be explored.

With progress in future work, this dissertation envisions that the human-embodied drone interface will generate opportunities for injured or elderly workers to complete tasks. The interface could also be a suitable test-and-evaluation platform to practice human-in-the-loop aerial manipulation in real and virtual worlds. The successful practice would yield a vital dataset to bridge the gap for autonomous aerial manipulation from implementation to adoption.

BIBLIOGRAPHY

- [1] R. O. Ambrose et al., "Mobile manipulation using NASA's Robonaut," *IEEE International Conference on Robotics and Automation (ICRA)*, pp. 2104-2109, 2004.
- [2] M. Seelinger, J. -. Yoder, E. T. Baumgartner and S. B. Skaar, "High-precision visual control of mobile manipulators," *IEEE Transactions on Robotics and Automation*, 18(6), pp. 957-965, 2002.
- [3] Brantner G., Khatib O. "Controlling Ocean One," *In: Hutter M., Siegwart R. (eds) Field and Service Robotics. Springer Proceedings in Advanced Robotics*, vol 5. Springer, Cham, 2018
- [4] K. Hirai, M. Hirose, Y. Haikawa and T. Takenaka, "The development of Honda humanoid robot," *IEEE International Conference on Robotics and Automation*, pp. 1321-1326 vol.2, 1998.
- [5] Y. Sakagami, R. Watanabe, C. Aoyama, S. Matsunaga, N. Higaki and K. Fujimura, "The intelligent ASIMO: system overview and integration," *IEEE/RSJ International Conference on Intelligent Robots and Systems*, pp. 2478-2483 vol.3, 2002.
- [6] T. Jung, J. Lim, H. Bae, K. K. Lee, H. Joe and J. Oh, "Development of the Humanoid Disaster Response Platform DRC-HUBO+," *IEEE Transactions on Robotics*, 34(1), pp. 1-17, 2018.
- [7] P. Y. Oh, K. Sohn, G. Jang, Y. Jun and B.K. Cho, "Technical Overview of Team DRC-Hubo@ UNLV's Approach to the 2015 DARPA Robotics Challenge Finals", *Journal of Field Robotics*, 34(5), pp. 874-896, 2017.
- [8] Boston Dynamics ATLAS - the world's most dynamic humanoid robot[Online], Available: <https://www.bostondynamics.com/atlas>
- [9] J. Carius, M. Wermelinger, B. Rajasekaran, K. Holtmann, and M. Hutter, "Deployment of an autonomous mobile manipulator at MBZIRC", *Journal of Field Robotics*, 35(8), pp.1342-1357.
- [10] N. Castaman , E. Tosello , M. Antonello , N. Bagarello, S. Gandin , M. Carraro , M. Munaro , R. Bortoletto , S. Ghidoni, E. Menegatti, and E. Pagello, "RUR53: an unmanned ground vehicle for navigation, recognition, and manipulation," *Advanced Robotics*, 35(1), pp. 1-18, 2021.

- [11] Q. Lindsey, D. Mellinger, and V. Kumar, "Construction of cubic structures with quadrotor teams," *Proceedings of Robotics: Science and Systems (RSS)*, Los Angeles, CA, USA, 2011
- [12] J. Thomas, J. Polin, K. Sreenath, V. Kumar, "AVIAN-INSPIRED GRASPING FOR QUADROTOR MICRO UAVS," *ASME International Design Engineering Technical Conferences and Computers and Information in Engineering Conference*, 2013
- [13] J. Munoz-Morera, I. Maza, C. J. Fernandez-Aguera, F. Caballero and A. Ollero, "Assembly planning for the construction of structures with multiple UAS equipped with robotic arms," *International Conference on Unmanned Aircraft Systems (ICUAS)*, pp. 1049-1058, 2015.
- [14] D. Mellinger, Q. Lindsey, M. Shomin and V. Kumar, "Design, modeling, estimation and control for aerial grasping and manipulation," *IEEE/RSJ International Conference on Intelligent Robots and Systems (IROS)*, pp. 2668-2673, 2011.
- [15] J. Choi, D. Kim, "A New UAV-based Module Lifting and Transporting Method: Advantages and Challenges," *International Symposium on Automation and Robotics in Construction (ISARC)*, vol.36, pp. 645-650, 2019.
- [16] M. Orsag, C. Korpela, and P.Y.Oh, "Modeling and Control of MM-UAV: Mobile Manipulating Unmanned Aerial Vehicle," *Journal of Intelligent and Robotic Systems*, vol. 69, pp. 227-240, 2013.
- [17] T. W. Danko and P. Y. Oh, "Toward coordinated manipulator-host visual servoing for mobile manipulating UAVs," *IEEE International Conference on Technologies for Practical Robot Applications (TePRA)*, pp. 1-6, 2014.
- [18] P. Ramon Soria, B. C. Arrue and A. Ollero, "A 3D-Printable Docking System for Aerial Robots: Controlling Aerial Robotic Manipulators in Outdoor Industrial Applications," *IEEE Robotics & Automation Magazine*, 26(1), pp. 44-53, 2019.
- [19] M. I. Sánchez, J. Á. Acosta and A. Ollero, "Integral action in first-order Closed-Loop Inverse Kinematics. Application to aerial manipulators," *IEEE International Conference on Robotics and Automation (ICRA)*, pp. 5297-5302, 2015.
- [20] G. Garimella and M. Kobilarov, "Towards model-predictive control for aerial pick-and-place," *2015 IEEE International Conference on Robotics and Automation (ICRA)*, pp. 4692-4697, 2015.
- [21] G. Heredia et al., "Control of a multicopter outdoor aerial manipulator," *IEEE/RSJ International Conference on Intelligent Robots and Systems (IROS)*, pp. 3417-3422, 2014.

- [22] A. Y. Mersha, S. Stramigioli and R. Carloni, "Exploiting the dynamics of a robotic manipulator for control of UAVs," *IEEE International Conference on Robotics and Automation (ICRA)*, pp. 1741-1746, 2014.
- [23] B. Yang, Y. He, J. Han and G. Liu, "Separated adaptive control scheme of a rotor-flying manipulator," *IEEE 14th International Workshop on Advanced Motion Control (AMC)*, pp. 63-70, 2016.
- [24] S. Kim, S. Choi and H. J. Kim, "Aerial manipulation using a quadrotor with a two DOF robotic arm," *IEEE/RSJ International Conference on Intelligent Robots and Systems (IROS)*, pp. 4990-4995, 2013.
- [25] V. Lippiello and F. Ruggiero, "Exploiting redundancy in Cartesian impedance control of UAVs equipped with a robotic arm," *IEEE/RSJ International Conference on Intelligent Robots and Systems (IROS)*, pp. 3768-3773, 2012.
- [26] M. Orsag, C. Korpela, S. Bogdan, P. Y. Oh, "Hybrid Adaptive Control for Aerial Manipulation," *Journal of Intelligent and Robotic Systems*, vol 73, pp. 693-707, 2014
- [27] E. Cataldi et al., "Impedance Control of an aerial-manipulator: Preliminary results," *IEEE/RSJ International Conference on Intelligent Robots and Systems (IROS)*, pp. 3848-3853, 2016.
- [28] A. Suarez, G. Heredia and A. Ollero, "Physical-Virtual Impedance Control in Ultralightweight and Compliant Dual-Arm Aerial Manipulators," *IEEE Robotics and Automation Letters*, 3(3), pp. 2553-2560, 2018.
- [29] H. Tsukagoshi, M. Watanabe, T. Hamada, D. Ashlih and R. Iizuka, "Aerial manipulator with perching and door-opening capability," *IEEE International Conference on Robotics and Automation (ICRA)*, pp. 4663-4668, 2015.
- [30] T. Bartelds, A. Capra, S. Hamaza, S. Stramigioli and M. Fumagalli, "Compliant Aerial Manipulators: Toward a New Generation of Aerial Robotic Workers," *IEEE Robotics and Automation Letters*, 1(1), pp. 477-483, 2016.
- [31] A. Suarez, G. Heredia and A. Ollero, "Lightweight compliant arm with compliant finger for aerial manipulation and inspection," *IEEE/RSJ International Conference on Intelligent Robots and Systems (IROS)*, pp. 4449-4454, 2016.
- [32] M. Fumagalli et al., "Developing an Aerial Manipulator Prototype: Physical Interaction with the Environment," *IEEE Robotics & Automation Magazine*, 21(3), pp. 41-50, 2014.
- [33] Pruano F, Ollero A, Cano R, Prez C, Heredia G, "Mechanical design of a 6-DOF aerial manipulator for assembling bar structures using UAVs," *In Proceedings of the 2nd IFAC workshop on research, education and development of unmanned aerial systems (RED UAS)*, 2013

- [34] S. Kim, Hoseong Seo and H. J. Kim, "Operating an unknown drawer using an aerial manipulator," *IEEE International Conference on Robotics and Automation (ICRA)*, pp. 5503-5508, 2015.
- [35] M. Perez-Jimenez, M. A. Montes-Grova, P. Ramon-Soria, B. C. Arrue and A. Ollero, "POSITRON: lightweight active positioning compliant joints robotic arm in power lines inspection," *International Conference on Unmanned Aircraft Systems (ICUAS)*, pp. 729-736, 2020.
- [36] M. Orsag, C. Korpela, S. Bogdan and P. Oh, "Valve turning using a dual-arm aerial manipulator," *International Conference on Unmanned Aircraft Systems (ICUAS)*, pp. 836-841, 2014.
- [37] M. Orsag, C. Korpela, S. Bogdan and P. Oh, "Dexterous Aerial Robots — Mobile Manipulation Using Unmanned Aerial Systems," *IEEE Transactions on Robotics*, 33(6), pp. 1453-1466, 2017.
- [38] D. Lee, H. Seo, D. Kim and H. J. Kim, "Aerial Manipulation using Model Predictive Control for Opening a Hinged Door," *IEEE International Conference on Robotics and Automation (ICRA)*, pp. 1237-1242, 2020.
- [39] A. E. Jimenez-Cano, J. Martin, G. Heredia, A. Ollero and R. Cano, "Control of an aerial robot with multi-link arm for assembly tasks," *IEEE International Conference on Robotics and Automation*, pp. 4916-4921, 2013.
- [40] A. Suarez, F. Real, V. M. Vega, G. Heredia, A. Rodriguez-Castaño and A. Ollero, "Compliant Bimanual Aerial Manipulation: Standard and Long Reach Configurations," *IEEE Access*, vol. 8, pp. 88844-88865, 2020.
- [41] T. W. Danko, K. P. Chaney and P. Y. Oh, "A parallel manipulator for mobile manipulating UAVs," *IEEE International Conference on Technologies for Practical Robot Applications (TePRA)*, pp. 1-6, 2015.
- [42] P. Chermprayong, K. Zhang, F. Xiao and M. Kovac, "An Integrated Delta Manipulator for Aerial Repair: A New Aerial Robotic System," *IEEE Robotics & Automation Magazine*, 26(1), pp. 54-66, 2019.
- [43] A. Ollero et al., "The AEROARMS Project: Aerial Robots with Advanced Manipulation Capabilities for Inspection and Maintenance," *IEEE Robotics & Automation Magazine*, 25(4), pp. 12-23, 2018.
- [44] H. Nguyen, S. Park and D. Lee, "Aerial tool operation system using quadrotors as Rotating Thrust Generators," *IEEE/RSJ International Conference on Intelligent Robots and Systems (IROS)*, pp. 1285-1291, 2015.
- [45] G. Muscio et al., "Coordinated Control of Aerial Robotic Manipulators: Theory and Experiments," *IEEE Transactions on Control Systems Technology*, 26(4), pp. 1406-1413, 2018.

- [46] M. Tognon, C. Gabellieri, L. Pallottino and A. Franchi, "Aerial Co-Manipulation With Cables: The Role of Internal Force for Equilibria, Stability, and Passivity," *IEEE Robotics and Automation Letters*, 3(3), pp. 2577-2583, 2018.
- [47] H. Lee, H. Kim, W. Kim and H. J. Kim, "An Integrated Framework for Co-operative Aerial Manipulators in Unknown Environments," *IEEE Robotics and Automation Letters*, 3(3), pp. 2307-2314, 2018.
- [48] H. Nguyen, S. Park, J. Park and D. Lee, "A Novel Robotic Platform for Aerial Manipulation Using Quadrotors as Rotating Thrust Generators," *IEEE Transactions on Robotics*, 34(2), pp. 353-369, 2018.
- [49] V. Narli and P. Y. Oh, "Hardware-in-the-loop Test Rig to Capture Aerial Robot and Sensor Suite Performance Metrics," *IEEE/RSJ International Conference on Intelligent Robots and Systems*, pp. 3521-3526, 2006.
- [50] C. Korpela, M. Orsag, Y. Jun, P. Brahmhatt and P. Oh, "A hardware-in-the-loop test rig for aerial manipulation," *International Conference on Unmanned Aircraft Systems (ICUAS)*, pp. 982-987, 2013.
- [51] T. W. Danko and P. Y. Oh, "Evaluation of visual servoing control of aerial manipulators using test gantry emulation," *International Conference on Unmanned Aircraft Systems (ICUAS)*, pp. 821-829, 2014.
- [52] C. Korpela, M. Orsag and P. Oh, "Towards valve turning using a dual-arm aerial manipulator," *IEEE/RSJ International Conference on Intelligent Robots and Systems (IROS)*, pp. 3411-3416, 2014.
- [53] C. Korpela, M. Orsag, and P. Oh, "Hardware-in-the-Loop Verification for Mobile Manipulating Unmanned Aerial Vehicles," *Journal of Intelligent and Robotic Systems*, pp.725-736, 2014
- [54] C. Korpela, M. Orsag, T. Danko and P. Oh, "Insertion tasks using an aerial manipulator," *IEEE International Conference on Technologies for Practical Robot Applications (TePRA)*, pp. 1-6,2014.
- [55] C. L. Teo, E. Burdet and H. P. Lim, "A robotic teacher of Chinese handwriting," *Proceedings 10th Symposium on Haptic Interfaces for Virtual Environment and Teleoperator Systems (HAPTICS)*, pp. 335-341, 2002.
- [56] C. Basdogan, S. De, J. Kim, Manivannan Muniyandi, H. Kim and M. A. Srinivasan, "Haptics in minimally invasive surgical simulation and training," *IEEE Computer Graphics and Applications*, 24(2), pp. 56-64, 2004.
- [57] T. Bhattacharjee, G. Lee, H. Song and S. S. Srinivasa, "Towards Robotic Feeding: Role of Haptics in Fork-Based Food Manipulation," *IEEE Robotics and Automation Letters*, 4(2), pp. 1485-1492, 2019.

- [58] V. Yem and H. Kajimoto, "Wearable tactile device using mechanical and electrical stimulation for fingertip interaction with virtual world," *IEEE Virtual Reality (VR)*, pp. 99-104, 2017.
- [59] M. Mohammadi, A. Franchi, D. Barcelli and D. Prattichizzo, "Cooperative aerial tele-manipulation with haptic feedback," *IEEE/RSJ International Conference on Intelligent Robots and Systems (IROS)*, pp. 5092-5098, 2016.
- [60] S. Park et al., "ODAR: Aerial Manipulation Platform Enabling Omnidirectional Wrench Generation," *IEEE/ASME Transactions on Mechatronics*, 23(4), pp. 1907-1918, 2018.
- [61] Tiehua Chen, Dingxuan Zhao and Zhuxin Zhang, "Research on the tele-operation robot system with tele-presence based on the virtual reality," *IEEE International Conference on Robotics and Biomimetics (ROBIO)*, Sanya, 2007, pp. 302-306, doi: 10.1109/ROBIO.2007.4522178.
- [62] J. P. Whitney, Tianyao Chen, J. Mars and J. K. Hodgins, "A hybrid hydrostatic transmission and human-safe haptic telepresence robot," *IEEE International Conference on Robotics and Automation (ICRA)*, pp. 690-695, 2016.
- [63] A. Valiton and Z. Li, "Perception-Action Coupling in Usage of Telepresence Cameras," *IEEE International Conference on Robotics and Automation (ICRA)*, pp. 3846-3852, 2020.
- [64] D. Wallace, J.C. Vaz, Y.H. He, L. Georgescu, P.Y. Oh, "Multimodel Teleoperation of Heterogeneous Robots within a Construction Environment," *IEEE/RSJ International Conference on Intelligent Robots and Systems (IROS)*, 2020.
- [65] J. Lee et al., "Visual-Inertial Telepresence for Aerial Manipulation," *IEEE International Conference on Robotics and Automation (ICRA)*, pp. 1222-1229, 2020.
- [66] S. Bouabdallah, P. Murrieri and R. Siegwart, "Design and control of an indoor micro quadrotor," *IEEE International Conference on Robotics and Automation (ICRA)*, pp. 4393-4398, 2004.
- [67] R. Mahony, V. Kumar and P. Corke, "Multirotor Aerial Vehicles: Modeling, Estimation, and Control of Quadrotor," *IEEE Robotics and Automation Magazine*, 19(3), pp. 20-32, 2012.
- [68] M. Orsag, C. Korpela, P.Y. Oh, S. Bogdan, *Aerial Manipulation*, Springer Publishing, 2018.
- [69] F. Ruggiero, V. Lippiello and A. Ollero, "Aerial Manipulation: A Literature Review," *IEEE Robotics and Automation Letters*, 3(3), pp. 1957-1964, 2018.

- [70] D. Kim and P. Y. Oh, "Skywriting unmanned aerial vehicle proof-of-concept design," *International Conference on Unmanned Aircraft Systems (ICUAS)*, pp. 1398-1403, 2017.
- [71] D. Kim and P. Y. Oh, "Lab automation drones for mobile manipulation in high throughput systems," *IEEE International Conference on Consumer Electronics (ICCE)*, pp. 1-5, 2018.
- [72] D. Kim and P. Y. Oh, "Toward Lab Automation Drones for Micro-plate Delivery in High Throughput Systems," *IEEE International Conference on Unmanned Aircraft Systems (ICUAS)*, pp. 279-284, 2018.
- [73] D. Kim and P. Y. Oh, "Towards Micro-Plate Delivery using a re-sized Lab Automation Drone in High Throughput Systems," *IEEE International Conference on Ubiquitous Robots (UR)*, pp. 682-686, 2018.
- [74] D. Kim and P. Y. Oh, "Testing-and-Evaluation Platform for Haptics-based Aerial Manipulation with Drones," *IEEE American Control Conference (ACC)*, pp. 1453-1458, 2020.
- [75] D. Kim and P. Y. Oh, "Human-Drone Interaction for Aerially Manipulated Drilling using Haptic Feedback," *IEEE/RSJ International Conference on Intelligent Robots and Systems (IROS)*, 2020.
- [76] D. A. G. Jauregui, F. Argelaguet, A. Olivier, M. Marchal, F. Multon and A. Lecuyer, "Toward "Pseudo-Haptic Avatars": Modifying the Visual Animation of Self-Avatar Can Simulate the Perception of Weight Lifting," *IEEE Transactions on Visualization and Computer Graphics*, 20(4), pp. 654-661, 2014.
- [77] M. E. Walker, D. Szafir and I. Rae, "The Influence of Size in Augmented Reality Telepresence Avatars," *IEEE Conference on Virtual Reality and 3D User Interfaces (VR)*, pp. 538-546, 2019.
- [78] T. M. Takala, C. C. Hsin and T. Kawai, "Stand-alone, Wearable System for Full Body VR Avatars: Towards Physics-based 3D Interaction," *IEEE Conference on Virtual Reality and 3D User Interfaces (VR)*, pp. 1398-1398, 2019.
- [79] I. Bae, "Avatar drone: Drone as telepresence platform with 3D mobility," *International Conference on Ubiquitous Robots and Ambient Intelligence (URAI)*, pp. 452-453, 2016.
- [80] X. Wang, J. Li, K. Shima, T. Kosaki and S. Li, "Drone were me: Flying drone as avatar by aligned stereo view and head pose," *IEEE 5th Global Conference on Consumer Electronics*, pp. 1-2, 2016.
- [81] D. Kim and P. Y. Oh, "Toward Avatar-Drone: A Human-Embodied Drone for Aerial Manipulation," *International Conference on Unmanned Aircraft Systems (ICUAS)*, pp. 567-574, 2021.

- [82] Avatar XPRIZE Competition Rules and Regulations [Online] Available: "https://www.xprize.org/prizes/avatar/guidelines"
- [83] ROS Sharp (ROS#) [Online]
Available: <https://github.com/siemens/ros-sharp>
- [84] S. Chiaverini, B. Siciliano and O. Egeland, "Review of the damped least-squares inverse kinematics with experiments on an industrial robot manipulator," *IEEE Transactions on Control Systems Technology*, 2(2), pp. 123-134, 1994.
- [85] Orocos Kinematics and Dynamics [Online]
Available : <https://www.orocos.org/kdl.html>
- [86] Leap Motion Controller [Online]
Available : <https://www.ultraleap.com/product/leap-motion-controller/>
- [87] Seul Jung, T. C. Hsia and R. G. Bonitz, "Force tracking impedance control of robot manipulators under unknown environment," *IEEE Transactions on Control Systems Technology*, 12(3), pp. 474-483, 2004.
- [88] D. Lee, H. Seo, I. Jang, S. J. Lee and H. J. Kim, "Aerial Manipulator Pushing a Movable Structure Using a DOB-Based Robust Controller," *IEEE Robotics and Automation Letters*, 6(2), pp. 723-730, 2021.
- [89] Shim, H., Park, G., Joo, Y. et al., "Yet another tutorial of disturbance observer: robust stabilization and recovery of nominal performance," *Control Theory Technology* 14, pp. 237-249, 2016.
- [90] 3DSystems Haptic [Online] Availabe : "https://www.3dsystems.com/haptics"
- [91] OpenHaptics Developer Software [Online]
Available: <https://www.3dsystems.com/haptics-devices/openhaptics>
- [92] R.Q. VanderLinde et al., "The Hapticmaster, a New HighPerformance Haptic Interface," *Proc. Eurohaptics, Edinburgh University*, pp. 1-5, 2002.
- [93] PX4 Controller Diagrams [Online]
Available: <https://dev.px4.io/v1.9.0/en/flight-stack/controller-diagrams>
- [94] Ardupilot - versatile, trusted, open [Online]
Available: <https://ardupilot.org/>
- [95] MultiWii Project [Online]
Available : <http://www.multiwii.com/>
- [96] Dynamixel MX-28 E-Manual [Online]
Available: <http://emanual.robotis.com/docs/en/dxl/mx/mx-28/>

- [97] National Institute of Health (NIH) - Small Business Innovation Research (SBIR)
Available: <https://www.sbir.gov/node/1166395>
- [98] ANA Avatar XPRIZE [Online]
Available: <https://www.xprize.org/prizes/avatar>
- [99] Microsoft Mixed Reality Toolkit(MRTK) [Online]
Available: <https://docs.microsoft.com/en-us/windows/mixed-reality/develop/unity/mrtk-getting-started>
- [100] C. Faure et al., "Adding Haptic Feedback to Virtual Environments With a Cable-Driven Robot Improves Upper Limb Spatio-Temporal Parameters During a Manual Handling Task," *IEEE Transactions on Neural Systems and Rehabilitation Engineering*, 28(10), pp. 2246-2254, 2020.

CURRICULUM VITAE

Graduate College
University of Nevada, Las Vegas

Dongbin Kim

akdba0207@gmail.com

Address:

1325 E Flamingo Road, College of Engineering Robotics Lab
Las Vegas, Nevada 89119

Degrees:

Bachelor of Science, Aircraft Systems Engineering, 2017
Korea Aerospace University, Republic of Korea

Dissertation Title: A HUMAN-EMBODIED DRONE FOR DEXTEROUS AERIAL
MANIPULATION

Dissertation Examination Committee:

Chairperson, Dr. Paul. Y. Oh, Ph.D.
Committee Member, Dr. Woosoon Yim, Ph.D.
Committee Member, Dr. Mohamed Trabia, Ph.D.
Committee Member, Dr. Georg Mauer, Ph.D.
Graduate Faculty Representative, Dr. Jin Ouk Choi, Ph.D.

Publication:

- D. Kim, P. Y. Oh, “Skywriting Unmanned Aerial Vehicle Proof-of-Concept Design”, IEEE International Conference on Unmanned Aircraft Systems (ICUAS), 2017.
- D. Kim, P. Y. Oh, “Lab Automation Drones for Mobile Manipulations in High Throughput Systems” , IEEE International Conference on Consumer Electronics (ICCE), 2018
- D. Kim, P. Y. Oh, “Lab Automation Drones for Mobile Manipulations in High Throughput Systems”, Society of Lab Automation and Screening (SLAS), 2018
- D. Kim, P. Y. Oh, “Towards Micro-Plate Delivery using a re-sized Lab Automation Drone in High Throughput Systems”, IEEE International Conference on Ubiquitous Robots (URAI), 2018

- D. Kim, P. Y. Oh, “Toward Lab Automation Drones for Micro-plate Delivery in High Throughput Systems”, IEEE International Conference on Unmanned Aircraft Systems (ICUAS), 2018
- D. Kim, P. Y. Oh, “Parallel Manipulator-Gripper for Mobile Manipulating UAVs”, Annual Meeting of Inspecting and Preserving Infrastructure Through Robotic Exploration (INSPIRE), 2018
- D. Kim, J. O. Choi, “A New UAV-based Module Lifting and Transporting Method: Advantages and Challenges”, International Symposium on Automation and Robotics in Construction (ISARC), 2019
- D. Kim, P. Y. Oh, “Testing-and-Evaluation Platform for Haptic-based Aerial Manipulation with drones”, IEEE American Control Conference (ACC), 2020
- D. Kim, P. Y. Oh, “Human Collaborative Haptic-Based Mobile-Manipulating UAVs”, Annual Meeting of Inspecting and Preserving Infrastructure Through Robotic Exploration (INSPIRE), 2020
- D. Kim, P. Y. Oh, “Human-Drone Interaction for Aerially Manipulated Drilling using Haptic Feedback”, IEEE International Conference on Intelligent Robots and Systems (IROS), 2020
- D. Kim, P. Y. Oh, “Avatar-Drone: A Human-Embodied Drone for Aerial Manipulation”, IEEE International Conference on Unmanned Aircraft Systems (ICUAS), 2021
- D. Kim, P.Y. Oh, ”Aerial Manipulation using Embodied Human-Intelligence”, IEEE International Conference on Robotics and Automation (ICRA), 2022 (Submitted)
- D. Kim, P.Y. Oh, “A Human-Embodied Drone for Dexterous Manipulation in Bridge Inspection and Maintenance”, International Workshop on Structural Health Monitoring (IWSHM), 2022 (Submitted)

Invited Talk:

- Lab Automation Drones for Mobile Manipulation in High Throughput Systems - Society of Lab Automation and Screening (SLAS) International Conference and Exhibition, Tony B. Awardee talk, 2018
- A new UAV-based Module Lifting and Transporting Method, Construction Industry Institute (CII) Modularization Communities for Business Advancement (CBA) virtual meeting, 2020
- Aerial Manipulation using Embodied Human-Intelligence for Construction, CEE 710: Modular Construction, University of Nevada, Las Vegas, 2021